US Department of Energy, National Energy Technology Laboratory
Contract No. DEFE0031662

Tuning Surface Stoichiometry of SOFC Electrodes at the Molecular and Nano-scale for Enhanced Performance and Durability

Final Report

Submission Date: January 5, 2020

Project Period: 10/01/2018-09/30/2020

PI: Eric D. Wachsman, Ph.D.
Director, Maryland Energy Innovation Institute
William L. Crentz Centennial Chair in Energy Research
University of Maryland
College Park, MD 20742
ewach@umd.edu
Tel.: (301) 405-8193, Fax.: (301) 314-8514

Submitting Official: Stephanie M. Swann
Senior Contract Administrator
University of Maryland
Office of Research Administration
3112 Lee Building
College Park, MD 20742
smbrack@umd.edu
Tel.: (301) 405-8079, Fax.: (301) 314-9569
DUNS Number: 790934285

EXECUTIVE SUMMARY

This project achieved the following objectives. Different cation segregation behaviors of different common SOFC cathodes, including $La_{0.6}Sr_{0.4}Co_{0.2}Fe_{0.8}O_{3-\delta}$ (LSCF), $Sr_{0.5}Sm_{0.5}O_{3-\delta}$ (SSC), and $PrBa_{0.5}Sr_{0.5}Co_{1.5}Fe_{0.5}O_{5+\delta}$ (PBSCF), were determined. We showed how oxygen partial pressure and gas impurities impact the stability of SOFC cathodes. We developed atomic layer deposition (ALD) coating techniques for electrodes and showed that by introducing different elements and different ALD oxidizers, electrode surface chemistry can be altered, resulting in enhanced oxygen reduction kinetics. In addition, we developed solution infiltration technique to enhance performance and durability of electrodes. Different infiltrates as well as different thermal treatment processes were screened to identify the optimal surface modification process that yields both low impedance and high durability. The modified cathode shows excellent stability and has a low area specific resistance (ASR) of only 0.2 Ωcm^2 at 600 °C after over 2000 hours of operation. Further, we developed ceramic anodes, $SrFe(Co,Mo)O_3$ (SFCM) and $SrFe(Ni,Mo)O_3$(SFNM), and enhanced anode oxidation kinetics by solution infiltration or *in situ* catalyst exsolution from the ceramic anode surface. The modified anodes showed improved performance in full SOFCs, and the optimized anode modification shows high stability for over 400 hours at 550 °C. Moreover, the modified anode also demonstrates high durability in methane. This work provides fundamental understanding of electrode surface chemistry and demonstrates a simple, facile, cost-effective approach to enhance catalytic activity and durability of SOFC electrodes.

ACCOMPLISHMENTS

Major Goals/Objectives and Milestones

This Statement of Project Objectives outlines the tasks planned to achieve the following objectives:

- Control the surface stoichiometry of electrodes (cathode and anode) to enhance the durability and performance of solid oxide fuel cells (SOFCs)
- Correlate the catalytic activity with the surface defect chemistry of modified electrodes.
- Develop surface modification techniques to modify the surface stoichiometry of electrodes
- Prevent the phase segregation such as strontium carbonate / strontium oxide formation in common cathodes $La(Sr)MnO_3$ (LSM), $La(Sr)Co(Fe)O_3$ (LSCF), and $Sm(Sr)CoO_3$ (SSC), and advanced ceramic anodes $(SrFe(Ni,Mo)O_3$, $(SrFe(Co,Mo)O_3$ through the control of surface cation/anion stoichiometry
- Develop novel approaches utilizing different cost-effective and mass producible surface modification techniques including atomic layer deposition (ALD) and solution infiltration techniques
- Identify the optimal surface modification process that yields the best initial performance and long-term stability on the modified electrodes

- Quantify degradation rates/performance and reveal the underlying mechanisms on tuned stoichiometric electrodes
- Integrate the optimized cathode and anode to the full cell level
- Adapt the surface modification process to full format SOFCs

Milestone logs

MS.2.1: Complete development of ALD coating techniques. **Due** Y1Q1.

MS.2.2: Complete development of solution-based infiltration. **Due** Y1Q2.

MS.3.1: Complete performance characterization of modified cathodes. **Due** Y1Q3.

MS.3.2: Identify optimized surface modification process. **Due** Y1Q4.

MS.4.1: Determine the performance of modified anodes. **Due** Y2Q1.

MS.4.2: Complete performance characterization of modified anodes in methane. **Due** Y2Q2.

MS.5.1: Complete performance characterization of button cells integrated with modified anodes and cathodes. **Due** Y2Q3.

MS.5.2: Complete post-testing characterization on surface modified SOFCs. **Due** Y2Q4.

Cathode Surface Segregation Evaluation

Sample preparation - Fabrication and Aging of Cathode Materials

Commercially available cathode powders LSCF and SSC were purchased from Praxair. PBSCF was synthesized through sol-gel synthesis from the metal nitrate precursors $Pr(NO_3)_3 \cdot 6H_2O$ (Sigma Aldrich), $Ba(NO_3)_2$ (Alfa Aesar), $Sr(NO_3)_2$ (Alfa Aesar), $Co(NO_3)_2\ 6H_2O$ (Carolina), and $Fe(NO_3)_3\ 9H_2O$ (Sigma Aldrich). These precursors were dissolved in water along with ethylene glycol and citric acid, in a 1:1.5:2 molar ratio. After dissolution, the pH was raised to 7-8 using ammonium hydroxide and the precipitate dried. The result was then ground up and heated until auto-ignition. Finally, it was calcined at 1075°C for 5 hours and phase was verified with XRD.

Dense samples were made by pressing each cathode powder with a hydraulic press. Resulting discs were sintered in air at 1400°C for 4 hours for LSCF, 1175°C for 5 hours for SSC, and 1175°C for 11 hours for PBSCF. Once sintered, the discs were polished with SiC sandpaper down to 8μ and then with diamond polishing particles to 0.25μ. This allows observation of grain boundaries with SEM.

Dense samples of LSCF, PBSCF, and SSC were aged in environmentally controlled reactors. Gas flow rates were controlled with mass flow controllers and the gas environment was verified with a Zirox SGM5EL PO_2 sensor. O_2, N_2, CO_2, and H_2 (Airgas) were used as gases to create each testing environment. The aged samples were then studied under SEM to evaluate the

changes to their surface microstructure. Analysis of surface particles was then carried out using ImageJ software and the Trainable WEKA Segmentation plugin.

Surface SrO Segregation

The compositions of the chosen cathode materials were such that SrO segregation could be observed without any hindrance. Stoichiometric and undoped compositions were chosen so that we control the SrO segregation by altering gas environment, temperature, and subsequent surface modification. **Figure 1** shows the XRD spectra of each cathode material indicating pure phase. All three materials are perovskites but with different ordering and lattice parameters. LSCF and SSC are both orthorhombic perovskites while PBSCF is a double perovskite.

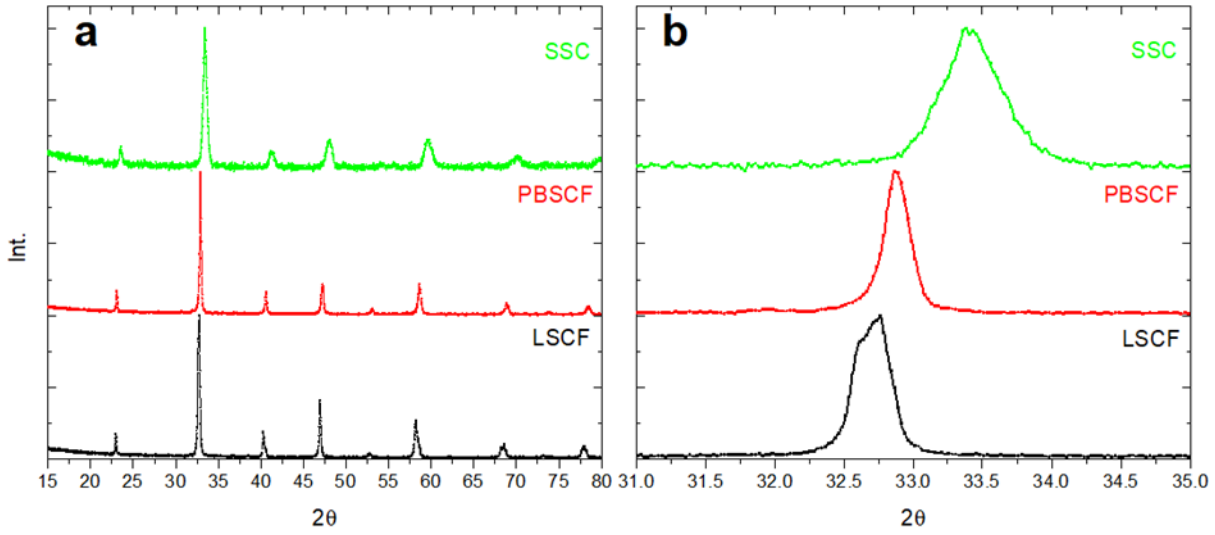

Figure 1. XRD of unmodified cathode materials. (a) XRD spectra indicating perovskite phase (b) Insert showing primary perovskite peak around 2θ=32-34°.

We studied different variables that controlled the degrees of surface cation segregation on perovskites, including time, temperature, oxygen partial pressure (pO_2), and gas impurities.

The aging effect on the LSCF surface segregation is summarized in **Figure 2**. No significant secondary phases can be seen on the unaged sample surface. As the aging time increases at 800 °C in ambient air, the surface covered by particles increases (**Figure 2 (b)-(d)**). Grain boundaries are easy to distinguish even when no SrO segregation was observed. After aging for 25 hours, It can also be seen that some grains have more prominent secondary phase growth than others. The segregated SrO preferably presents at the grain boundaries (**Figure 2 (b)**. These SrO particles migrate to particular grains after a longer aging time (**Figure 2 (c) and (d)).** Therefore, it is likely a result of each lattice orientation having different defect formation energies.

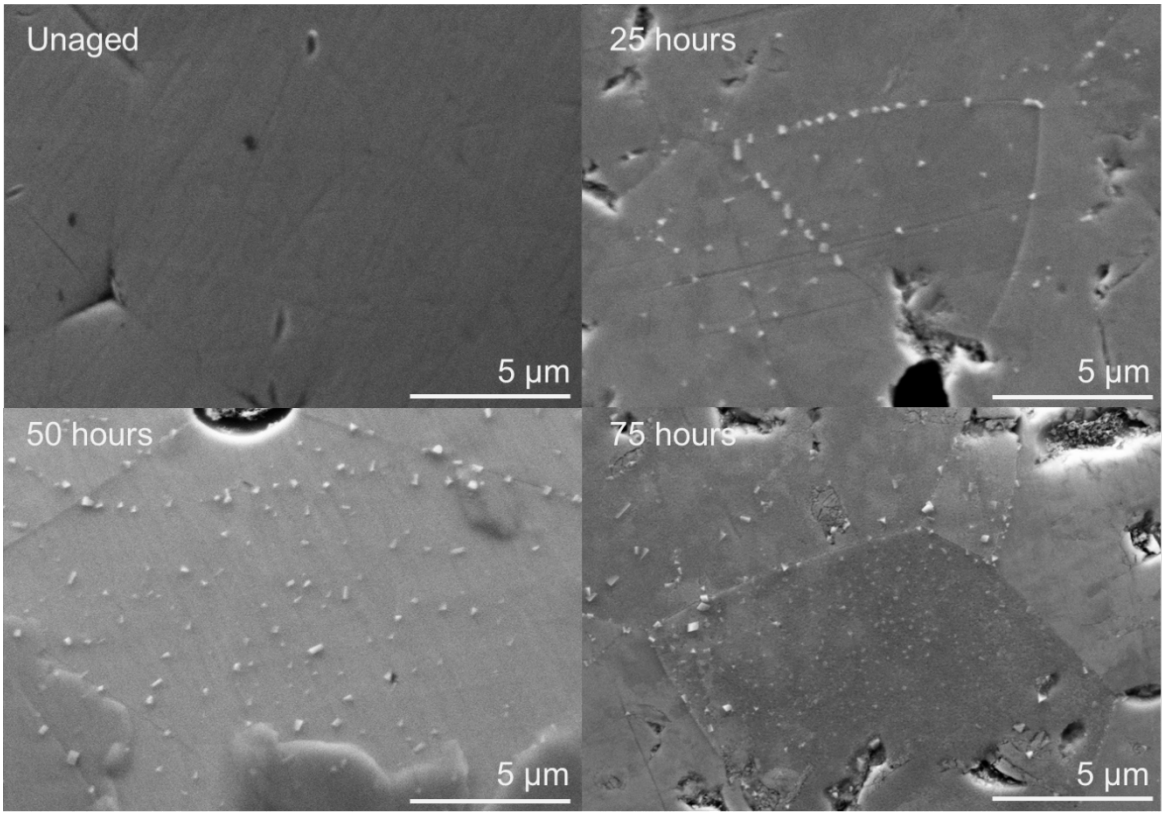

Figure 2. Time dependence of the LSCF surface segregation at 800 °C.

In addition to aging time, the effect of temperature on surface segregation was also studied. All samples were aged in synthetic air for 25 hours and different aging temperatures were tested. **Figure 3** shows the temperature dependence on the nucleation of secondary phases on the surface. SrO segregation is observed as low as 600°C. As the aging temperature increases, SrO particles tend to agglomerate to larger particles. This can be seen in the increasing particle size and surface coverage with temperature. Based on our results, the diffusion of Sr cations is thermally activated, and the phase segregation of LSCF is thermodynamically favored at higher temperature. These segregated phase tend to migrate to the surface through grain boundaries and then well-distribute on the grain.[1,2]

At 850°C and above some grains are completely covered by the secondary phase SrO. However, the degree of phase segregation is different in different grains, suggesting the crystalline orientation plays a vital role in the segregation process. In addition, pores that grow with increasing temperature are visible. It is likely that these pores are formed as a result of cation diffusion. The high temperature enhances the rate of diffusion towards the surface, thus making the pores bigger.

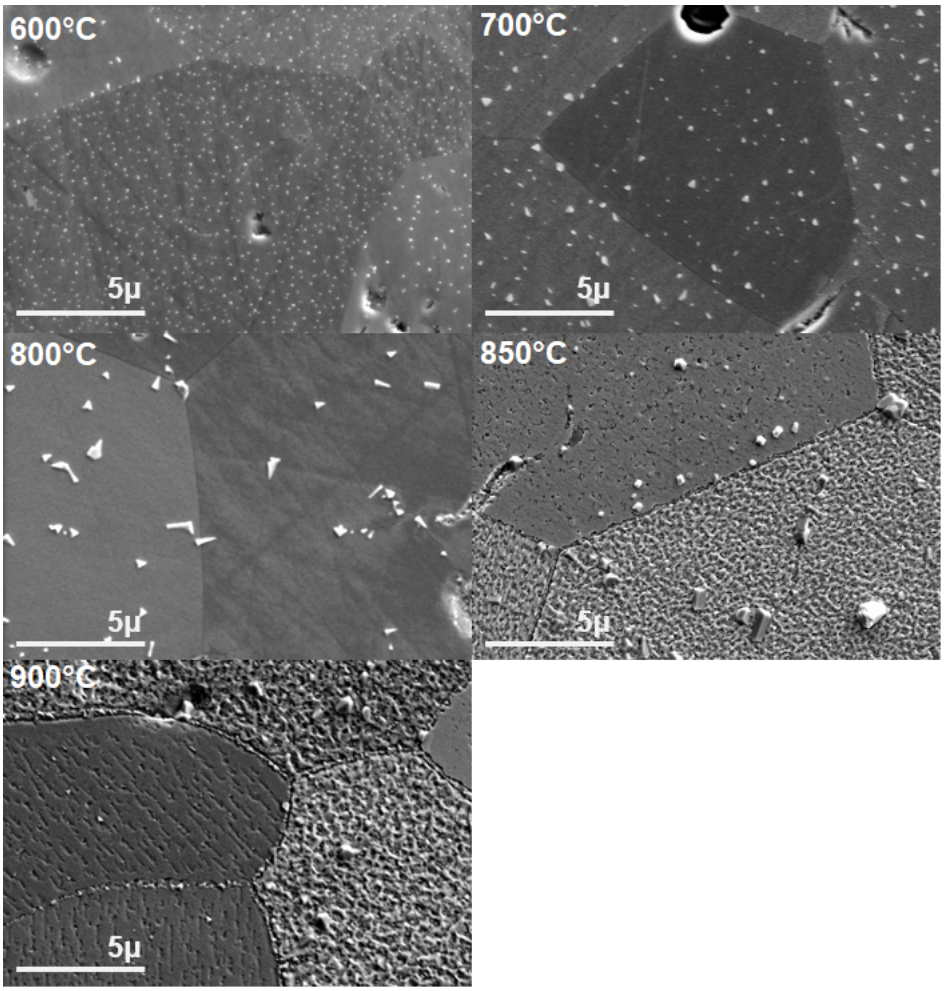

Figure 3. Temperature Dependence of SrO segregation on LSCF aged in synthetic air for 25 hours in the temperature range 600-900°C

To study the pO_2 effects on the surface cation segregation, LSCF was exposed to a wide range of pO_2 at 700°C for 25 hours. **Figure 4 s**hows the effect of each pO_2 on the surface morphology. Reducing conditions (5% H_2, balanced in N_2) shows some segregated particles. A further investigation is needed to identify the components as well as the phase of these particles. However, no secondary phases are observed in pure N_2. In synthetic air, SrO particles are clearly formed on the surface. At high pO_2 (1 atm O_2), it was found that the SrO concentration decreases when compared to synthetic air. Also, a pure O_2 environment causes smaller particles.

To understand the role of impurities in air, such as CO_2 and moisture, a comparison between these two conditions (synthetic air and pure O_2) as well as ambient air is shown in **Figure 5**. It was observed that there is a higher concentration of SrO segregate in ambient air, suggesting that the gaseous impurities in air promoted the nucleation of SrO on the surface. In contrast, the use of pure O_2 suppresses the formation of SrO, compared to the synthetic air one, which is consistent with the observation by Niania et al.[2] at a much lower gas pressure (3 mbar).

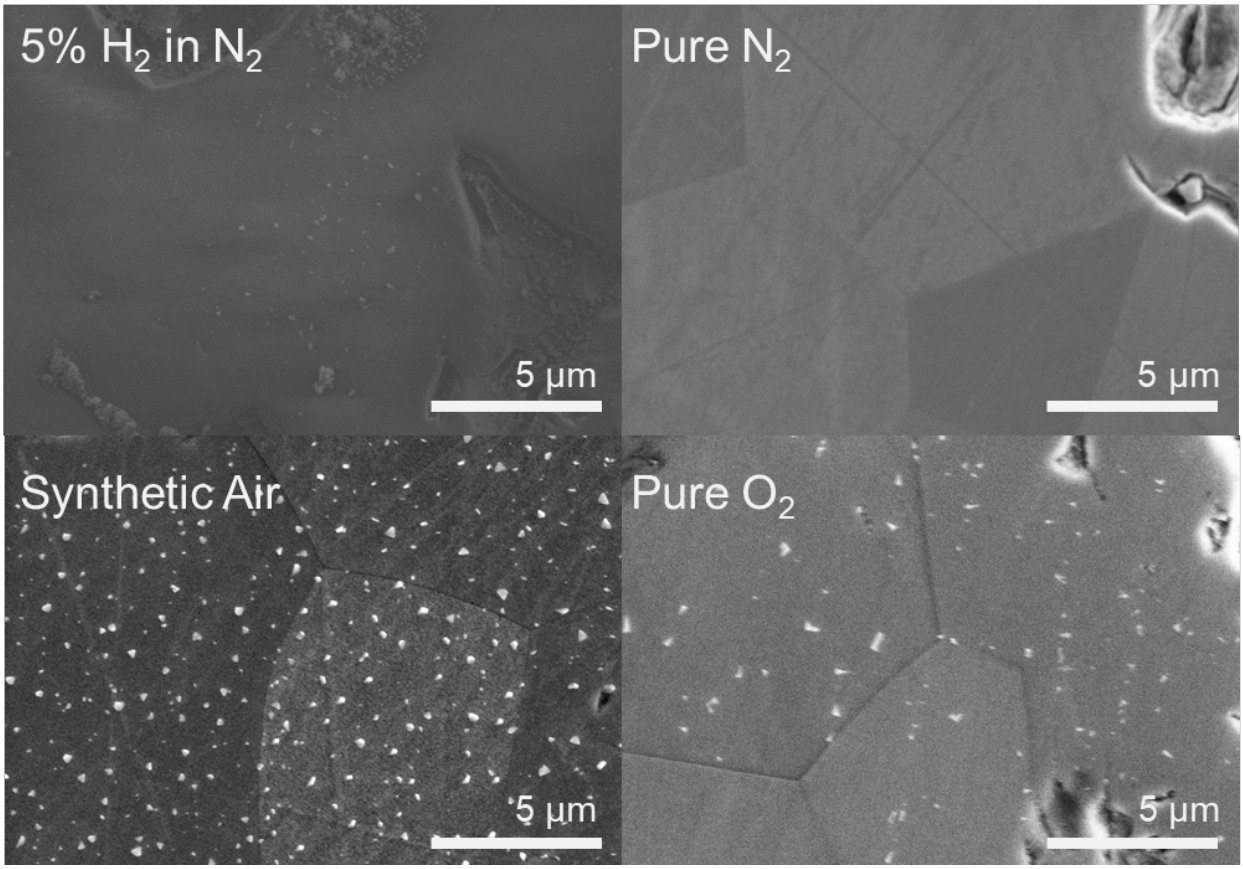

Figure 4. pO_2 dependence of SrO segregation on LSCF aged for 25 hours at 700°C in a wide range of pO_2.

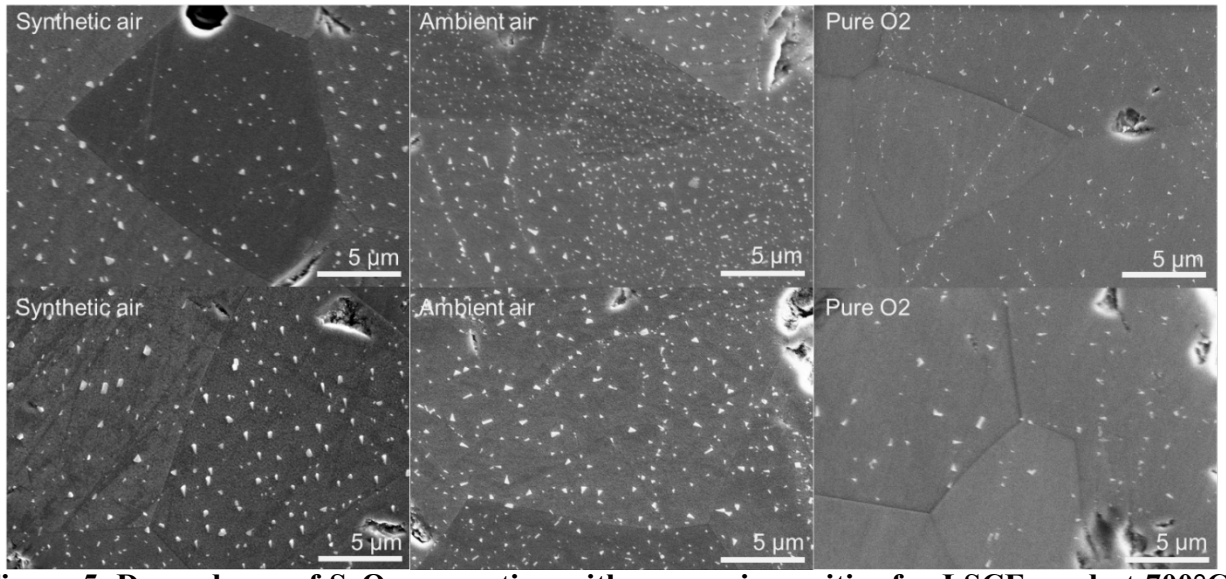

Figure 5. Dependence of SrO segregation with oxygen impurities for LSCF aged at 700°C for 25 hours in each gas environment.

Analysis of Aging Parameters on Microstructure

Following the aging of the LSCF, the distribution of the quantity and size of segregated particles was studied to determine the effect of each parameter on surface microstructure. These distributions are based on the image processing results of SEM images included in the previous report. The result of this analysis for aging time and temperature is shown in **Figure 6.**

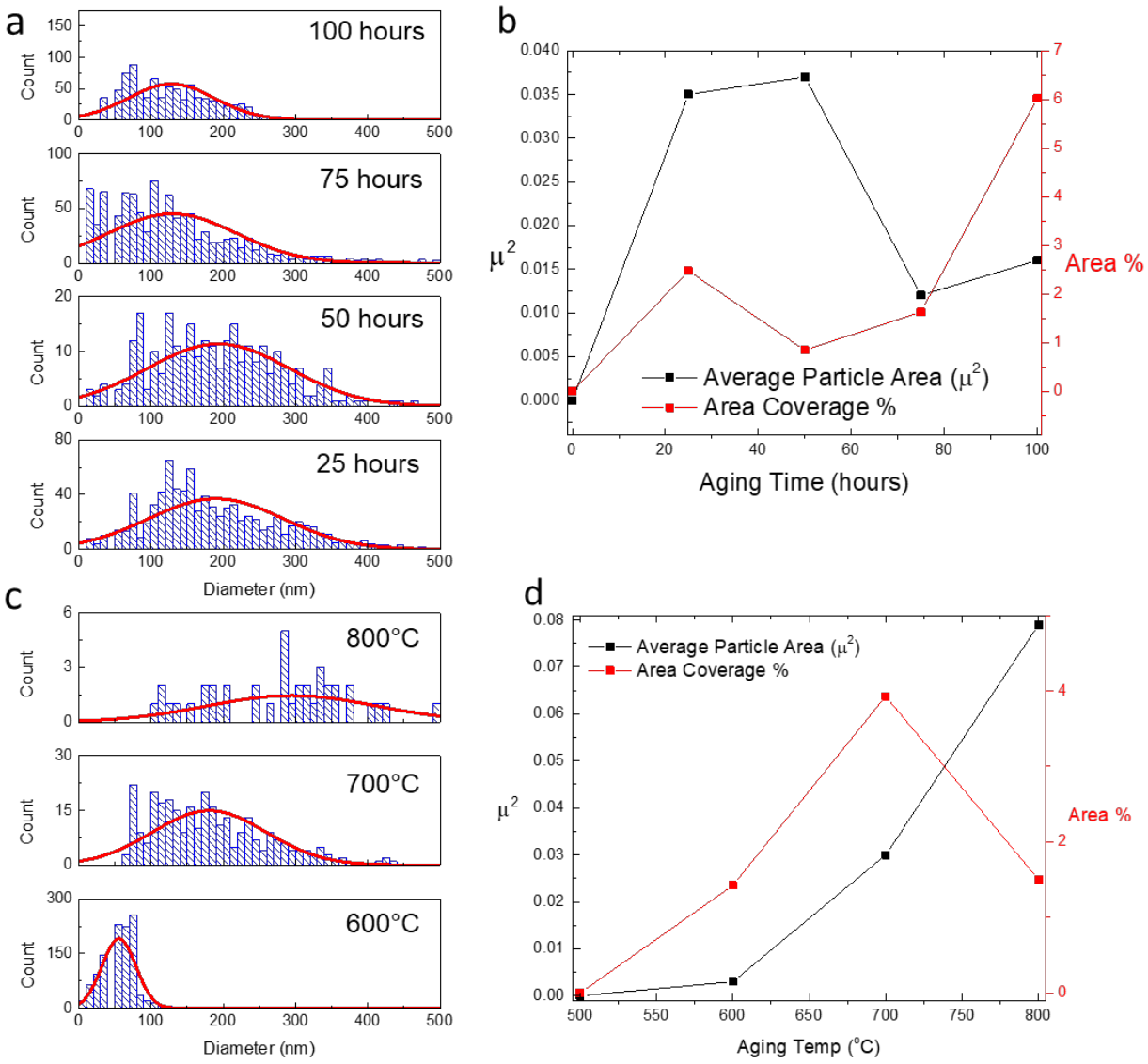

Figure 6. Effects of aging time and temperature on SrO segregation on LSCF. (a) Particle size distribution at each aging time, and (b) area coverage and average particle size as a function of aging time. LSCF bar samples were aged at 700 °C in synthetic air. (c) Particle size distribution at each aging temperature, and (d) area coverage and average particle size as a function of temperature. LSCF bar samples were aged for 25 hours in synthetic air.

As seen in **Figure 6(a-b)**, for LSCF aged at 700 °C, the relationship between aging time and particle size is not straightforward. As aging time increases, there is an initial increase in particle area followed by a decrease with additional aging time. Similarly, the SrO covered area coverage doesn't increase at a constant rate with the aging time. A similar trend in aging time in air was reported by Niania et al.[2] in which there was a local minimum in surface area coverage, albeit under different temperatures and pressures. What does increase steadily is the quantity of particles on the surface. This suggests that long term aging eventually promotes the formation of smaller particles rather than large ones. This could indicate that in these conditions smaller particles are more energetically favorable.

The effect of temperature on particle size distribution is more straightforward. **Figure 6 (c-d)** show increasing particle size with decreasing particle quantity. The reduction in the covered area is likely due to vertical growth of the particles, which can be seen to grow upwards at higher temperatures. It can thus be said that higher temperatures promote agglomeration of larger SrO particles which absorb the smaller ones. This means the trend of particle size and aging time could be more obvious at different temperature regimes. Above 800 °C, there was a great deal of surface roughness and decomposition, so a particle size analysis was not performed.

The gas environment effect on the LSCF surface was also examined to determine the LSCF degradation mechanism. Having varied the aging environment as a function of pO_2 and pCO_2, it was then possible to analyze the trends of particle size and surface coverage as a result of the gas compositions. **Figure 7 (a)** and **(b)** shows the effects of pO_2 on the SrO particle size distribution and SrO surface area coverage, respectively. All samples were aged at 700 °C for 25 hours in the stated atmosphere. Note that surface particles were not observed in pure N_2Using image processing, we are able to do statistical analysis on the precipitated particles, as shown in the size versus the population distribution in **Figure 7 (a)**. The results are summarized in **Figure 7 (b)**. The particle size and area coverage both follow the same trend: increase up to 21% O_2 and decrease with further O_2. The results suggest that the presence of oxygen is necessary for the SrO precipitation process because there is no observable SrO segregation in N_2. Further, the increase of pO_2 could promote a certain step of surface segregation process, likely the nucleation process. However, the high pO_2 could also change the defect concentration in LSCF, leading to a decrease in oxygen vacancy concentration. Since oxygen vacancies are known to contribute to Sr segregation, this would explain the reduction in surface coverage at high pO_2 range.

CO_2 appears to reduce the size of surface particles but may increase their quantity. **Figure 7 (c)** and **(d)** show the effects of pCO_2 on the SrO particle size distribution and SrO surface area coverage. All samples were aged at 700 °C for 25 hours in the stated atmosphere. The particle size shows a positive correlation with the pCO_2, as shown in **Figure 7 (c)**. The particle size as a function of pCO_2 is summarized in **Figure 7 (d)**, showing a linear dependence. Our results demonstrated that the precipitated particle size is controlled by the gas environment.

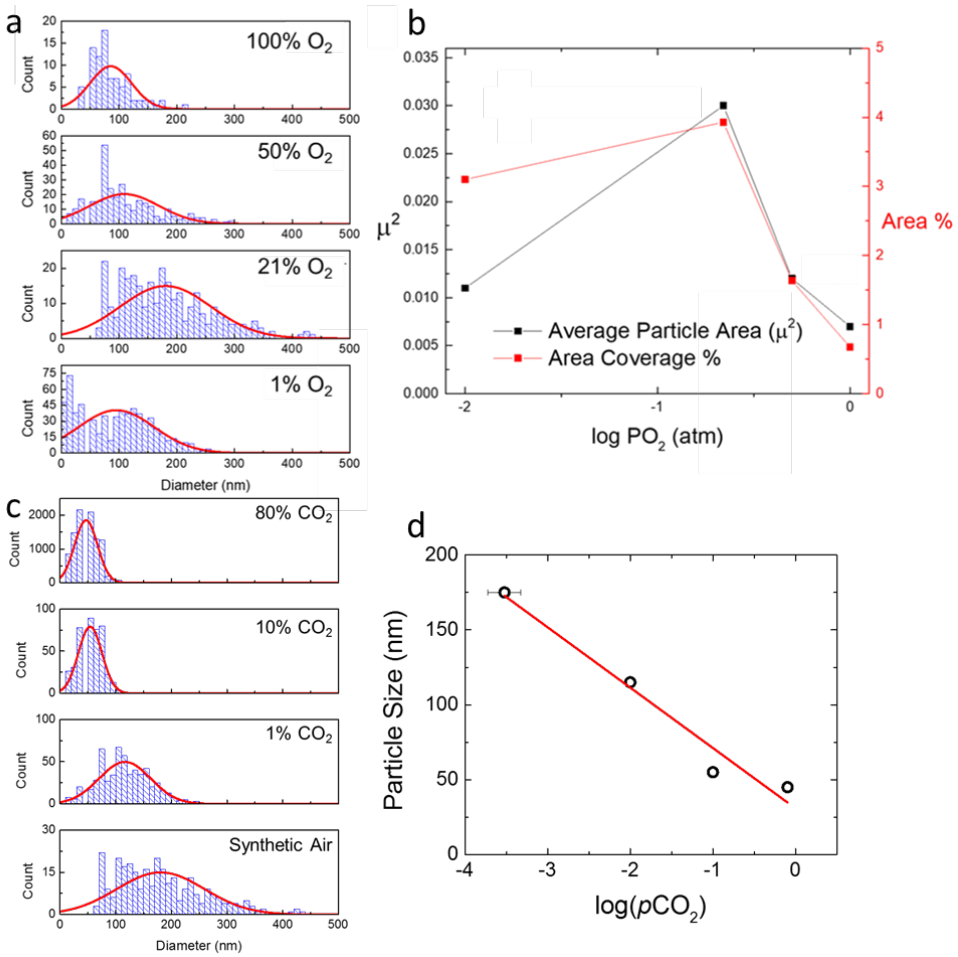

Figure 7. Effects of pO_2 and pCO_2 on SrO particle size distribution on LSCF. (a) Particle size distribution at each pO_2. (b) Trend of area coverage and average particle size with pO_2. (c) Particle size distribution at each CO_2 containing environment. (b) Trend of average particle size with level of CO_2.

We further confirmed that CO_2, O_2, and N_2 have different effects on the LSCF surface segregation. We designed another set of experiments: aging LSCF in a fixed gas ratio (80 %: 20%) of CO_2/O_2, CO_2/N_2, and N_2/O_2, as shown in **Figure 8**. All samples were aged at 700 °C for 25 hours. Interestingly, the sample aged in N_2/O_2 shows more severe surface segregation than the one in CO_2/N_2. Compared to other mixed gases, the CO_2/O_2 mixture results in smaller segregated particle size. This suggests that the ratio between O_2 and CO_2 is a factor in the surface segregation kinetics. In addition, each gas composition could cause different effects on the surface precipitation of LSCF. This study is the first to demonstrate the complex gas effects on LSCF surface segregation and resultant defect chemistry.

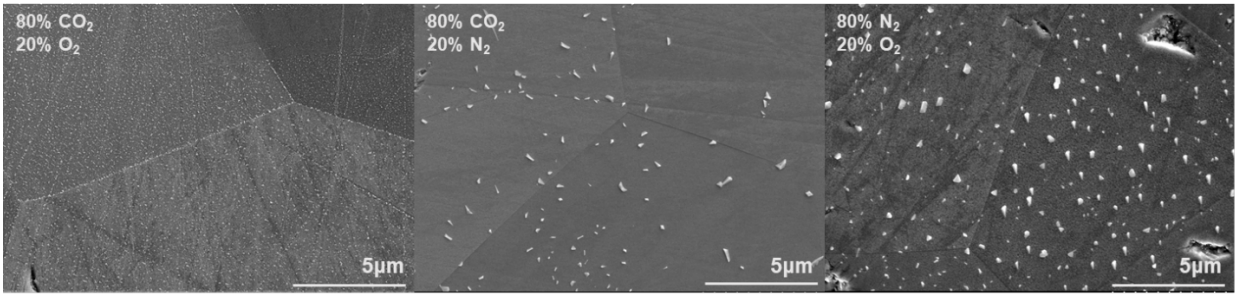

Figure 8. Surface Segregation on LSCF aged in 80% CO_2 with O_2 and N_2 separately compared to LSCF aged in 80% N_2 and 20 % O_2. All samples were aged at 700 °C for 25 hours.

Surface Chemistry Study using XPS

The surface compositions of aged LSCF samples were studied using XPS to determine the degree of Sr segregation on LSCF. This was done to determine the effect of its aging environment such as different oxygen partial pressures (pO_2) on surface chemistry of LSCF and correlation with the observed particle formation reported previously. **Figure 9** (**a**) shows the XPS of Sr 3d spectra for LSCF aged in different environments. Based on the binding energy of Sr 3d peaks, the surface SrO (blue) and Sr in LSCF lattice (green) can then be separated and quantified. The ratio between the bulk and surface (**Figure 9** (**b**)) is shown to change with pO_2 such that the highest level of Sr on the surface is found at the pO_2 which matches that of air. This was also found to be the gas environment in which the greatest level of surface coverage was observed. Thus, our results confirm that SrO segregation on cathodes is a function of gas environment, and both pO_2 and the air impurity concentration (such as pCO_2) significantly affects the Sr segregation level. We believe that SrO segregation on the oxide surface is determined by not only thermodynamic factors but also surface reaction kinetics that are determined by the operating environment.

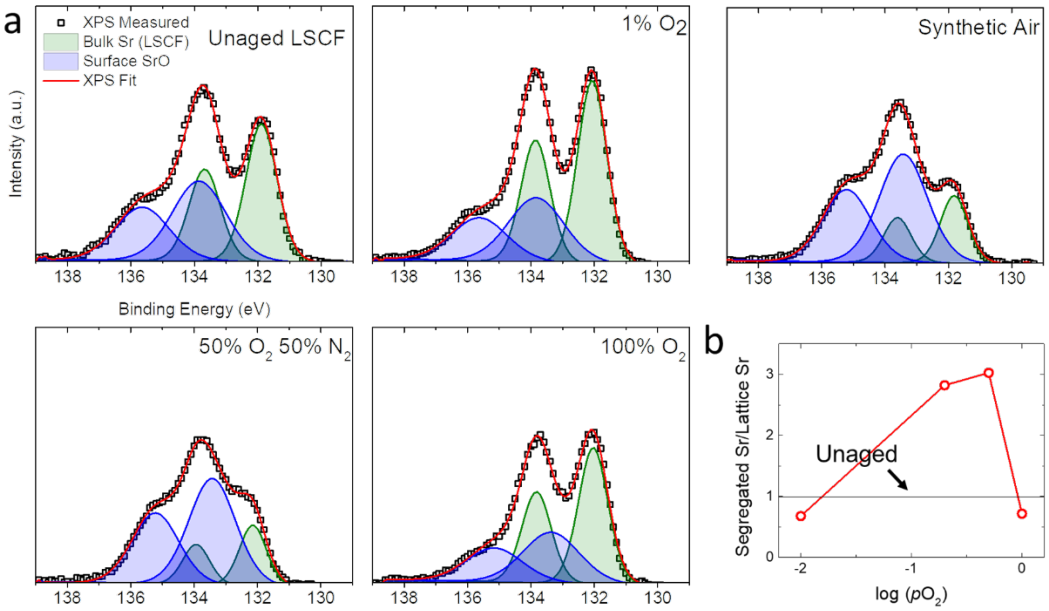

Figure 9. XPS spectra of dense LSCF samples aged at different pO_2 levels. (a) XPS Sr 3d Spectra at different pO_2's. Peaks associated with SrO and Sr in LSCF lattice are highlighted in blue and green, respectively. The pO_2 value is provided in the figures. (b) Ratio of surface to bulk Sr peak areas.

SrO Segregation on PBSCF and SSC

Study of the microstructure as function of aging conditions was also performed for PBSCF (a layered structure), and SSC (a low-temperature cathode). Both PBSCF and SSC have been demonstrated to have high performance with high long-term stability. The study of these materials can further advance the fundamental understanding of the SrO segregation.

Figure 10 shows the PBSCF surface as a function of aging time, with an unaged sample shown for comparison. Samples were aged at 700°C in synthetic air. Like LSCF, the grain boundaries are difficult to distinguish before aging. After only 25 hours, small particles are seen to cover most of the surface. As aging time continues, the particles are seen to agglomerate and increase in size. At 75 and 100 hours, the larger particles resemble those seen on LSCF.

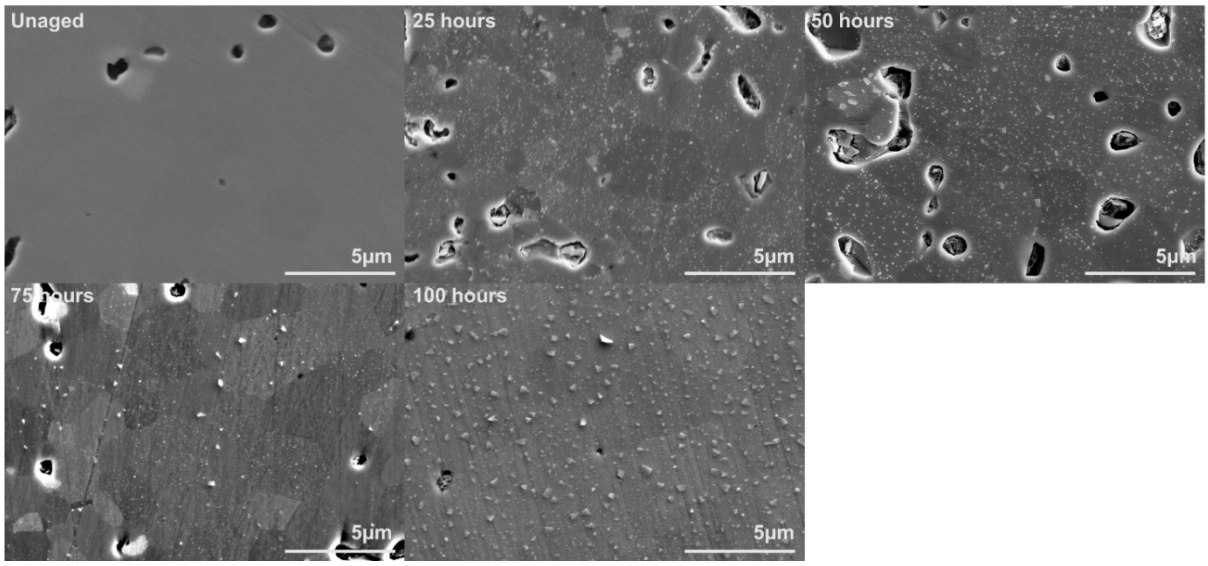

Figure 10. Effect of aging time on the PBSCF surface. Samples were aged at 700°C in synthetic air.

The effect of aging temperature on the PBSCF surface is shown in **Figure 11.** It is important to note that at 500 °C, no particles were observed with LSCF but particles are seen with PBSCF. This indicates that the Sr cations are less stable since they begin to precipitate at lower temperatures. At 800°C, the PBSCF surface is completely covered with particles and "pores" can be observed in some of the grains. These pores suggest that large amounts of Sr and possibly other cations are diffusing out of the lattice to agglomerate on the surface. Above 800 °C, large agglomerates are present, and they all seem to be located on the grain boundaries. This indicates that despite the formation of "pores" the grain boundaries are responsible for much of the Sr diffusion to the surface and eventually act as nucleation sites for the secondary phase growth.

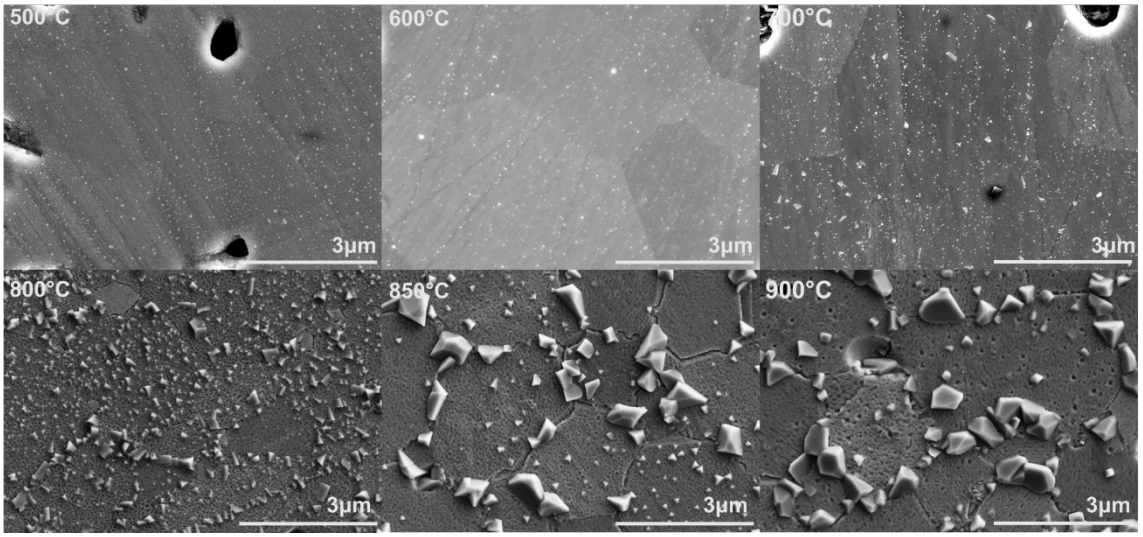

Figure 11. Effect of aging temperature on PBSCF surface microstructure. Samples were aged for 25 hours in synthetic air.

PBSCF surface segregation also demonstrates a different relationship with pO_2 than does LSCF. **Figure 12** shows the effects of aging PBSCF in different pO_2's. Large particles are observed even in pure N_2, suggesting that O_2 is not the only thing needed for particles to nucleate. Compared to the case of LSCF, which have no observable SrO segregation in pure N_2, the layered structure of PBSCF is likely to precipitate cations on the surface.

Also, the grain orientation seems to determine the particle size, suggesting that cation diffusivity strongly depends on the crystal orientation. A similar effect has also been reported in LSCF.[2,3] The relationship between pO_2 and particle size is unclear in PBSCF. "Large" particles are observed at all pO_2's, but the quantity of small particles is reduced in ambient air and at 50% O_2. It is possible that ambient moisture may promote agglomeration of larger particles over the nucleation of smaller ones as seen in LSCF by Niania *et al*.[2] Finally, PBSCF demonstrates less surface segregation with 100% O_2 than with intermediate pO_2 values, which is also the case with LSCF. It appears that oxygen vacancies play an important role in the surface segregation process, but further investigation is needed to determine the relationship between gas environment and the surface segregation process on PBSCF.

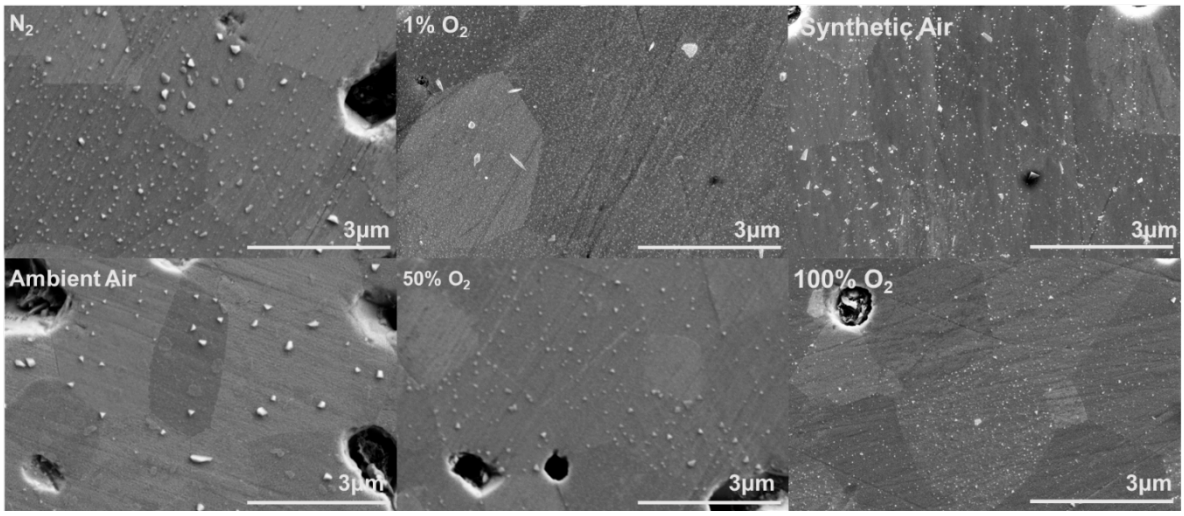

Figure 12. Effect of aging environment on the PBSCF surface. **Samples were aged for 25 hours at 700°C.**

We also observed surface segregation on SSC in a variety of conditions. First, the effect of aging time on the SSC surface was studied. **Figure 13** shows the SSC surface with varying aging time at 700°C in synthetic air. Unlike with LSCF and PBSCF, surface segregation on SSC appears to be concentrated on specific grains rather than across the entire surface. The lighter grains seen at 25 hours form distinct crystallized particles at 50 hours and become "saturated" at 75 hours. At 100 hours, the surface segregation is not limited to these select grains and resembles the microstructure seen in LSCF and PBSCF. The magnified image of one of these grains shows that the particles are primarily growing on the grain with a few seen on nearby grain boundaries. These particles look more like "flakes" than those that grow on the LSCF and PBSCF surface, which resemble distinct particles. It is also clear that the mechanism(s) behind surface segregation in SSC is very different from those in LSCF and PBSCF. In the other cathode materials, the grain orientation affects the quantity and size of the particles formed, but in SSC some orientations appear to act as either nucleation sites or diffusion pathways for cations.

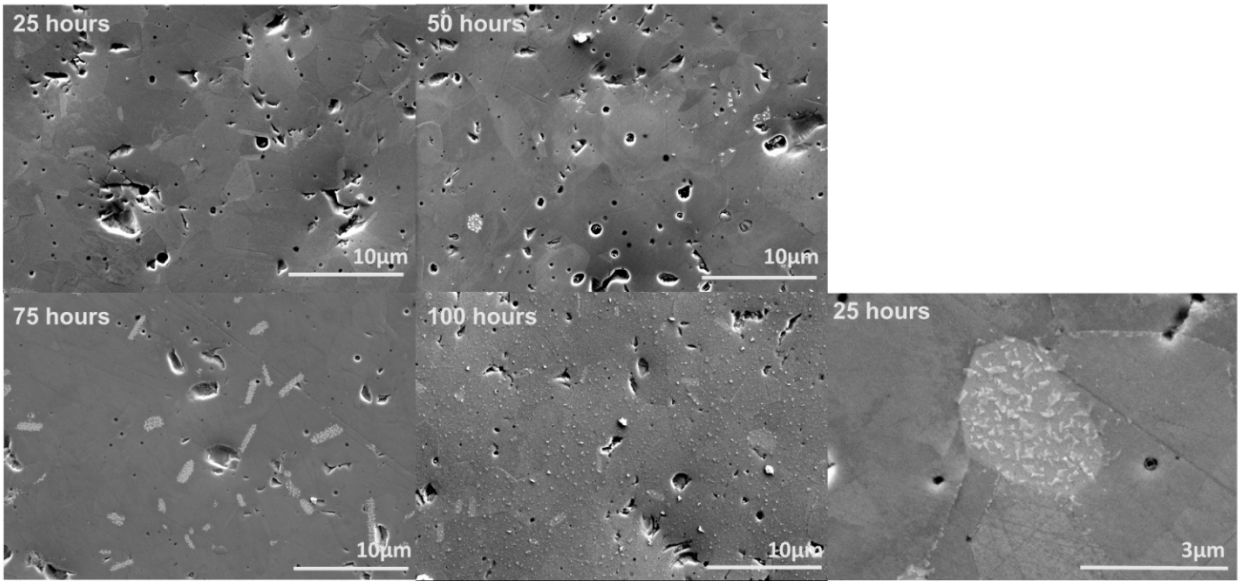

Figure 13. Effect of aging time on the SSC surface. Samples were aged at 700°C in synthetic air. An Enlarged view of the grain for the sample aged for 25 hours is also listed.

To help understand the SSC surface segregation mechanism, EDS was used to study the surface composition of one of these grains. **Figure 14** shows the EDS area mapping for 2 SSC samples with two levels of surface degradation. **Figure 14 (a-c)** shows the EDS on a sample of SSC aged at 700°C for 25 hours in 1% O_2 that exhibits a mild degree of surface segregation but enough that particles are formed in different grains. The sample in **Figure 14(d-f)** shows the EDS mapping on a highly degraded sample of SSC with significant particle segregation all over the surface. This sample was aged in synthetic air for 100 hours at 700°C. In both samples, the featured grain showed a greater concentration of Sm compared to the rest of the surface. The distribution of Sr seemed uniform except for several large distinct particles. This could suggest that grain orientations that terminate with Sm at the surface are less chemically stable. Worth noting is that in the Sm rich regions, there is also a lower concentration of Co and O. Some Sr is still present in these regions suggesting that it is diffusing to the surface and ultimately forming particles. It is unclear exactly what role these Sm-rich regions play in surface segregation, but their presence in a variety of SSC samples suggests that they are important to the mechanisms for surface segregation.

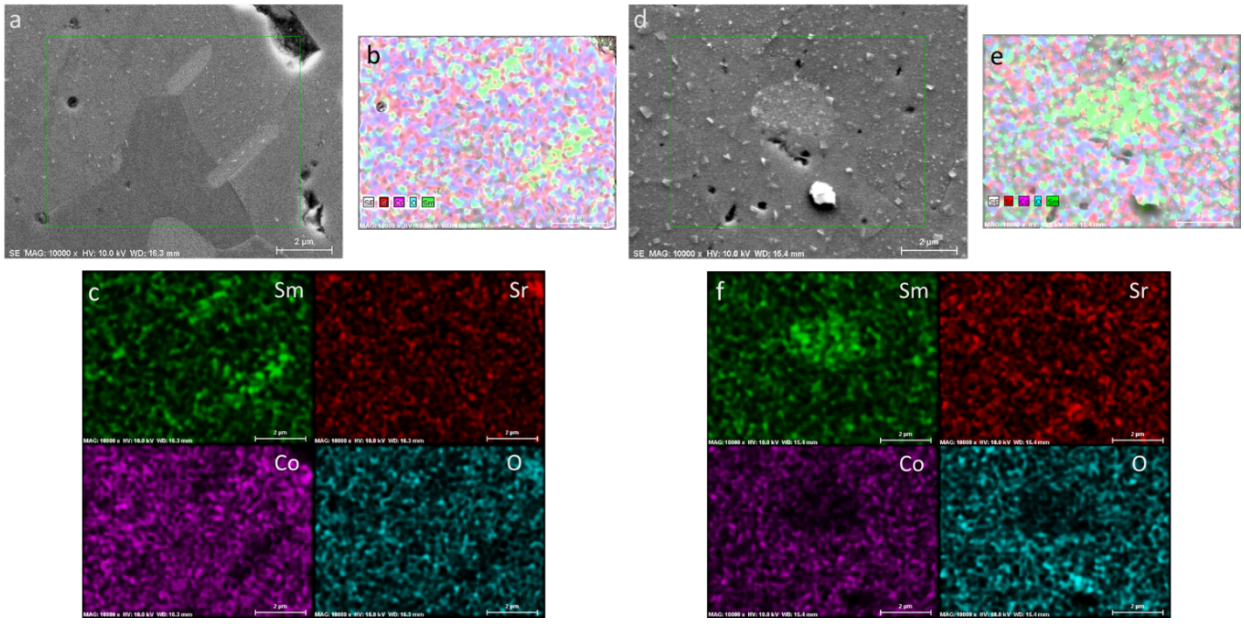

Figure 14. EDS study of SSC aged in 1% O_2 for 25 hours at 700°C. (a) SEM image (b) EDS mapping (c) Elemental mapping EDS study of SSC aged in synthetic air for 25 hours at 700°C (d) SEM image (e) EDS mapping (f) Elemental mapping.

In addition to the effect of aging time. The microstructure of SSC was also analyzed as a function of temperature. In **Figure 15** the SSC surface aged from 500°C to 900°C is shown. Although no precipitated particles are visible at 500°C, there is still a large grain (near the center of the image) that shows the promotion of surface precipitation. There is no significant change from 600°C to 700°C but at 800°C the entire surface exhibits particle coverage, with all the grain boundaries being "filled". Above 800°C the particles agglomerate and pores are visible.

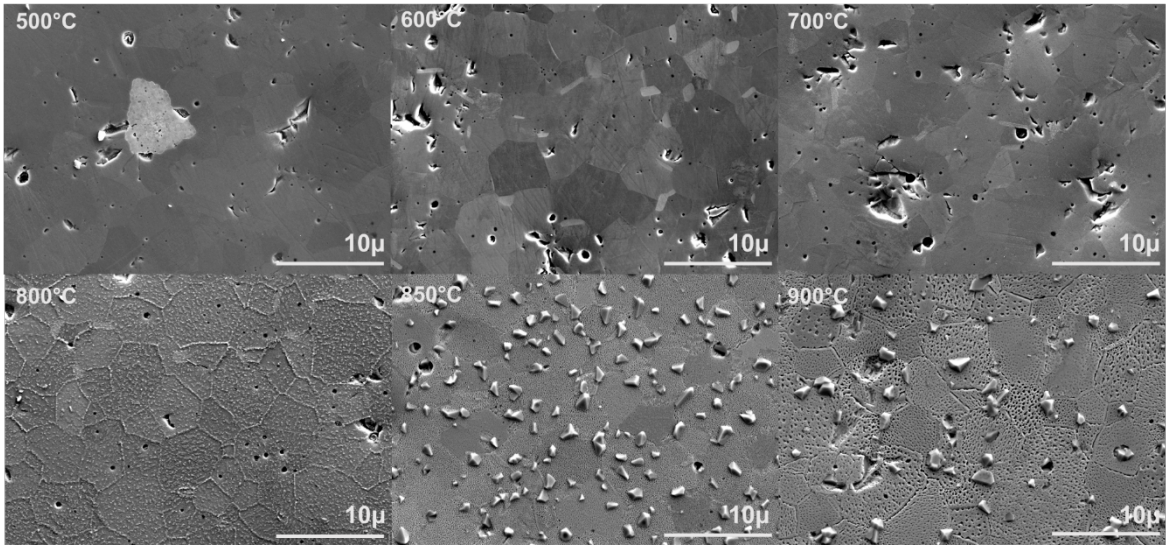

Figure 15. Effect of aging temperature on SSC surface microstructure. Samples were aged for 25 hours in synthetic air.

The agglomeration of large segregated particles is observed for all three cathode materials at higher temperatures, demonstrating that temperature is a major driving force for both cation diffusion and segregated particle growth. One distinction between the SSC and PBSCF is that in SSC, the agglomerated particles are not concentrated on the grain boundaries the way that they are in PBSCF. SSC also demonstrates a mechanism for surface segregation entirely different from LSCF and PBSCF, that is initiated at specific grains rather than throughout the surface.

Determination of Preferable Planes for Surface Sr Segregation

We also showed different cathode segregation processes on $Sm_{0.5}Sr_{0.5}CoO_3$ (SSC), a common low-temperature SOFC cathode. Previously, we demonstrated that study of surface degradation in SSC has a high level of dependence on the grain orientation. Aging SSC initially causes cation segregation in select grains rather than uniformly across the surface. This is in contrast with the particle microstructure varying with grain orientation, as observed in LSCF.

These select grains are observed as light or dark spots on the surface of SSC and were previously reported to be rich in Sm rather than Sr. In an attempt to determine their grain orientation, electron backscatter diffraction (EBSD) was performed on aged SSC to identify the grains of interest. EBSD has already been used on LSCF in prior literature but has not yet been applied to other lower-temperature cathode materials such as SSC or PBSCF. By determining the grain orientation and composition of these unusual grains, it will be possible to propose a unified cation segregation mechanism for different perovskite cathodes.

Figure 16 shows the EBSD mapping and corresponding SEM image of an aged SSC sample (500°C for 25 hours in synthetic air). Using EBSD, we identified different grain orientations, as shown in different highlighted colors. The highlighted grain (orange) shows the strongest cation segregation level. We will compare the grain orientation to the crystal structure and determine why this direction prefers to have cation segregation.

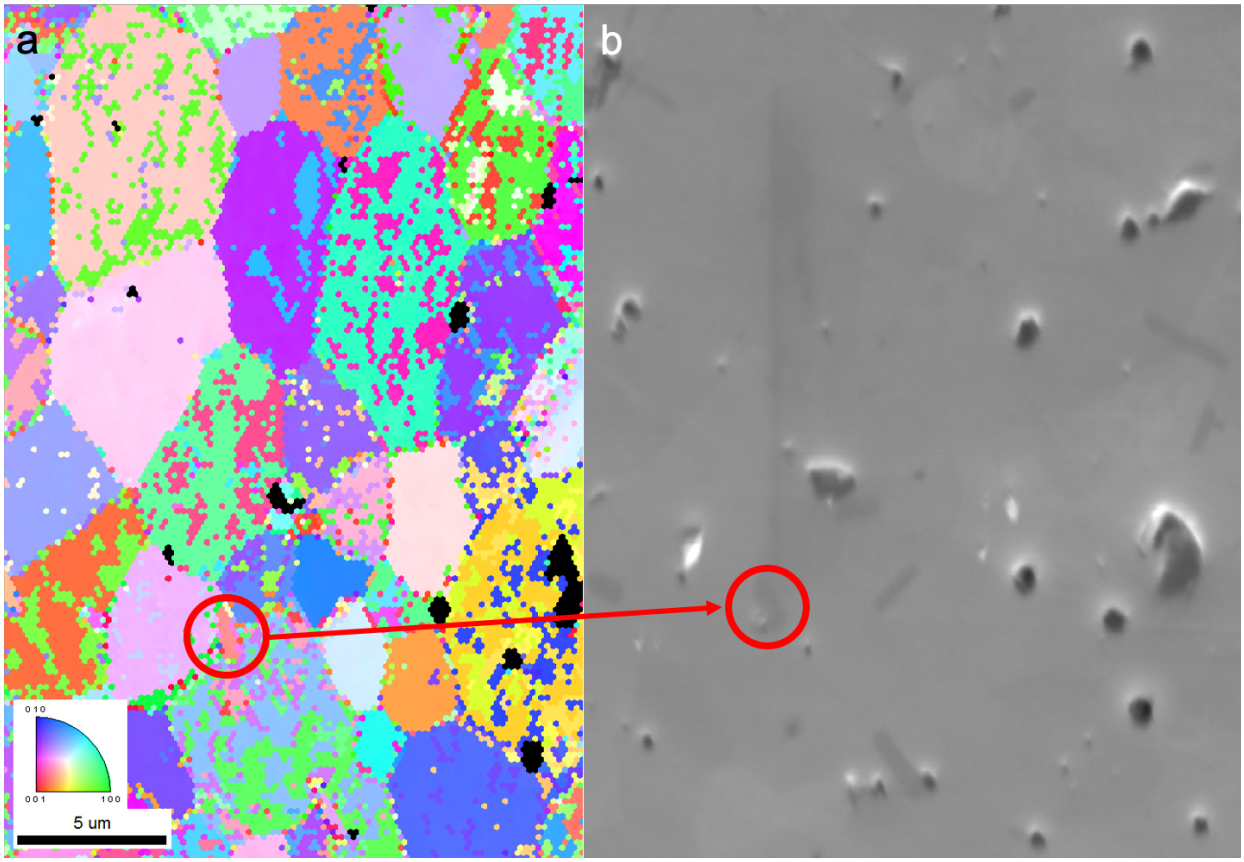

Figure 16. Surface mapping of SSC aged at 500°C for 25 hours in synthetic air. (a) EBSD image of aged SSC. (b) Corresponding SEM image.

Development of ALD surface modification technique

The surface properties of La(Sr)Co(Fe)O_3 (LSCF) were modified through ALD. The validation of ALD process was conducted in the UMD Nanocenter. We first identified suitable metal oxides and corresponding precursors. Titanium oxide (TiO_x) and vanadium oxide (VO_x) were deposited by ALD on three different samples for different purposes: a silicon wafer to calibrate film thickness, a dense cathode material bar sample to determine the ALD effect on surface kinetics of cathode materials, and a porous cathode symmetric cells to determine ALD effects on electrochemical performance.

Dense samples were made by pressing $La_{0.60}Sr_{0.30}Co_{0.20}Fe_{0.80}O_{3-X}$ powder (Fuel Cell Materials) with a hydraulic press. The resulting discs were sintered at 1400°C for 4 hours. The sintered dense discs were polished with SiC abrasives to form a smooth surface and were then cut into rectangular bars that were polished a second time.

Symmetric cells using a 10% Gd-doped Ceria electrolyte (GDC) (Fuel Cell Materials) were formed by pressing the electrolyte powder into pellets and sintering at 1450°C for 4 hours. The sintered pellets were polished before being blade coated with LSCF-GDC composite cathode paste

(Fuel Cell Materials) onto both sides of the pellets. Once dry, the coated pellets were heated in a furnace for 1 hour at 400°C and for 3 hours at 1080 °C.

Evaluation of ALD parameters

The process parameters for depositing high quality films were determined. ALD was performed using a Beneq TFS 500 reactor. The number of cycles and reactor temperature were adjusted to control the deposition conditions. To ensure uniform coating, all samples were placed on custom made sample holders so that all of the active surfaces could be exposed to the reactants. TiO_x was deposited using TDMAT (Tetrakis(dimethylamido)titanium) as precursor and water as oxidizer. VO_x was deposited using VTOP (vanadium tri-isopropoxide) with ozone as an oxidizer. The UMD Nanocenter also offers trimethylaluminum (TMA) and diethylzinc (DEZ) for aluminum oxide and zinc oxide respectively. Due to the fixed oxidation state of Al in aluminum oxide and Zn in zinc oxide, we first examined the ALD deposition process for titanium and vanadium.

Analysis of the ALD film quality and thickness are essential to understanding the kinetics of oxygen diffusion at the surface. **Figure 17** shows the microstructure of dense LSCF with and without ALD modification in different conditions. The unmodified surface (**Figure 17 (a)**) is relatively featureless and so are the surfaces with 750 cycles of TiO_x and 1500 cycles of TiO_x, as shown in **Figure 17 (b) and (c)**. This indicates a smooth and conformal ALD coating on the LSCF surface. In contrast, VO_x deposition at 150 °C formed an uneven coating that consisted of distinct VO_x particles that nucleated on the surface as shown in **Figure 17 (d)-(e)**. When the deposition temperature for VO_x was increased to 175°C, the particles became much smaller (**Figure 17 (f)**). This suggests that the conditions for ALD were not enough to remove all of the precursor from the previous cycle. As a result, the regions with residual precursor served as nucleation sites. This was remedied by increasing the duration of the vacuum purge in between cycles. The increase in temperature improved the microstructure because it increased the evaporation of the precursor. However, VTOP decomposes above 185°C, so increasing the temperature is not an ideal solution.

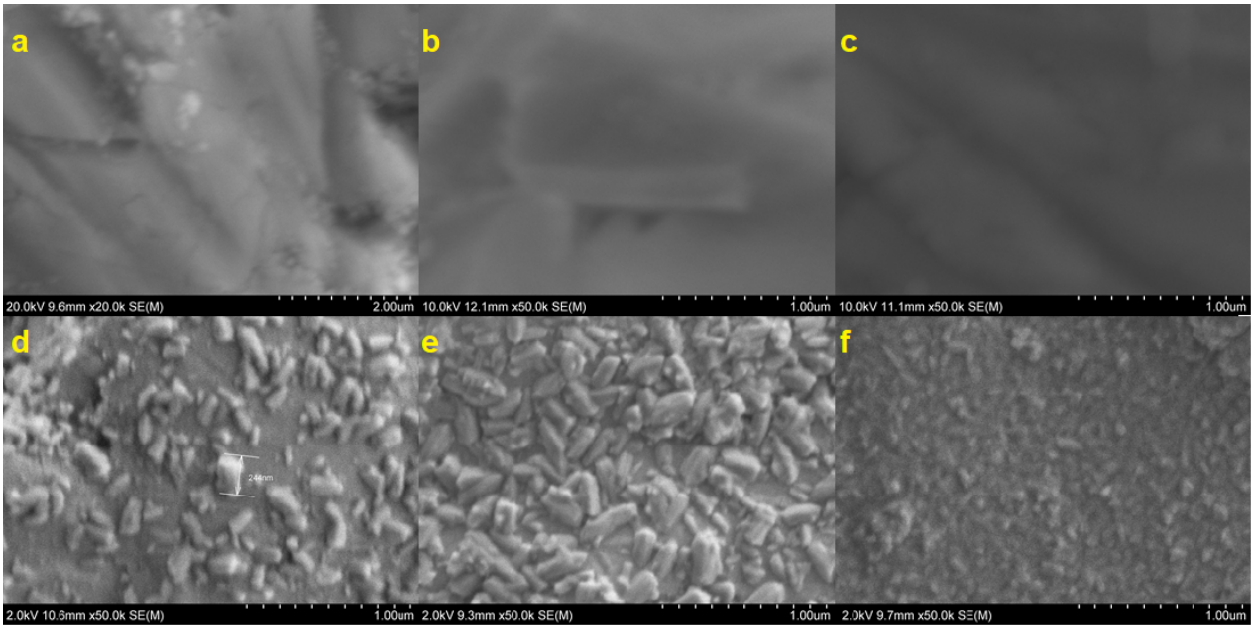

Figure 17. LSCF and ALD microstructure. (a) Unmodified dense LSCF surface (b) 750 ALD cycles of TiO_x at 150 °C (c) 1500 ALD cycles of TiO_x at 150 °C (d) 750 ALD cycles of VO_x at 150 °C (e) 1500 ALD cycles of VO_x at 150 °C (f) 750 cycles of VO_x at 175 °C.

After ALD modification, the film thickness was determined using a Woollam M-2000D Spectroscopic Ellipsometer on Si wafers that were placed alongside the dense and porous samples. The microstructure and elemental composition of the dense samples were then evaluated using a Hitachi Su-70 SEM and corresponding EDS. **Figure 18** shows the film thickness of TiO_x and VO_x ALD based on the number of cycles. The TiO_x film growth per cycle shows a linear dependence at approximately 0.6 Å/cycle. The linear trend between the film thickness and number of cycles is in accordance with the conformal and uniform nature of the TiO_x film. For VO_x, it has a slower growth rate of approximately 0.16 Å/cycle. The thickness/cycle shows a higher deviation than TiO_x because the rough film surface of the VO_x likely contributes to non-uniform growth rates and nucleation of VO_x. The nucleation is likely caused by inadequate precursor removal.

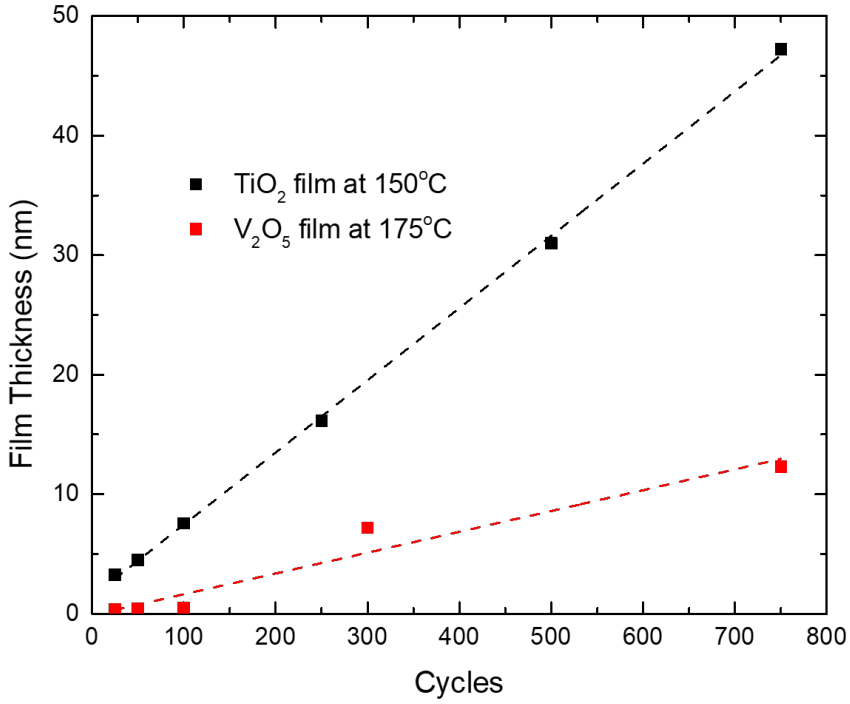

Figure 18. Calibration of ALD deposition cycles versus film thickness for different ALD precursors.

Effects of ALD on surface exchange kinetics were studied using electrical conductivity relaxation (ECR) technique. To prepare the dense samples for ECR, silver wires were attached in a 4-point probe arrangement with even spacing between the wire coils onto the LSCF bars. Each of the wires were then connected to a lead in a custom-built reactor and then hermetically sealed inside. The symmetric cells were coated on both sides with Au paste (Hereaus) and loaded into a custom reactor between two terminals inside a gas-tight reactor. The electrochemical properties were studied on porous symmetric cells using electrochemical impedance spectroscopy (EIS).

ECR and EIS measurements were performed using a 1470E Cell Test System with a 1455A Frequency Response Analyzer (Solartron). Oxygen partial pressure (pO_2) was adjusted by varying N_2 and O_2. A Zirox SGM5 O_2 sensor/pump was used as a pO_2 sensor to analyze the gas environment.

To examine the effects of TiO_x films on surface exchange properties of LSCF (**Figure 19**), a dense sample of LSCF was tested against one modified with 25 cycles of TiO_x ALD at 150 °C. These bar samples were heated in a pure nitrogen atmosphere and the voltage response was measured while a constant current of 20 mA was applied. The ECR curves are displayed in and compare the kinetics of the unmodified and TiO_x modified sample at 700 °C and 800 °C from pure N_2 to pO_2=0.25 atm. The unmodified LSCF is shown to have a faster response at both temperatures than the TiO_x modified sample, suggesting that TiO_x hinders the surface exchange kinetics on LSCF above 700 °C.

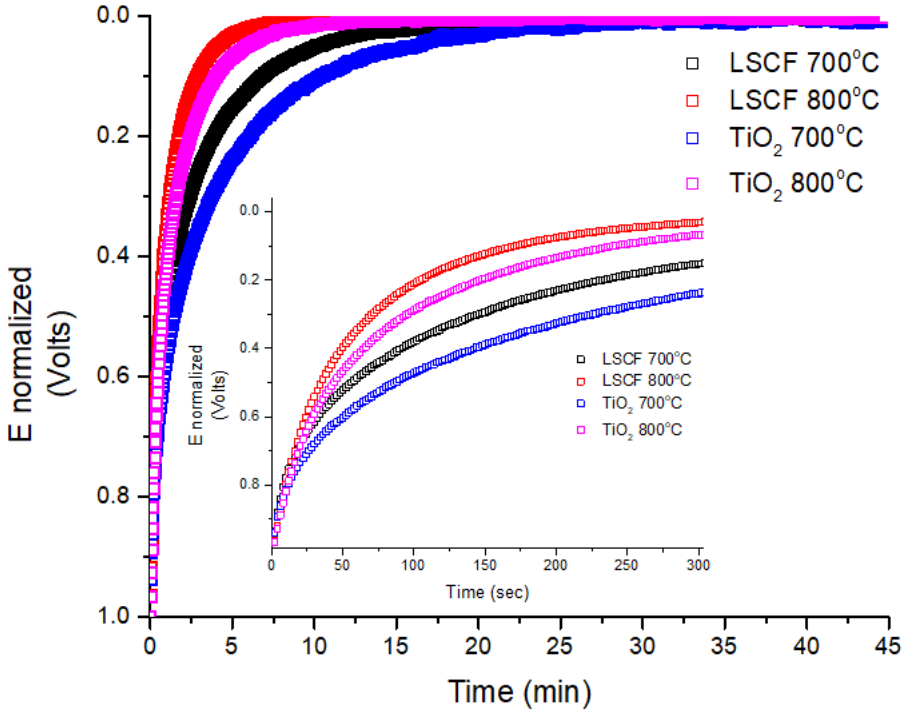

Figure 19. Electronic conductivity relaxation (ECR) curves for unmodified LSCF and ALD modified sample (25 cycles of TiO_x deposited at 150 °C). The curves show the voltage response from a pure N_2 atmosphere to a 25% O_2 atmosphere.

Both TiO_x and VO_x modified symmetric cells were tested to determine the ALD impact on electrochemical properties. The electrochemical properties were studied as a function of both

temperature and pO_2. **Figure 20** shows the impedance curves for LSCF-GDC symmetric cells in air with and without ALD modification. The TiO_x ALD reduces the polarization impedance at all temperatures. In contrast, VO_x ALD increases the non-ohmic impedance of the symmetric cell, and this large increase for the VO_x coated sample could be caused either by the poor film quality or because of the ineffective surface exchange properties of VO_x.

For both the TiO_x and VO_x samples, the impedance was measured while heating up from 500°C to 750°C and while cooling down to 500°C after annealing at 750°C for 2 hours. The impedance curves were found to change for 2 hours at 750°C, the effect of annealing on conductivity was also measured as shown in **Figure 21.** In **Figure 21 (a) and (b)**, the impedance of the TiO_x coated sample appears to increase after annealing at 750 °C, suggesting that the sintering temperature of ALD film plays an important role in electrochemical performance. Compared with ECR results of TiO_x coated LSCF bars, our results suggest that a lower sintering temperature may improve the activity of TiO_x ALD coated LSCF. Such heating may also affect the microstructural properties of the TiO_x film, resulting in coarsening. For the VO_x coated sample, although the annealing process reduced the non-ohmic impedance, it was still far higher than the unmodified symmetric cell.

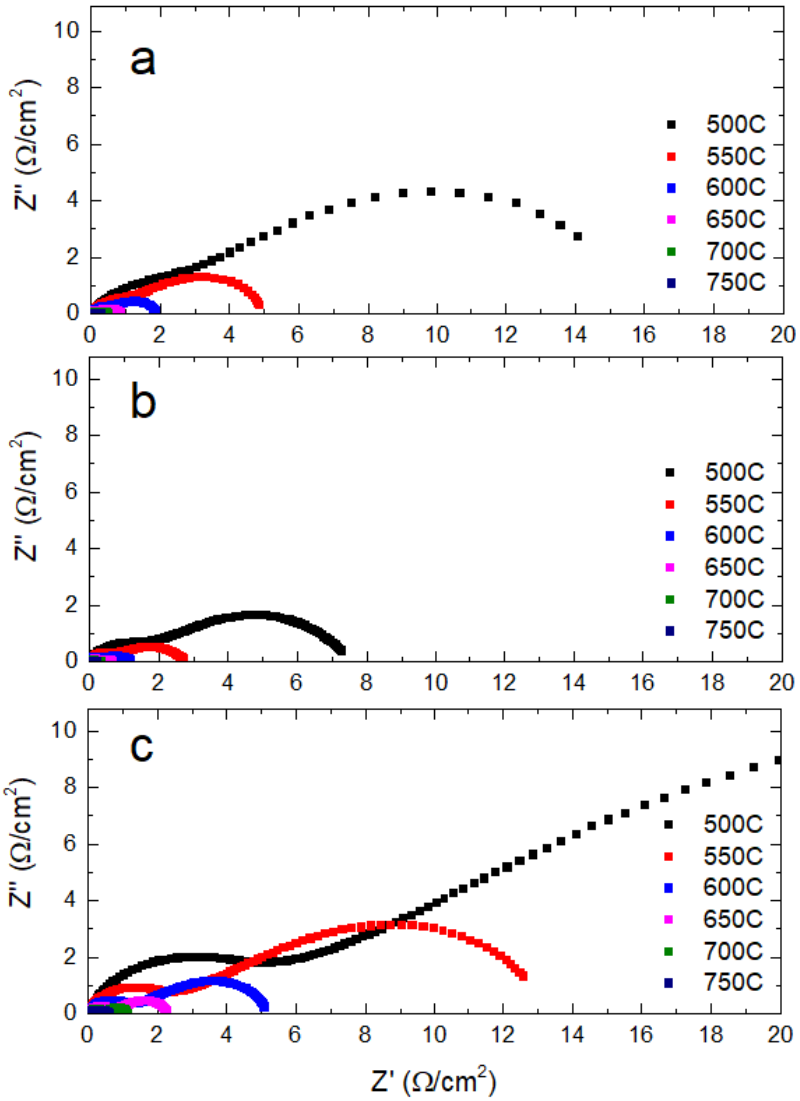

Figure 20. Impedance curves for LSCF-GDC symmetric cells in air with varying temperature. (a) Unmodified LSCF-GDC (b) 25 ALD cycles of TiO_x deposited at 150°C annealed at 750 °C for 2 hours (c) 25 ALD cycles of VO_x deposited at 175°C sintered at 750°C for 2 hours

The pO_2 dependence on the polarization impedance was studied in addition to temperature. **Figure 22** shows Nyquist plots of unmodified and ALD modified symmetric cells at different pO_2 values. For all samples, the non-ohmic impedance decreased with increasing pO_2 due to the increased concentration of oxygen in the sample. The pO_2 dependence was measured after the samples were annealed and the temperature dependence was tested. The pO_2 dependence may be different in the case of unannealed samples and may warrant further investigation. The TiO_x modified sample showed lower impedance than the unmodified sample at all pO_2 values. The VO_x modified sample had higher impedance than the baseline, but the conductivity still increased with pO_2. No drastic changes were observed with pO_2 suggesting that neither the TiO_x phase nor the VO_x phase are changing with pO_2.

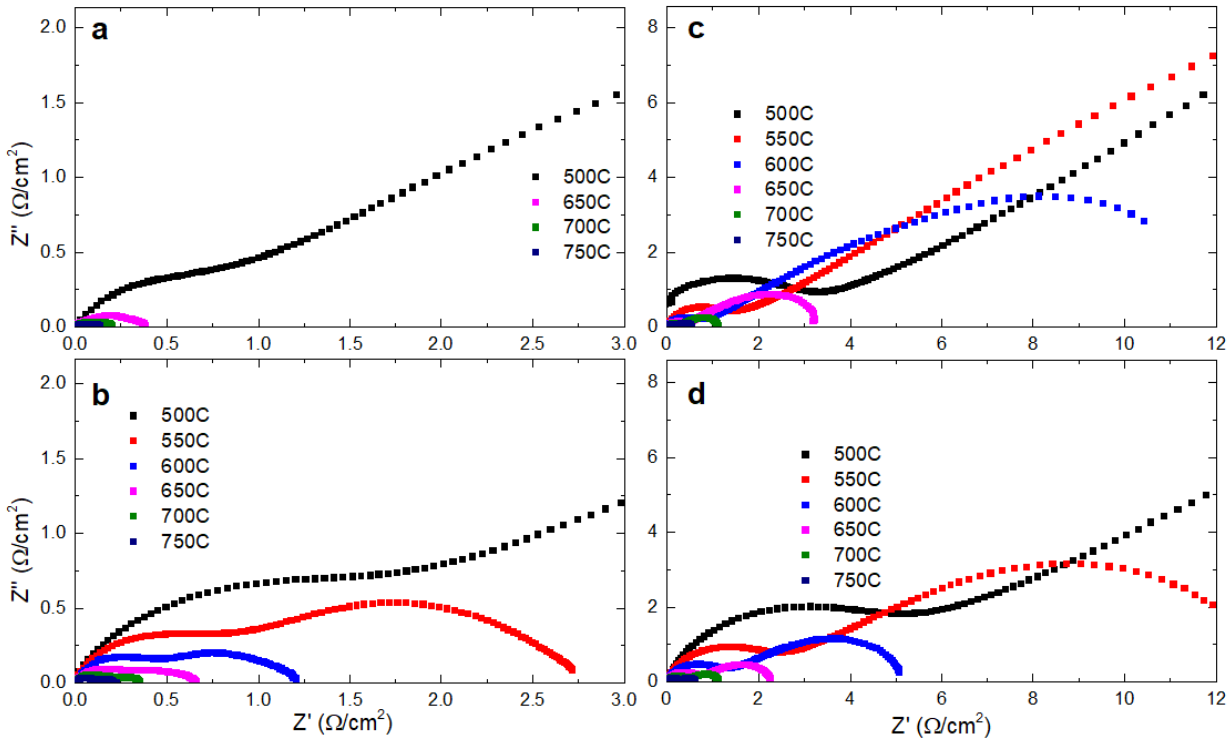

Figure 21. Comparison of impedance curves for ALD modified samples before and after annealing at 750 °C. (a) 25 ALD cycles of TiO_x before annealing (b) 25 ALD cycles of TiO_x after annealing (c) 25 ALD cycles of VO_x before annealing (d) 25 ALD cycles of VO_x after annealing.

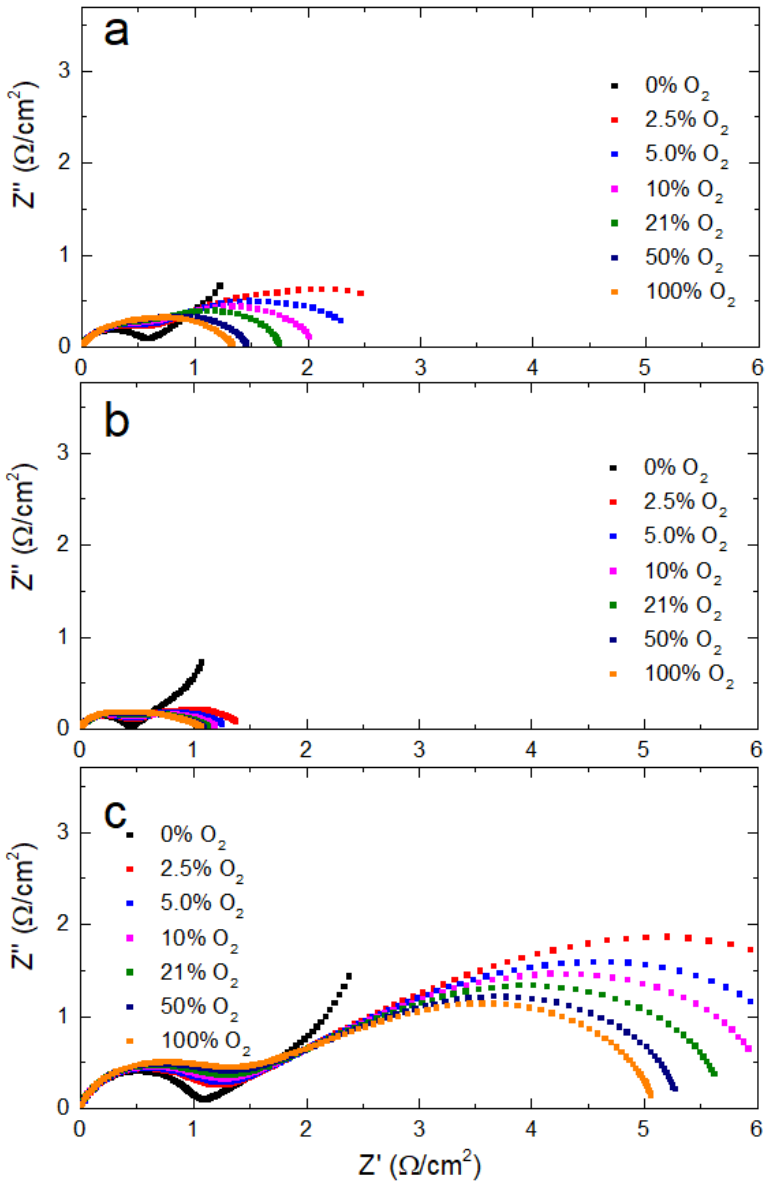

Figure 22. ALD coating effect on porous LSFC-GDC symmetric cells under a wide range of oxygen partial pressures (pO_2). Nyquist plots for (a) unmodified LSCF-GDC, (b) LSCF-GDC with 25 ALD cycles of TiO_x deposited at 150°C annealed at 750°C for 2 hours (c) LSCF-GDC with 25 ALD cycles of VO_x deposited at 175°C annealed at 750°C for 2 hours.

The temperature and pO_2 dependence of the ASR of unmodified and modified symmetric cells are summarized in **Figure 23**. Compared to the unmodified cell, TiO_x modified cell shows a lower ASR in all tested temperature region. In contrast, VO_x modified cell shows an opposite trend with an increase in ASR. **Figure 23 (b)** compares the temperature dependence for modified cells before and after sintering at 750 °C for 2 hours. The hypothesis is that the sintering of modified cells could trigger chemical reactions between ALD films and LSCF backbone, causing different effects. Results show that the high-temperature sintering process degrades the electrochemical

performance of TiO_x modified cell, but VO_x modified cell shows an improvement in the ASR, suggesting that a higher temperature is necessary to activate VO_x modified LSCF-GDC cell.

Figure 23 (c) shows the double log plot of pO_2 versus ASR for unmodified and modified cells. Unmodified cell has a slope of 0.22. TiO_x modified cell has a lower ASR across all pO_2 range with a decrease in the slope.

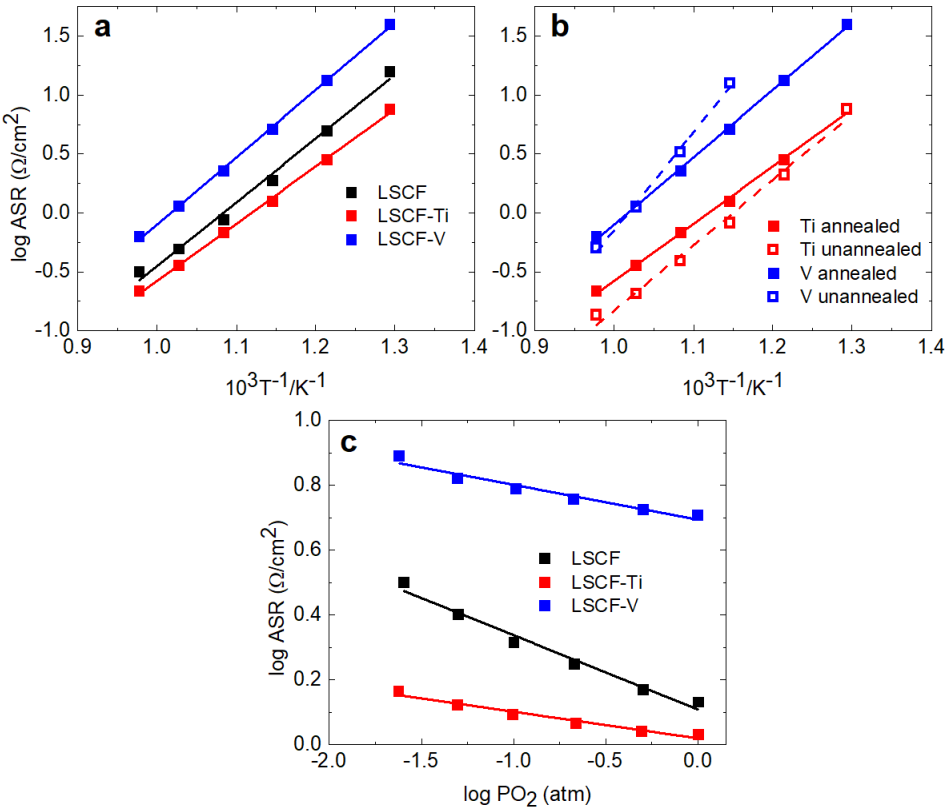

Figure 23. Temperature and pO_2 dependence on the polarization resistance of unmodified and ALD modified cells. (a) Arrhenius plot of ASR of unmodified, TiOx, and VOx modified cells. (b) Arrhenius plot of modified before/after sintering at 750°C for 2 hours. (c) pO_2 dependence of unmodified LSCF and ALD modified samples after annealing.

Analysis of the ECR and EIS data indicate that nanoscale films have a considerable effect on the kinetics of LSCF cathodes. Our results show that sintering temperatures of ALD films has a direct impact (either beneficial or deleterious) on fuel cell cathode performance. Experiments such as ECR and long-term aging studies need to be performed at lower temperatures to properly determine the properties and effectiveness of the ALD films. Determination of the mechanism for film degradation will allow optimization of the ALD films.

ALD film optimization entails determining the ideal amount of cycles as well as the ideal deposition temperatures for the ALD films. The composition of ALD films may also be modified

to allow them to retain their improved performance even at higher temperatures. This research will then be extended to anode materials.

Study of Kinetics and Degradation on ALD Modified Surface

A thin layer of Ti, V, Zn, and Al was deposited on the dense LSCF bar using ALD, and electrical conductivity relaxation (ECR) was used to determine the surface exchange kinetics of the modified LSCF surface. In addition to studying the effects of surface modification on kinetics, the effects of each ALD film on surface microstructure were also compared to unmodified LSCF. ALD of Ti, V, Zn, and Al were done on dense LSCF samples, and the surface microstructure after testing was compared to tested unmodified and aged (before testing) LSCF.

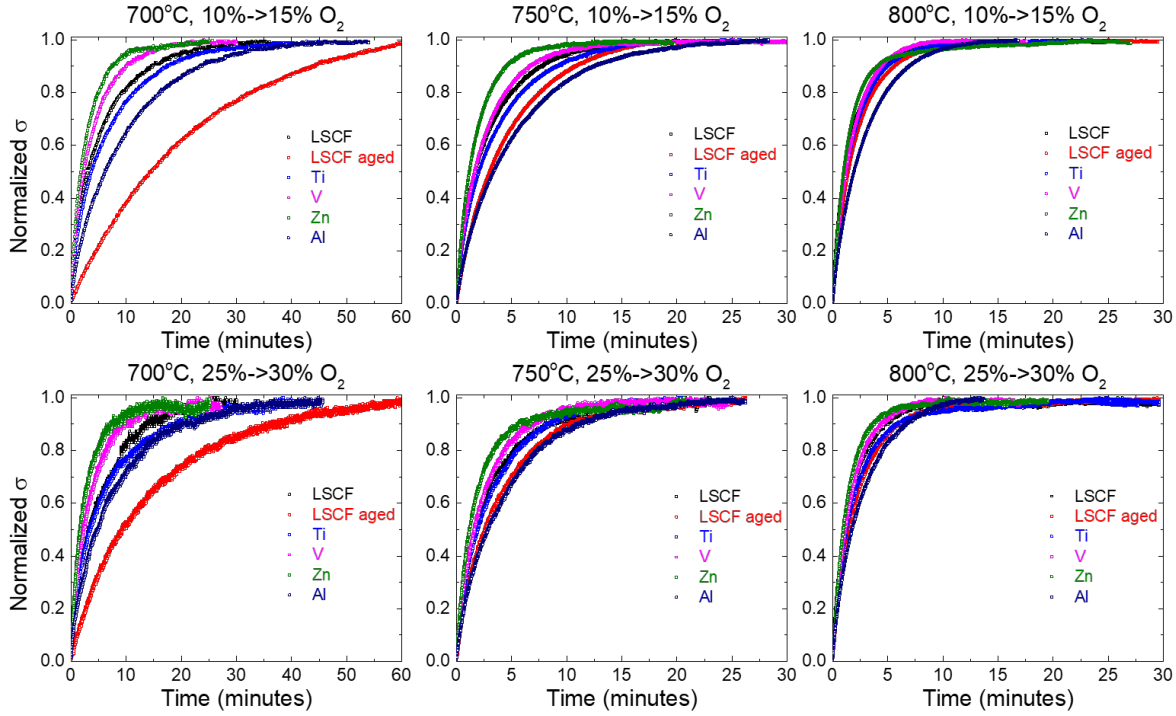

Figure 24. Oxygen Exchange Kinetics on ALD modified LSCF. ECR curves for unmodified and ALD modified LSCF shown for 2 steps 10% to 15% O_2 and 25% to 30% O_2 at 700, 750, and 800 °C.

Figure 24 shows the ECR measurements for LSCF in a variety of conditions. The ALD modified samples demonstrated different performance based on the composition of the film. V and Zn demonstrated improved performance, Ti was similar to that of the baseline, while Al exhibited the slowest response. As expected, the sample of LSCF that was aged prior to ECR measurements exhibited worse performance than the baseline LSCF but was in some instances better than the Al modified LSCF. Higher temperatures improved the kinetics for all samples as expected but higher temperatures also increase the rate of degradation and surface particle agglomeration as discussed previously. For that reason, it is important to consider the compositions had the best performance at lower temperatures, which happened to be Zn and V. Thin films of Zn and V showed improvement compared to the baseline at all temperatures and steps.

Following the study of ECR, the surface of the tested samples was then compared to prior work on SrO segregation. **Figure 25** shows the difference in microstructure after performing ECR measurements for unmodified samples. The surface microstructure after ECR is comparable to aging LSCF at 700°C for 25 hours. The aged LSCF was aged prior to ECR by being exposed to an atmosphere of 80% CO_2 and 20% O_2 for 25 hours at 700°C. The aged sample had more surface coverage than the unaged sample after it was tested. After the aged sample was tested, the surface showed large agglomerated particles and a rough pattern on the surface. The large particles resemble those formed at 850°C and 900°C but the rough features visible in the grains have not been seen elsewhere.

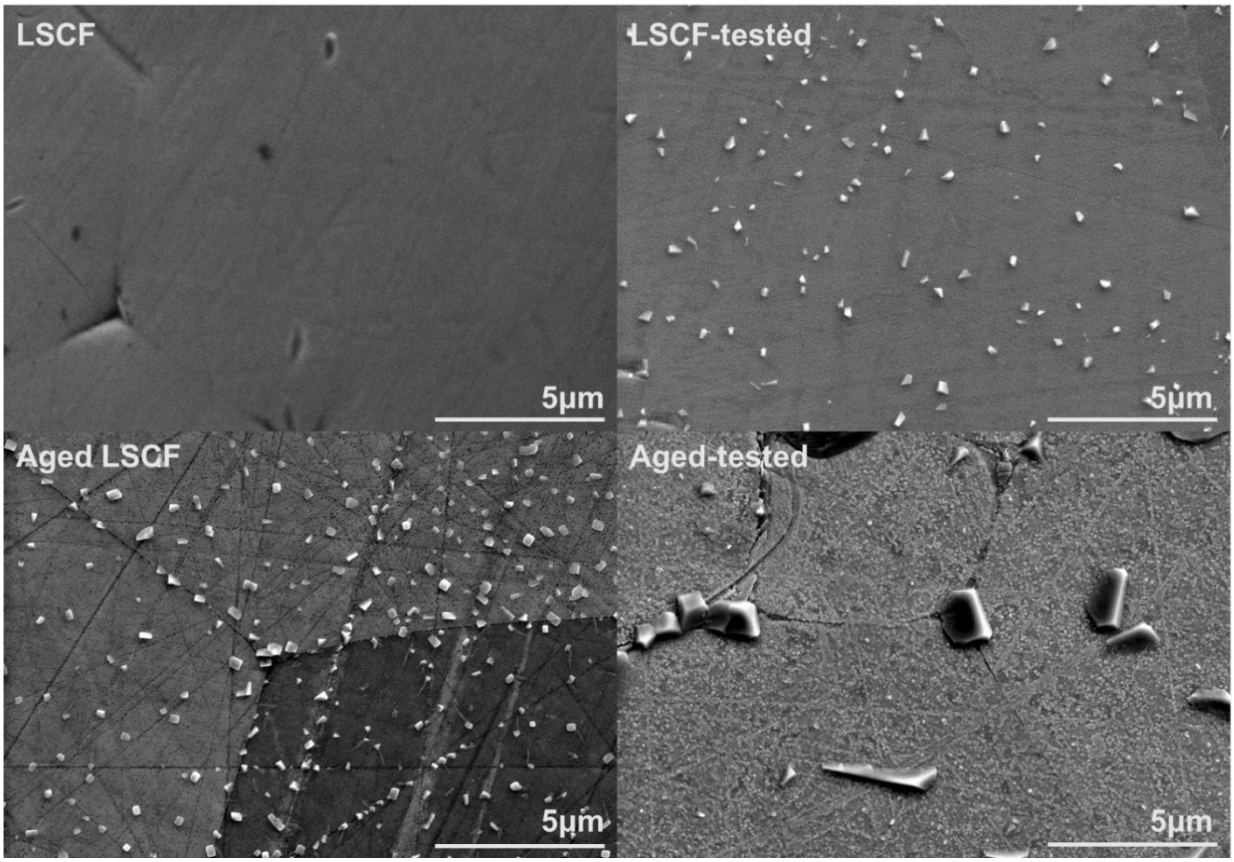

Figure 25. Microstructure of unmodified baseline and aged LSCF surface before and after ECR measurements.

The ALD modified LSCF was characterized prior to ECR measurements. **Figure 26** shows the fresh ALD coated LSCF surface as well as after ECR measurements were performed. For all three precursors, no changes to the surface from ALD are visible. The low number of cycles results in a very thin film too that is difficult to be detected using. Following ECR measurements, all of the ALD modified samples exhibited surface segregation. The Ti and Zn coated LSCF samples showed a larger number of particles that were also smaller than those that appeared on the V coated sample.

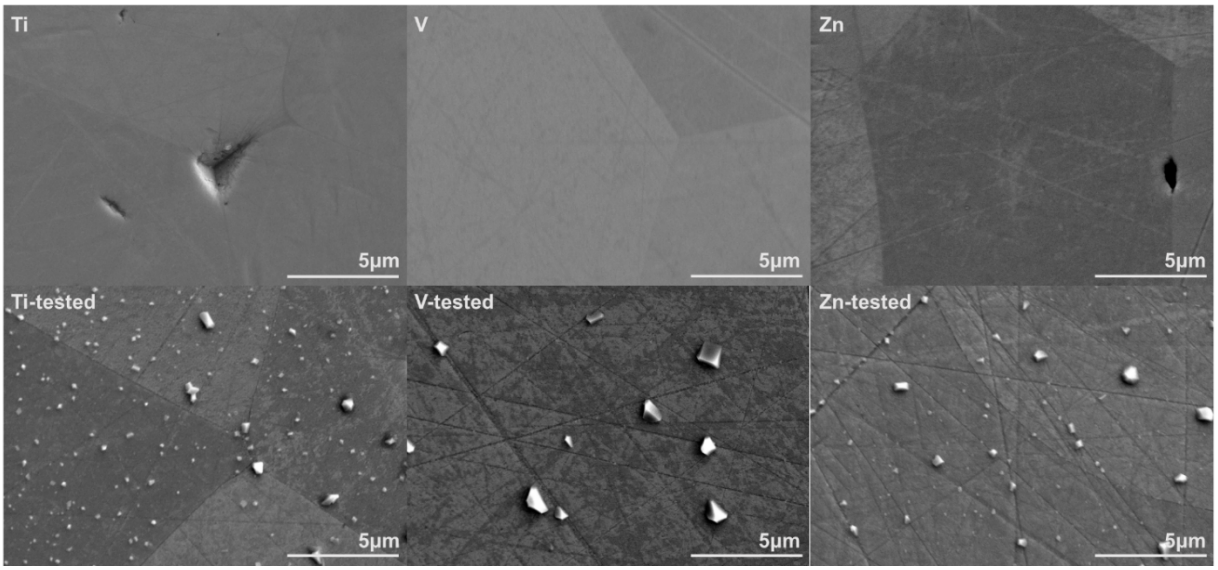

Figure 26. ALD modified LSCF before and after ECR measurements.

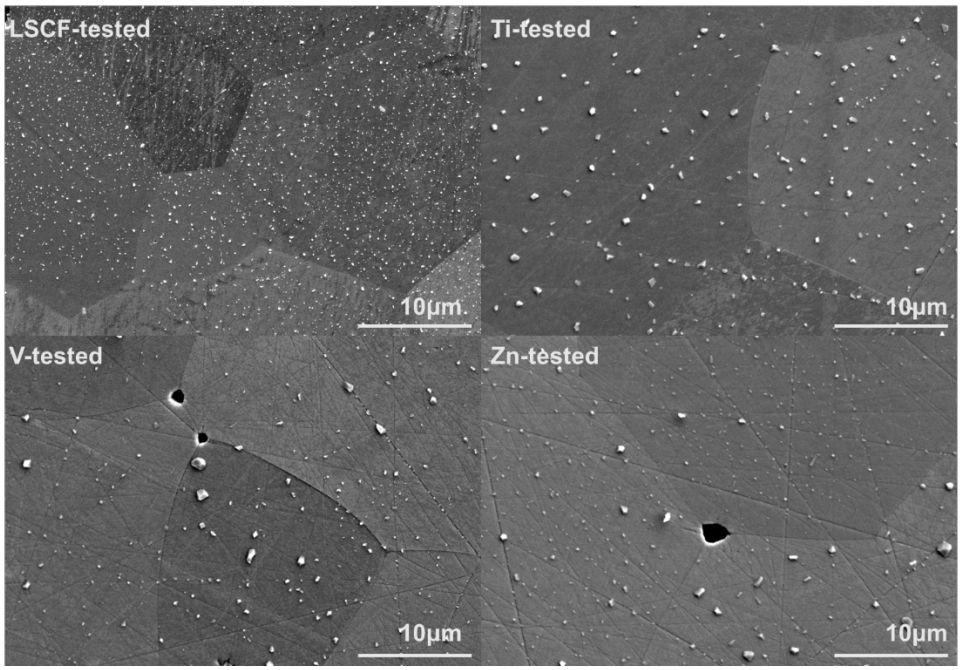

Figure 27. Comparison of unmodified LSCF to ALD modified LSCF before and after ECR measurements.

The ALD films have some effect on the LSCF surface regarding surface SrO segregation. **Figure 27** shows the difference in each sample after testing. All the modified samples exhibit larger particles after testing that the unmodified LSCF. An in-depth study of the effect of each thin film would have to evaluate the effect of varying film thickness on surface microstructure for each composition. A more controlled study of kinetics, microstructure, and film properties is needed to determine the exact effects of each thin film on the microstructure.

ALD Modification of Aged LSCF

To further understand how ALD affects the surface of LSCF after SrO segregation, ALD was performed on samples that had already undergone aging. The surface SrO segregation level was tuned by controlling the aging conditions of LSCF (80% CO_2 and 20% O_2 for 25 hours at 700°C). We performed ALD coating on SrO segregated surface and then determined the activity of samples. This could result in the formation of new SrO containing phases that may not be present in the case of deposition on a pristine LSCF surface. **Figure 28, Figure 29,** and **Figure 30** show the electrical conductivity relaxation (ECR) measurements for pristine and aged LSCF compared to ALD (25 cycles of each precursor, Ti, V, and Zn, respectively, at 150°C).

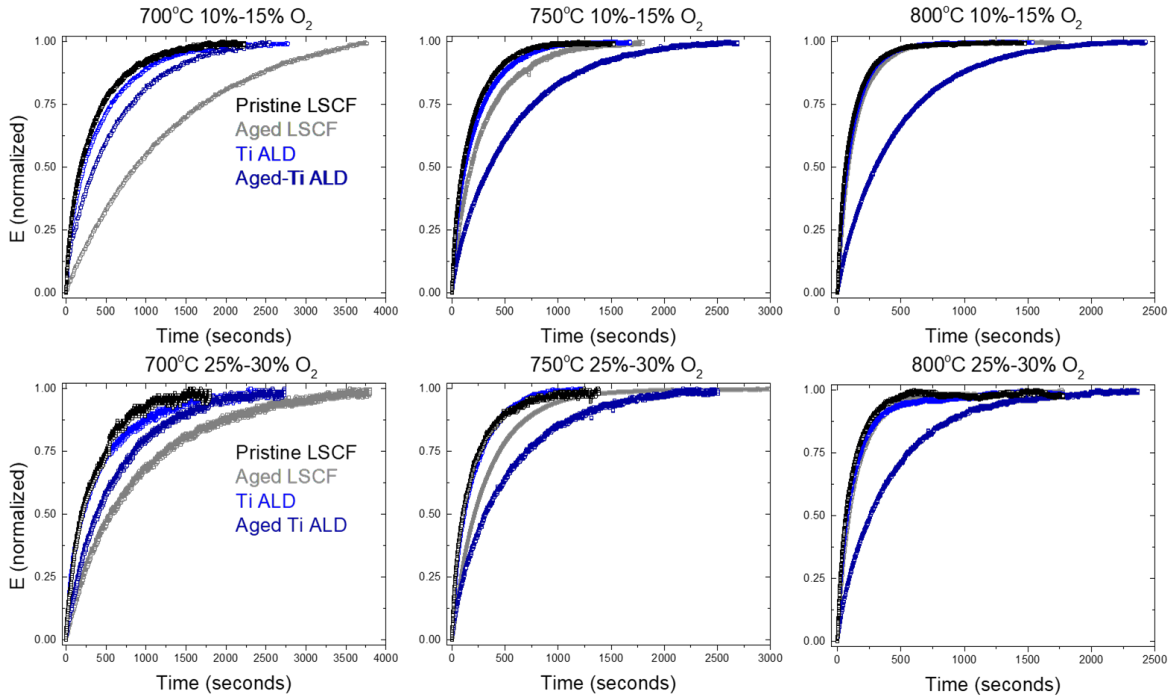

Figure 28. ECR curves for LSCF that has been aged with and without TiO_2 ALD compared to pristine LSCF with and without TiO_2.

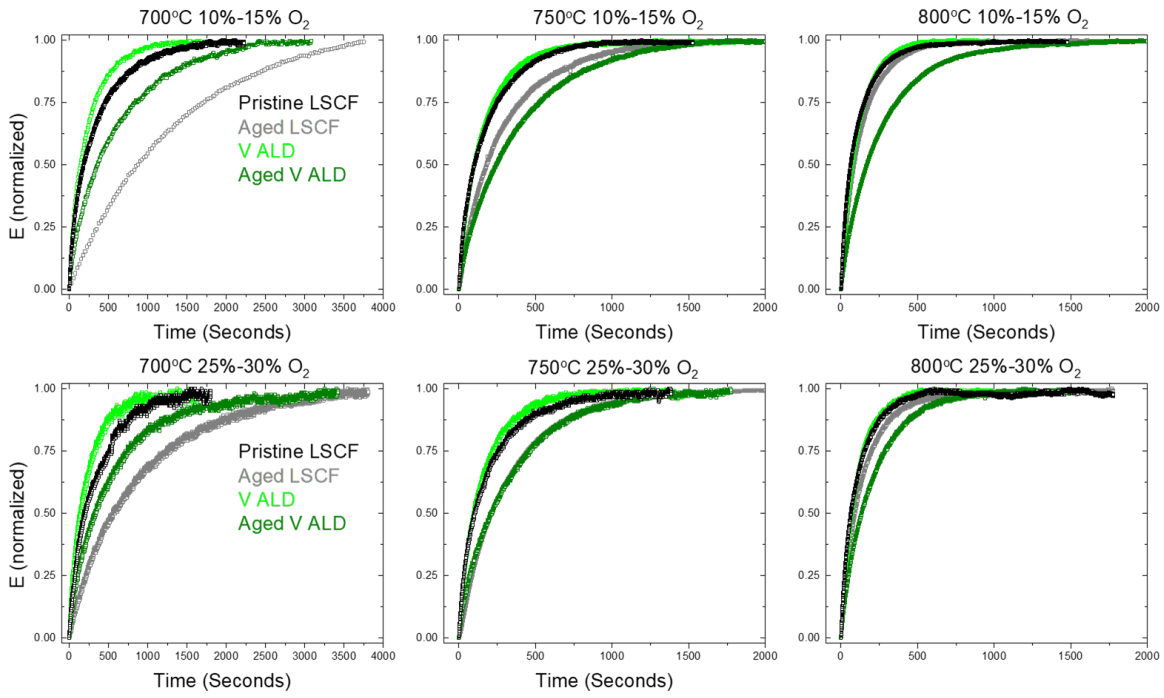

Figure 29. ECR curves for LSCF that has been aged with and without V_2O_5 ALD compared to pristine LSCF with and without V_2O_5.

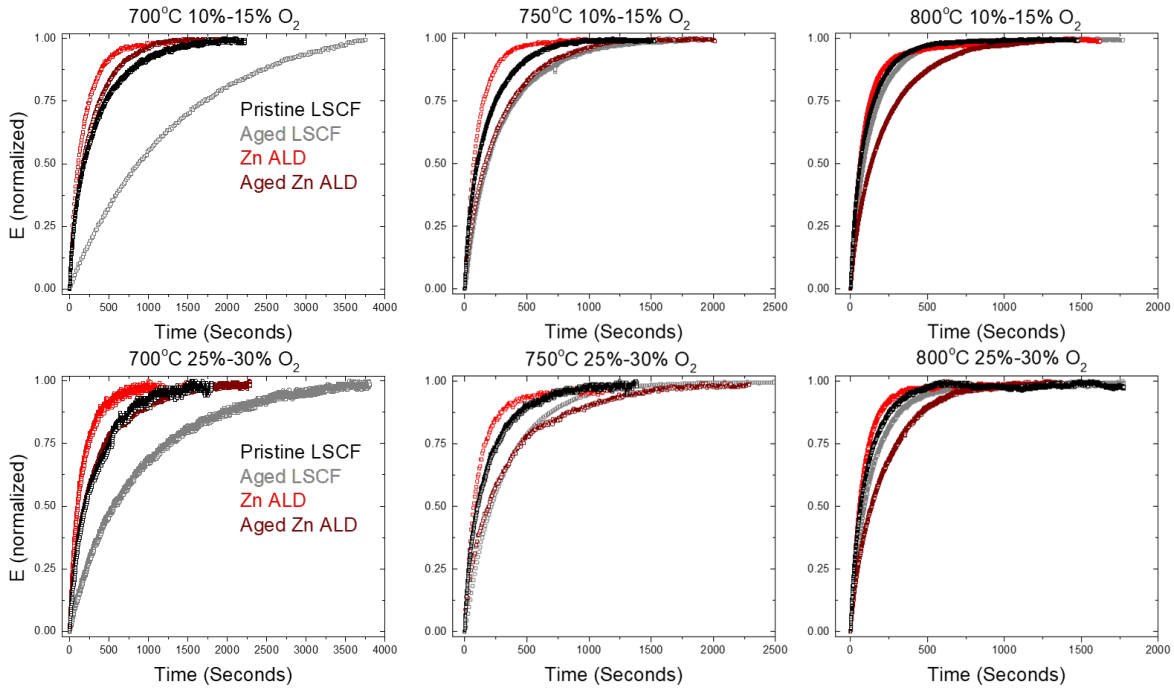

Figure 30. ECR curves for LSCF that has been aged with and without ZnO ALD compared to pristine LSCF with and without ZnO.

ECR was performed between 700 and 800°C under a rapid change in pO_2 from 10% to 30% O_2. ECR results of Ti ALD modified LSCF is shown in **Figure 28**. ECR of Pristine LSCF is shown in black, and the aged LSCF shows a slow response (grey) because of the SrO formation.

The kinetic response becomes faster at 700°C once the aged LSCF sample surface was modified with Ti ALD, which is labeled as "Aged Ti ALD" in **Figure 28**. The Ti ALD coated on the fresh LSCF sample is also shown for comparison (Ti ALD), which shows modest differences between the two unaged samples. However, in the case of TiO_2 ALD on aged LSCF, a substantial difference can be seen in the modified and unmodified aged LSCF. At 700°C the modified aged sample showed better performance but this improvement completely reversed at 750°C and above. This suggests that there was likely a reaction between the surface of the aged LSCF and the TiO_2 film.

Figure 29 shows the effect of vanadium oxide ALD on aged and pristine LSCF. Similar to TiO_2, the vanadium oxide only improved the performance of the aged sample below 750°C and the improvements to the pristine sample were modest.

Figure 30 shows that this is also the case for ZnO films. The ZnO modified aged LSCF did, however, demonstrate performance better than or similar to pristine LSCF depending on the pO_2. Since titanium, vanadium, and zinc oxide films showed worse performance than the aged sample at higher temperatures, it is clear that any new phases that form hinder oxygen kinetics. Further analysis is needed to determine their composition though it is clear that the films are more effective at lower temperatures. There is also the possibility that the inhomogenous surface created by the aging process results in a poor quality film but this does not account for the case of ZnO having better performance than the pristine LSCF at lower pO_2 and temperature. This study demonstrates the utility of ZnO thin films for enhancing LSCF oxygen kinetics.

ALD Conditions and Cathode Kinetics

The choice of oxidizer and other conditions during the ALD process have a profound effect on the thin film composition and properties. These effects can be used as a means of enhancing electrode performance. Understanding the general impact of parameters or processes on film properties and cathode kinetics is very important because a general methodology can be applied to surface modification techniques in general. A process such as annealing that can improve performance is valuable especially in the case of ALD where different groups using different parameters and equipment report different results, even for the same type of film.

The symmetric cells were coated with 16 cycles of TiO_2 ALD at 150 °C using TDMAT as a precursor. The pulse time for TDMAT was 1 second and a 10 second purge time was added between each precursor and oxidizer pulse to ensure diffusion into the porous cathodes. To tune crystallinity and/or oxygen content, both water and ozone were tested as oxidizers. In both cases a pulse time of one second was used. As reported previously, after ALD, the samples were coated with gold paste to form a current collector and then loaded into the reactor. The samples were heated in ambient air. The N_2 annealed samples was heated in a pure nitrogen environment up to

400 °C, then left that way for one hour. The annealing environment was measured to be around 90 ppm of O_2 using a Zirox pO_2 sensor. This oxygen sensor was also used to verify the gas environment used for pO_2 dependence measurements. The gas environment was adjusted by controlling the flow rates of O_2 and N_2, with a constant total flow rate.

After annealing the gas environment was changed to synthetic air and then the sample was heated to 500°C and subsequently 600°C. Measurements were taken at 500°C and impedance was measured as a function of pO_2 at 600°C. The impedance of the samples in synthetic air were measured 3 times; upon initially reaching 600°C, after measuring in low pO_2 and after measuring in high pO_2. The complete order was 20.6% O_2, 100% N_2, 5% O_2, 10% O_2, 20.6% O_2, 50% O_2, 100% O_2, and 20.6% O_2. This was done to determine the effect of the oxygen environment on the films and the reversibility of any effects caused by annealing.

The impedance of each sample in synthetic air at 500°C is shown in **Figure 31.** All of the coated samples showed improved performance compared the uncoated cathodes. The use of water as an oxidizer is shown to have lower impedance than ozone. The use of N_2 annealing results in a further reduction in impedance with the water annealed sample (H_2O-N_2) showing the least impedance.

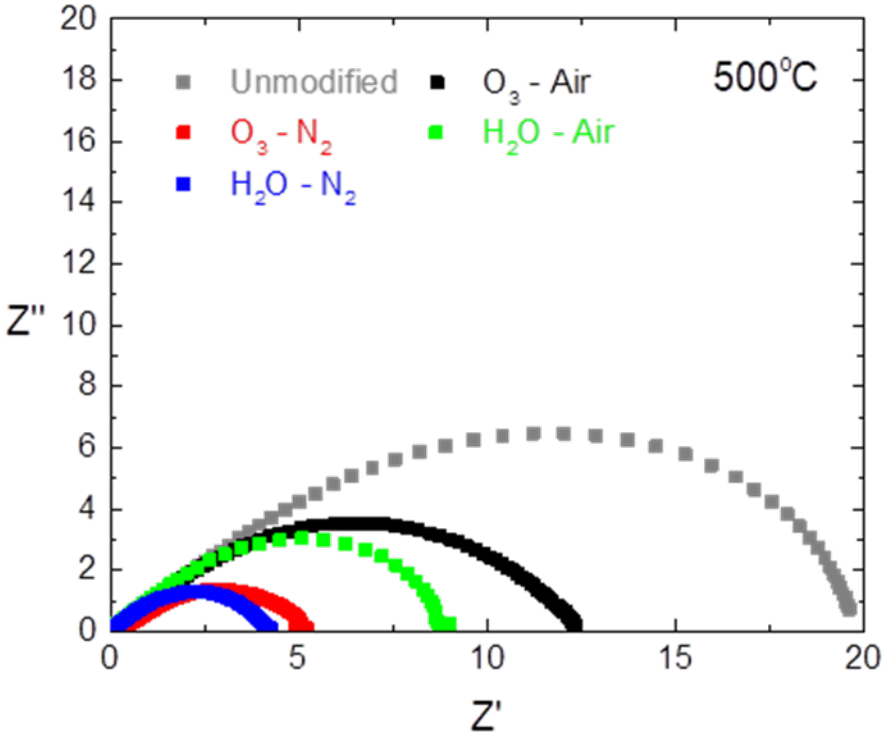

Figure 31. EIS spectra of TiO_2 coated symmetric cells with different oxidizers, with and without annealing.

The plot of pO_2 dependence is shown in **Figure 32.** The ozone sample without annealing (O_3-Air) showed greater impedance than the uncoated sample. The remaining samples continued to show reduced impedance and the sample with lowest impedance was still the annealed and water oxidized sample. All of the coated samples are seen having a non-linear dependence on pO_2, which

is not seen in the uncoated symmetric cell. The slope is steeper at lower pO_2 values and then becomes more flat as pO_2 increases. The effect of oxidizer on the slope was greater than the effect of annealing. Of the coated samples, the O_3-Air sample appears to have the most shallow slope.

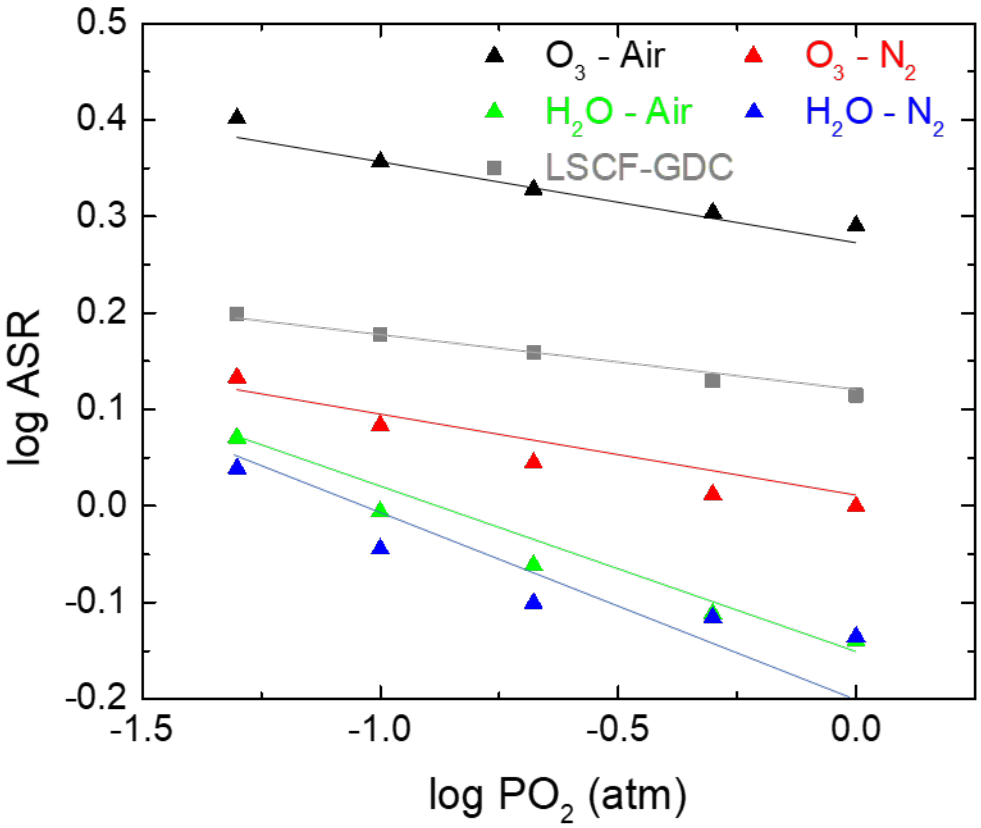

Figure 32. Plot of pO_2 dependence of total ASR. Lines are only intended to show general trends.

Adopting ALD for Porous Cathodes

ALD is typically used for deposition of films on flat, uniform substrates and needs to be adjusted to allow conformal deposition on porous and polycrystalline substrates. Porous substrates introduce variables as a result of their surface area and tortuosity which affect the flow of the gaseous ALD precursor, which is further complicated by the design of the ALD machine itself. Additionally as the film is deposited, it would affect the flow of gas through the porous substrate by tightening the paths for gas diffusion. Uniform ALD requires that all of precursors from the previous cycle has reacted with the substrate or diffused out so that the film can be uniform. Literature on ALD for porous substrates has reported significantly longer purge times than those that were used in our previous experiments. The recipe for TiO_2 ALD was modified accordingly to have a slightly longer pulse time (1 second instead of 0.5) and much longer purge time (10 seconds instead of 1). The recipe for TiO_2 ALD was modified instead of V_2O_5 because it was less complex due to not being reliant on ozone and higher deposition temperatures. The ZnO ALD

recipe can also be modified but it was able to improve performance using just the default recipe as seen in **Figure 33**.

Figure 33 shows the effect of ZnO ALD and the new recipes for TiO_2 as deposited on LSCF-GDC symmetric cells as a function of temperature. Based on the EIS, the ZnO deposition improved symmetric cell performance while the impact of TiO_2 ALD was heavily dependent on the number of cycles. The performance of tested symmetric cells was TiO_2-16 cycles > ZnO-25 cycles > Unmodified LSCF-GDC > TiO_2-25 cycles > TiO_2-9 cycles. It is unknown why 9 cycles of ALD demonstrated the worst performance but it is hypothesized that the deposition may not have been sufficient to form a conformal and crystalline film. It can also be observed that the samples with 9 and 25 cycles of ALD have an additional impedance arc that is not visible in the 16 cycle sample. It is unclear why that is, and further analysis such as the advanced impedance spectroscopy analysis, distribution of relaxation time (DRT) is needed to determine the mechanism behind hindered performance.

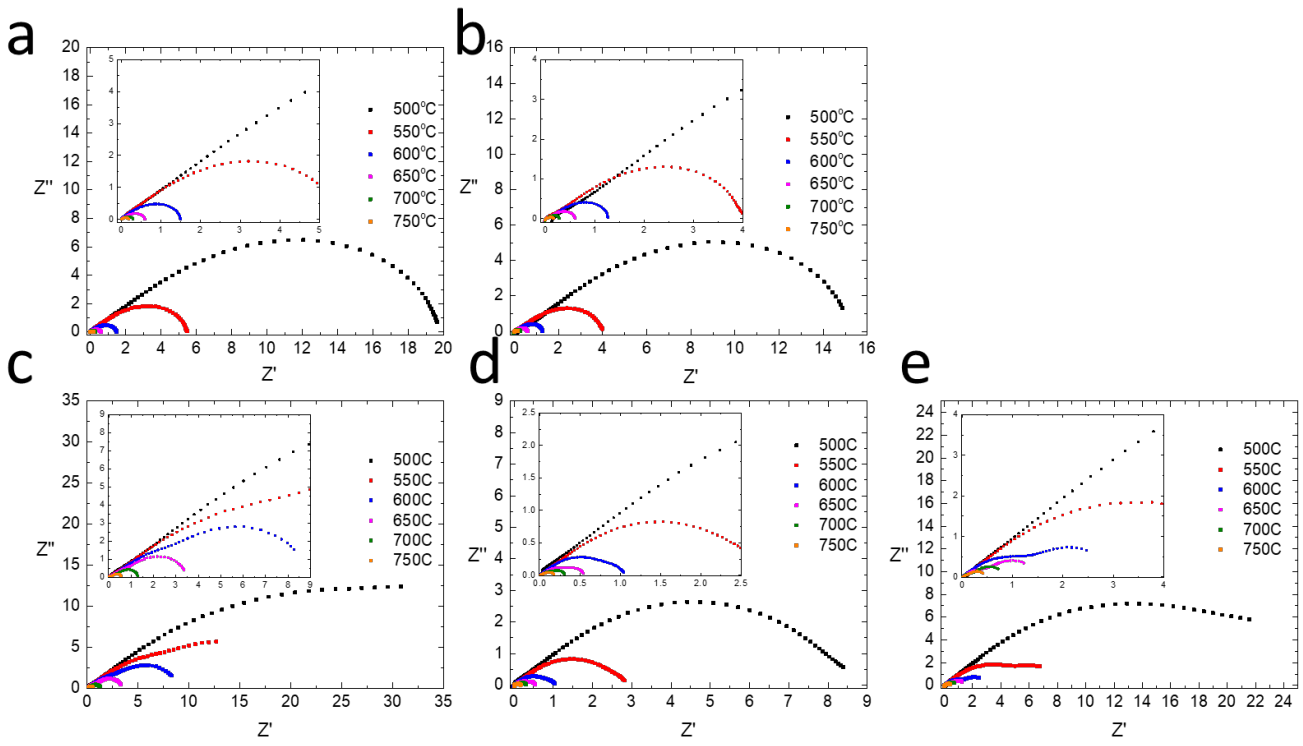

Figure 33. Nyquist plots generated by EIS with varying temperatures of (a) unmodified LSCF-GDC symmetric cell (b) 25 cycles of ZnO ALD (c) 9 cycles of TiO_2 (d) 16 cycles of TiO_2 (e) 25 cycles of TiO_2. Inserts show magnified view of higher temperature arcs.

Figure 34 shows the effect of changing pO_2 on the ALD modified symmetric cells. The pO_2 was varied at 600°C by changing the concentration of O_2 and N_2 using mass flow controllers.

The only symmetric cell which did not exhibit distinct impedance arcs is the unmodified sample. The ZnO symmetric cell has a small initial arc that does not change with pO_2 and a larger arc that decreases with pO_2. The TiO_2 symmetric cells have two arcs of similar size that follow the same trend.

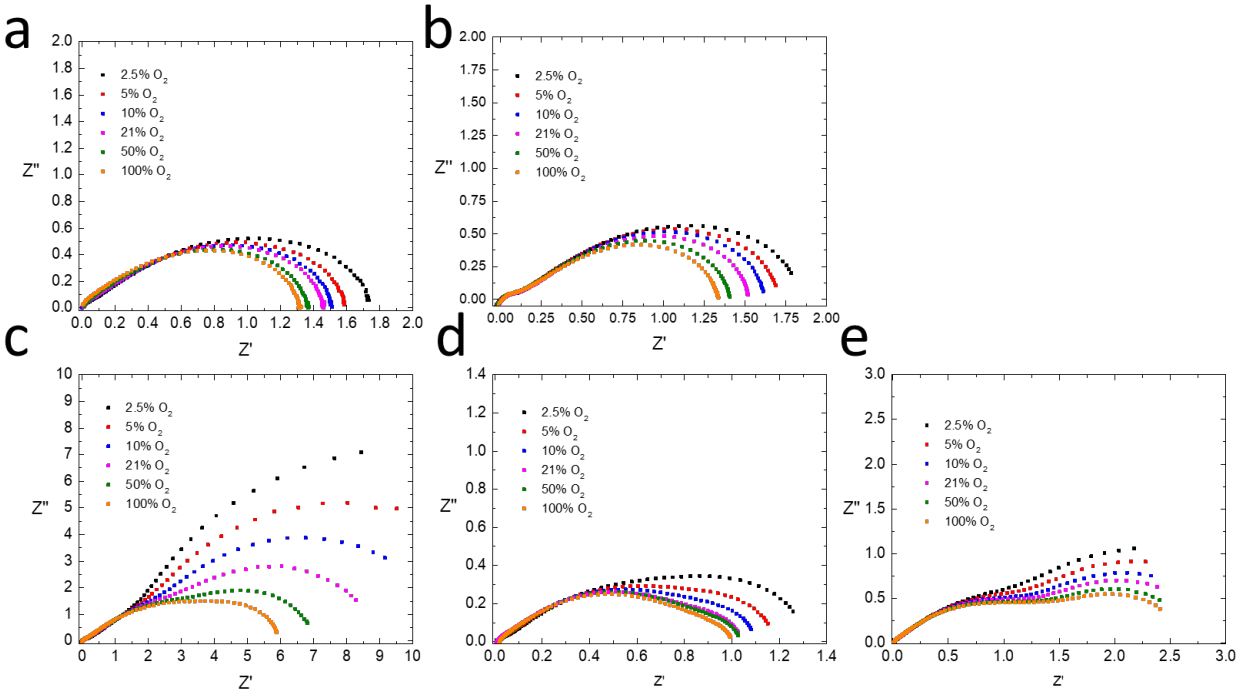

Figure 34. Nyquist plots generated by EIS with varying PO_2 of (a) unmodified LSCF-GDC symmetric cell (b) 25 cycles of ZnO ALD (c) 9 cycles of TiO_2 (d) 16 cycles of TiO_2 (e) 25 cycles of TiO_2. Inserts show a magnified view of higher temperature arcs.

The trends in symmetric cell performance are also summarized in **Figure 35** which presents cathode ASR as a function of temperature and pO_2. As expected, ASR decreased with increasing temperature and increasing pO_2. In **Figure 35 (a)** the samples with 25 cycles of ZnO and 16 cycles of TiO_2 showed lower ASR than the unmodified symmetric cell. However, this improvement was only present at lower temperatures. The other modified samples showed consistently higher ASR. In **Figure 35 (b)** the baseline cell had similar pO_2 dependence compared to the ALD modified samples except for the one with 9 cycles of TiO_2. **Table 1** shows the apparent activation energy (E_a) and pO_2 dependence derived from slopes in **Figure 35**. The best performing samples had the lowest E_a but otherwise no clear relationship can be observed as a function of ALD cycles for TiO_2. Additionally, all of the samples had similar pO_2 dependence except for the one with 9 cycles. It is unclear why the one with 9 cycles demonstrated much higher dependence on pO_2.

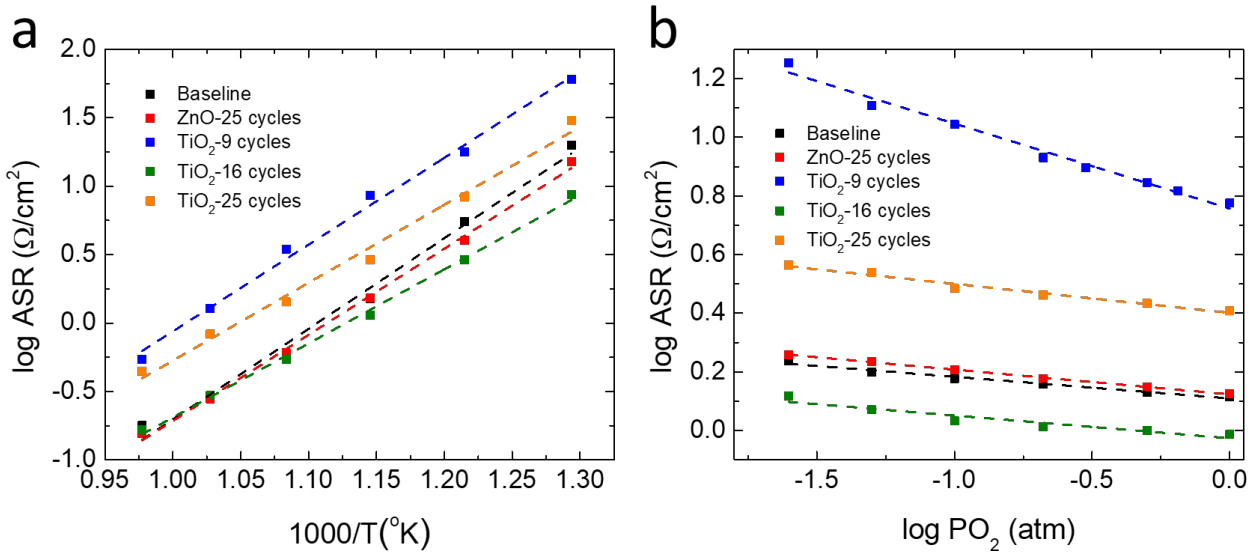

Figure 35. Total ASR as a function of (a) temperature and (b) pO_2.

Table 1. Activation energy and pO_2 dependence of tested symmetric cells.

Sample	Ea (eV)	pO_2 dependence
LSCF-GDC	1.32	-0.074
ZnO – 25	1.25	-0.085
TiO_2 – 9	1.26	-0.290
TiO_2 – 16	1.07	-0.078
TiO_2 – 25	1.13	-0.099

Effect of Thin Film Oxygen Content on Cathode Performance

Prior research on SOFC cathodes establishes that surface oxygen stoichiometry can significantly affect cation segregation as well as oxygen reaction kinetics. In order to study this effect in ALD films, EIS was done on LSCF-GDC symmetric cells using different ALD oxidizers and thermal annealing. By oxidizing ALD metal precursors using different oxidizers, the thin film can achieve different degrees of crystallinity.

For ALD, water and ozone are common oxidizers, and water is known to result in a more amorphous film that has a lower growth rate per cycle and retains protons. In contrast, ozone typically results in a more crystalline and stoichiometric film. The properties of an ALD film (or any metal oxide) can be tuned by post-deposition annealing in different atmospheres. This can affect the crystalline structure, chemical properties, and oxygen non-stoichiometry. By changing the oxygen content of the film, the surface of the underlying cathode may be adjusted as well.

The symmetric cells were coated with 16 cycles of TiO_2 ALD at 150°C using TDMAT as a precursor. The pulse time for TDMAT was 1 second and a 10 second purge time was added between each precursor and oxidizer pulse to ensure diffusion into the porous cathodes. To change the oxygen content, both water and ozone were tested as oxidizers. Water was tested for a longer duration as well since it is a weaker oxidizer. In addition, one of the water oxidized samples was also annealed in pure nitrogen. After ALD, the samples were coated with a gold current collector and then loaded into the reactor. The samples were heated in ambient air. The N_2 annealed sample was heated in a pure nitrogen environment up to 400°C, then left that way for one hour. Next, the environment was changed to synthetic air and temperature was raised to 500°C. EIS was measured repeatedly for one hour and no changes in the spectra were observed suggesting the film was stable at these conditions. At 600°C all symmetric cells were left for 3 hours to observe signs of cathode degradation or phase change of the film.

The effect of temperature on symmetric cell performance is shown in **Figure 36**. The TiO_2 coated cells exhibited similar impedance except for the one annealed in N_2. There is no clear difference in the choice of oxidizer or duration until 750°C when the ozone oxidized film becomes the best performing coating. The N_2 annealed sample shows the best performance up to 600°C, likely because it is gradually oxidizing making it more closely resemble the other films.

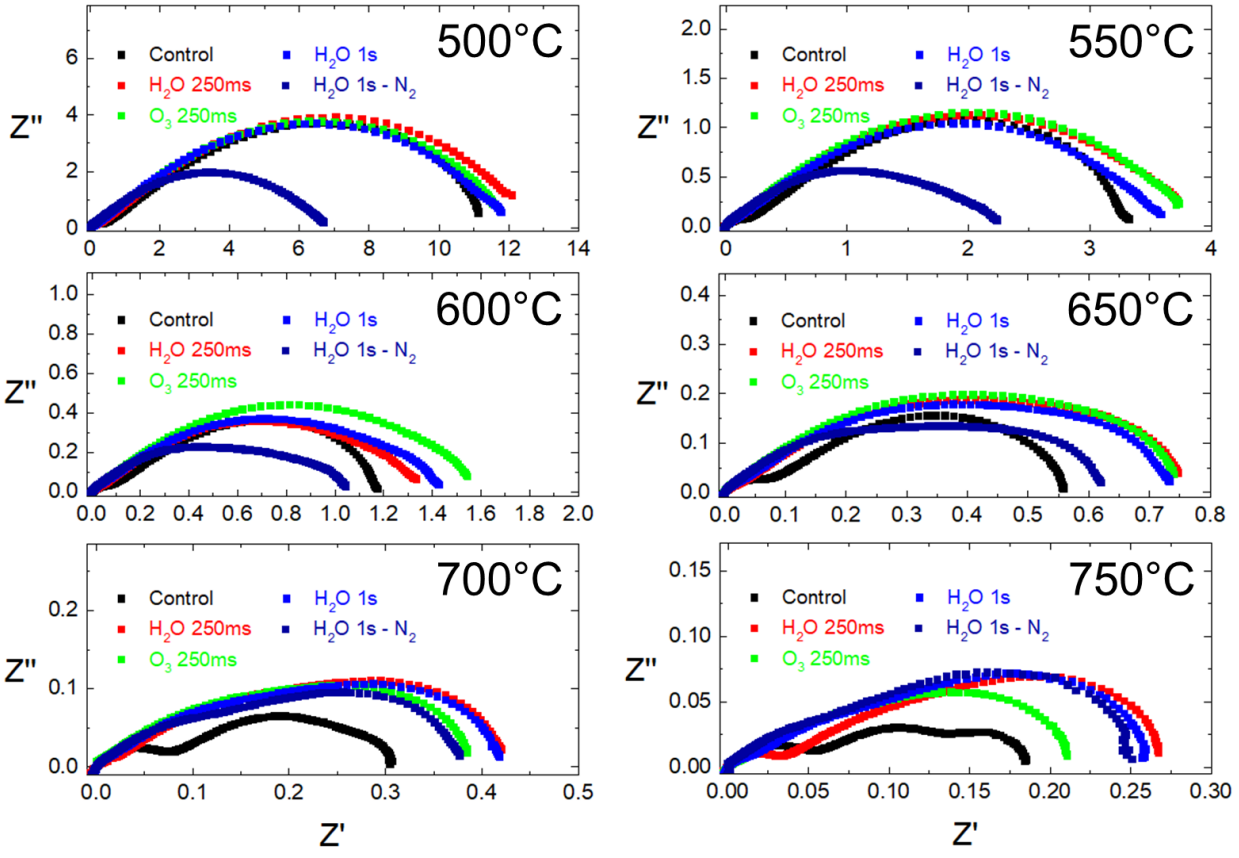

Figure 36. EIS spectra of TiO_2 coated symmetric cells. The initial measurement at 600°C is shown.

DRT Analysis of Modified Cathode EIS

In order to understand the mechanism(s) that affect cathode performance, distribution of relaxation time (DRT) was used to determine the contribution of different electrochemical processes to the cathode performance and the effects of each film, as shown in **Figure 37**. DRT analysis was done using the DRTTools plugin for matlab using 10^{-4} for the regularization parameter.

In the DRT spectra, both water-oxidized samples show similar performance suggesting that the increase in pulse time did not have a significant effect on the film properties. The N_2 annealed film exhibits entirely different performance from the other samples until about 700°C. All the symmetric cells had the primary process occur at a time constant of about 0.1 except for the annealed sample which had the dominant process occur at 0.01. The peaks at 0.1 and 1 grow with temperature for the annealed sample. Electrochemical processes occurring at intermediate frequencies/time constants ($0.01 \leq \tau \leq 1$) are attributed to the oxygen reduction reaction (ORR). Meanwhile the high frequency/low time constant processes are attributed to interfacial diffusion between the cathode and electrolyte. Thus it can be said that the improvement in performance with the N_2 annealed film is due to its enhancement of the ORR kinetics.

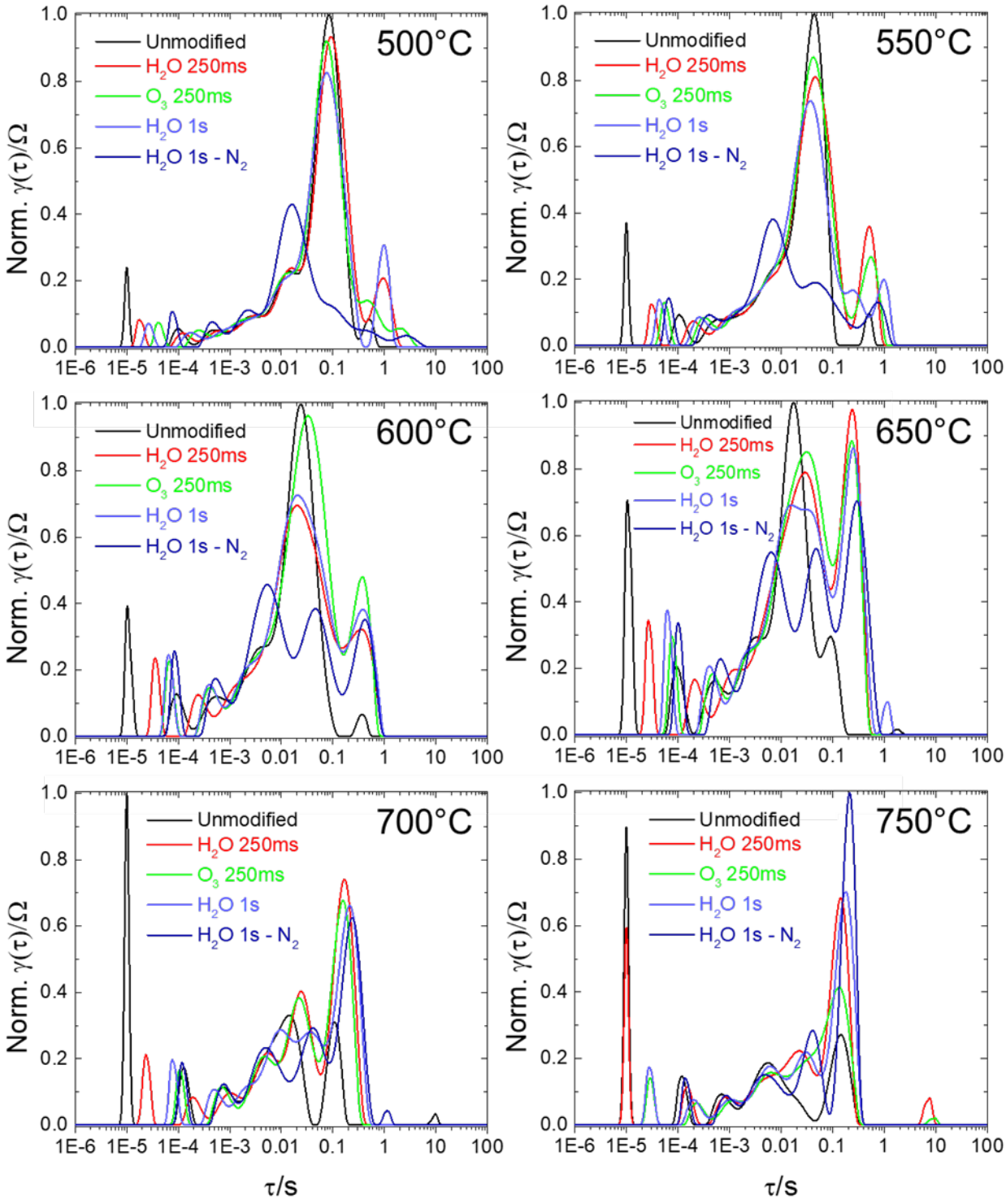

Figure 37. DRT analysis on ALD coated LSCF-GDC, derived from EIS spectra in Fig 6 at different temperatures.

The possible explanation of the ALD oxidizer effect is the concentration of oxygen vacancies in the film. It is also possible that the Ti atoms in the film reduced from Ti^{4+} to Ti^{3+}.

This is known to occur in oxygen deficient TiO_2 where Ti^{3+} ions may have higher mobility that can diffuse and dope into the LSCF bulk, modifying the surface stoichiometry of LSCF and change the cathode surface properties. Ti is more compatible in ionic radius with Co and Fe in the LSCF than La and Sr, thus it may occupy the B-site and affect the functionalities of LSCF.

We also considered the case that Ti diffusion into the GDC within the cathode. The fluorite structure of GDC has coordination numbers of 8 and 4 for cation and anion respectively. The ionic radii are Ce^{4+} = 0.97, Gd^{3+} = 1.053, and Ti^{4+} = 0.74 Å. Since the ionic radius increases with coordination and reduction, Ti^{3+} may substitute into the lattice. This could be beneficial at the interface between the LSCF and GDC. More work needs to be done to determine the exact mechanisms and the long-term stability of the cathode enhancement. Determining the pO_2 dependence and use of DRT would allow a better understanding of the mechanism. This ALD modification approach could streamline the use of ALD in surface modification.

Cathode Solution Infiltration

Baseline Cell Testing

Initial electrochemical testing was done on LSCF-GDC/GDC/LSCF-GDC to get baseline cell performance. **Figure 38 (a)** shows Nyquist plot of ohmic-corrected polarization impedance of LSCF-GDC symmetric cell at different temperatures. **Figure 38 (b)** shows the initial electrode polarization vs temperature for the LSCF-GDC/GDC/LSCF-GDC symmetrical cell. **Figure 39** shows a button cell performance for an anode supported Ni-GDC/GDC/LSCF-GDC cell. The peak power density is 0.45 W/cm^2 at 650 °C. The performance of surface modified cells will be compared to the baseline cell to quantitatively determine the improvement.

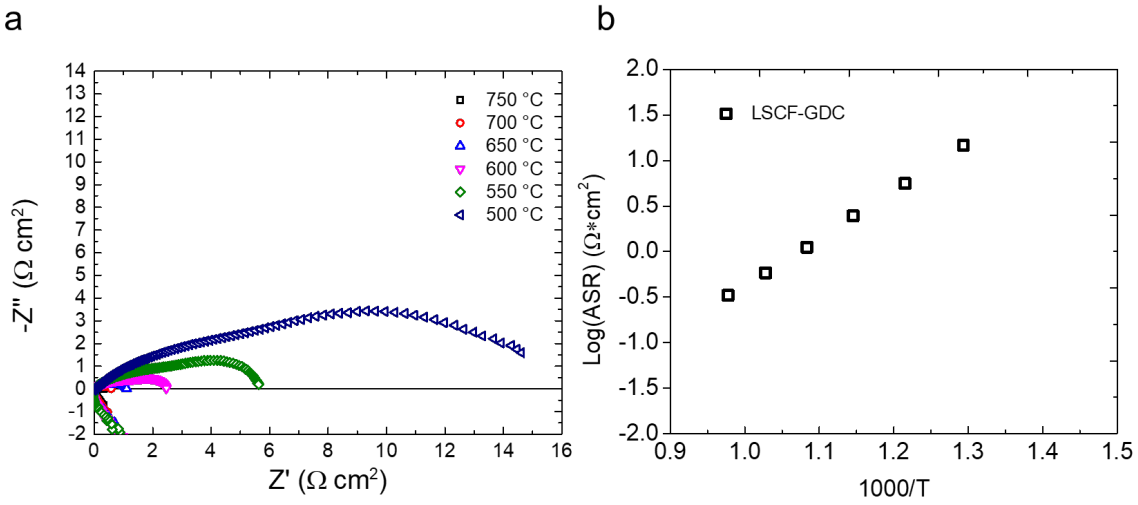

Figure 38. Electrochemical performance of LSCF-GDC/GDC/LSCF-GDC unmodified symmetric cell. (a) Nyquist plot of ohmic corrected polarization impedance of LSCF-GDC. (b) Arrhenius plot of polarization impedance of LSCF-GDC

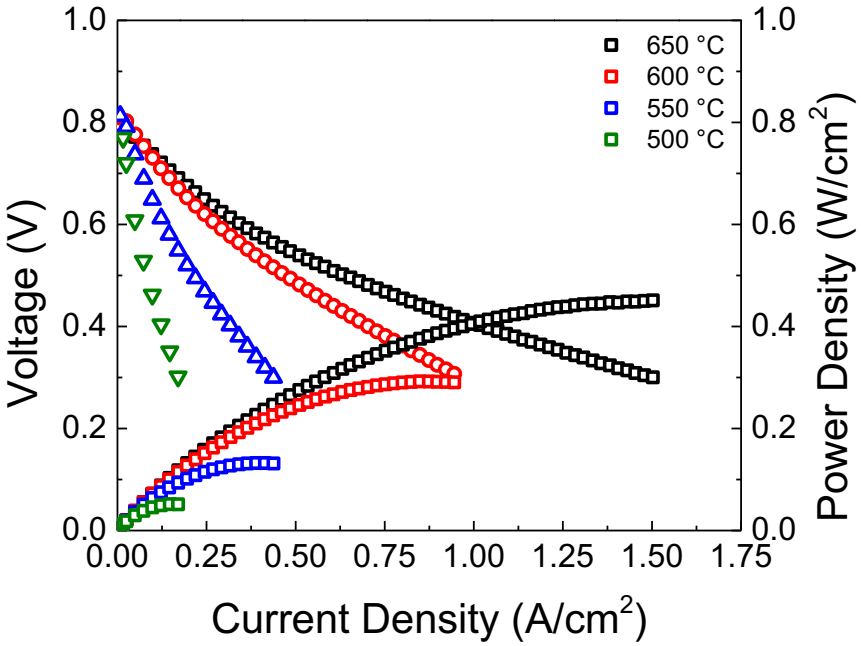

Figure 39. I-V characteristics of LSCF-GDC/GDC/Ni-GDC baseline SOFC performance plot at 500, 550, 600, and 650 °C.

Developing Solution Infiltration Technique

A solution infiltration technique was used to optimize the total nano-catalyst loading in the SOFC cathode. Solution infiltration on SOFC electrodes has been proven to not only improve the overall ASR of the SOFC electrodes but also the durability. The parameters to tune are how much loading per active area of electrode (i.e mass per area loading), the temperature of solution drying and calcination, and how many infiltration steps are required for optimal loading. Beginning with the first parameter to tune a micropipette was selected to apply the infiltration solution directly to the electrode. Using a cathode area of 0.31cm^2 three different amounts of solution were applied to LSCF-GDC/GDC/LSCF-GDC symmetrical cells. The amounts of infiltration solution were 10 µL, 5 µL and 2 µL. By a simple physical observation of the amount of solution on the surface of the cathode it was observed that 5 and 10 µL was too much solution for a 0.31 cm^2 electrode. So, a 2 µL drop size was selected to perform solution infiltration on a 0.31 cm^2 size electrode. **Figure 40** is a schematic of the solution infiltration process on an SOFC electrode. After selecting the drop size of the infiltrate, the resulting symmetrical cell was placed in a vacuum chamber for 10 minutes in order for the solution to wet the surface of the electrode and uptake into the pores of the electrode. After vacuum treatment the symmetrical cell then was placed into a furnace and heated to 450 °C to remove the solvent and calcine the nano-particles on the surface of the solution. This process is repeated for the second electrode on the backside of the symmetrical cell. After solution infiltration the symmetrical cell is ready for electrochemical testing.

Figure 41 are SEM images of the LSCF-GDC/GDC/LSCF-GDC cathode infiltrated with a praseodymium nitrate solution, comparing it to that of a non-infiltrated LSCF-GDC cathode. This was done to evaluate the bonding of praseodymium nitrate on the surface of the cathode. The image on the left does not have praseodymium infiltrated into the cathode. The image on the right shows the symmetrical cell infiltrated with praseodymium in the electrode which is the small particles on the surface of the cathode. The infiltrates are well-distributed into the porous LSCF-GDC scaffold and have very fine structure.

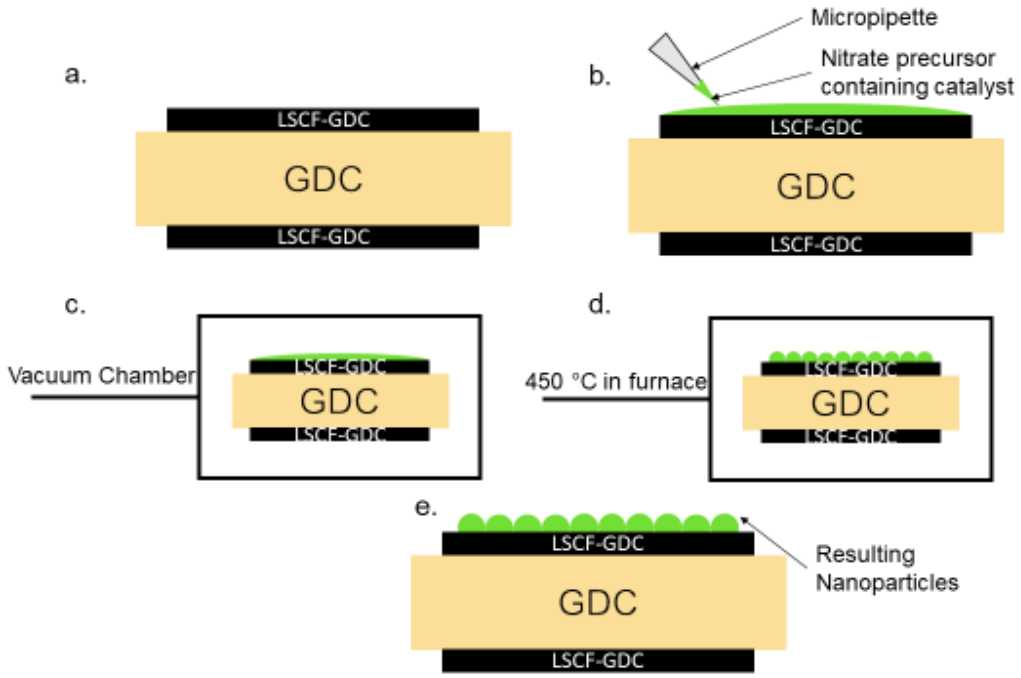

Figure 40. Solution infiltration process for SOFC electrodes. (a) Starting with a SOFC full or symmetrical cell. A LSCF-GDC/GDC/LSCF-GDC symmetrical cell is used here as an example. (b) Pipetting solution on desired electrode. (c) Vacuum treatment of solution on the surface of the symmetrical cell. (d) Calcination of nanoparticles and removal of liquid solution from electrode. (e) Final symmetrical cell after one electrode with resulting nanoparticles.

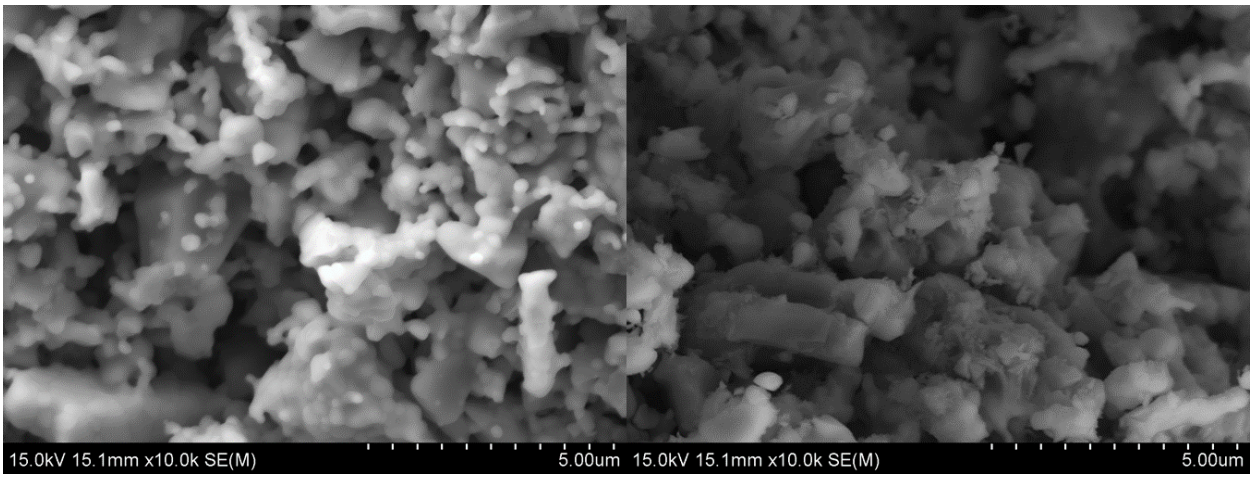

Figure 41 SEM images of LSCF-GDC without (left) and with praseodymium nitrate solution infiltration (right).

The infiltrates were first calcined at a relatively low temperature (450 °C) to decompose nitrates, and an *in situ* phase calcination of the nitrate solution was performed. By doing so, we can optimize the sintering temperature for the infiltrated electrocatalysts and avoid any coarsening from high temperature sintering. A symmetrical cell design was used to evaluate the electrochemical performance enhancement. **Figure 42** displays the initial EIS spectra for LSCF-GDC without praseodymium infiltration (a) and for LSCF-GDC infiltrated with praseodymium (b). There is an order of magnitude reduction in ASR for LSCF-GDC infiltrated with praseodymium oxide in all the tested temperatures, as summarized in the Arrhenius plot shown in **Figure 43**. Initial EIS testing of LSCF-GDC infiltrated with praseodymium show that the electrode polarization was lowered in desired SOFC cathode operating conditions (air at 500 -650°C).

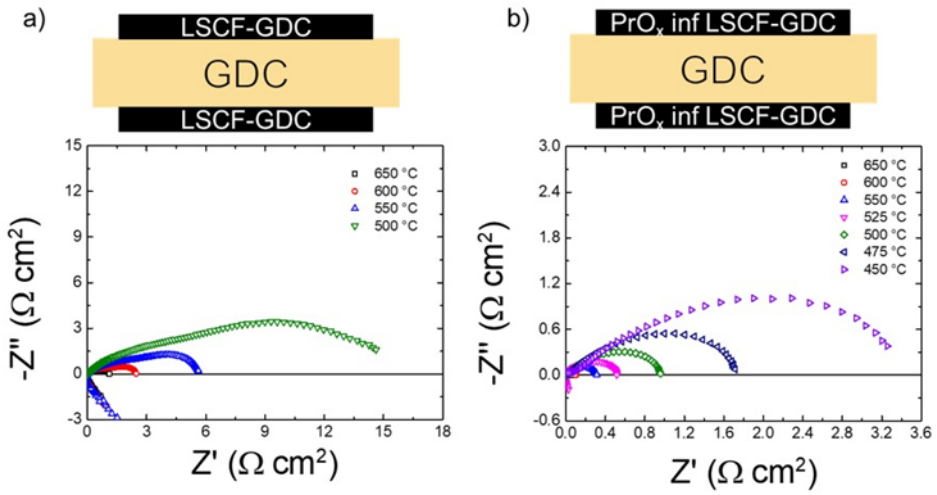

Figure 42. EIS of (a)LSCF-GDC and (b) LSCF-GDC infiltrated with PrO_x.

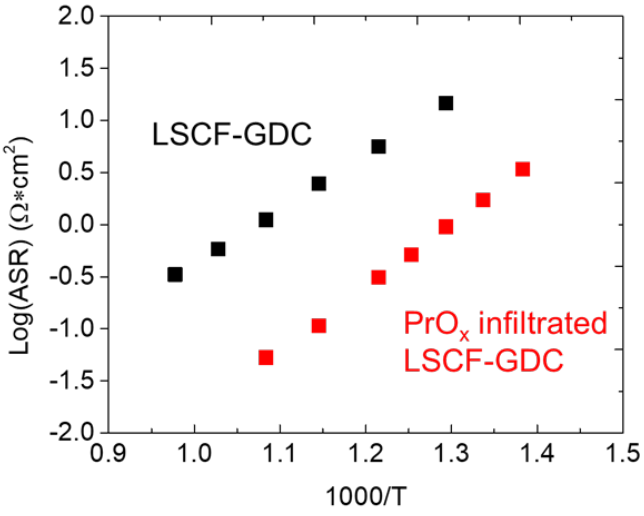

Figure 43. Arrhenius plot of Log(ASR) vs 1000/T for LSCF-GDC pristine cell (black) and PrO_x infiltrated LSCF-GDC cell (red).

To identify the optimal number of $PrNO_3$ infiltrations on the LSCF-GDC cathode, symmetrical cells were fabricated and infiltrated 0 (unmodified), 1, 3, and 5 times by the previously explained method. EIS was carried out at four temperatures (650, 600, 550, and 500 °C) to determine the non-ohmic area-specific resistance (ASR) of both the unmodified and modified cathodes. **Figure 44** shows a summary of the impedance for all cells at each temperature. All three infiltrated cathodes showed significantly lower ASR than the unmodified LSCF-GDC cathode (by approximately an order of magnitude). The cathode infiltrated 3 times was found to have the lowest ASR of all the tested symmetrical cells with values of 0.037, 0.073, 0.192, and 0.615 Ω cm^2 at 650, 600, 550, and 500 °C, respectively.

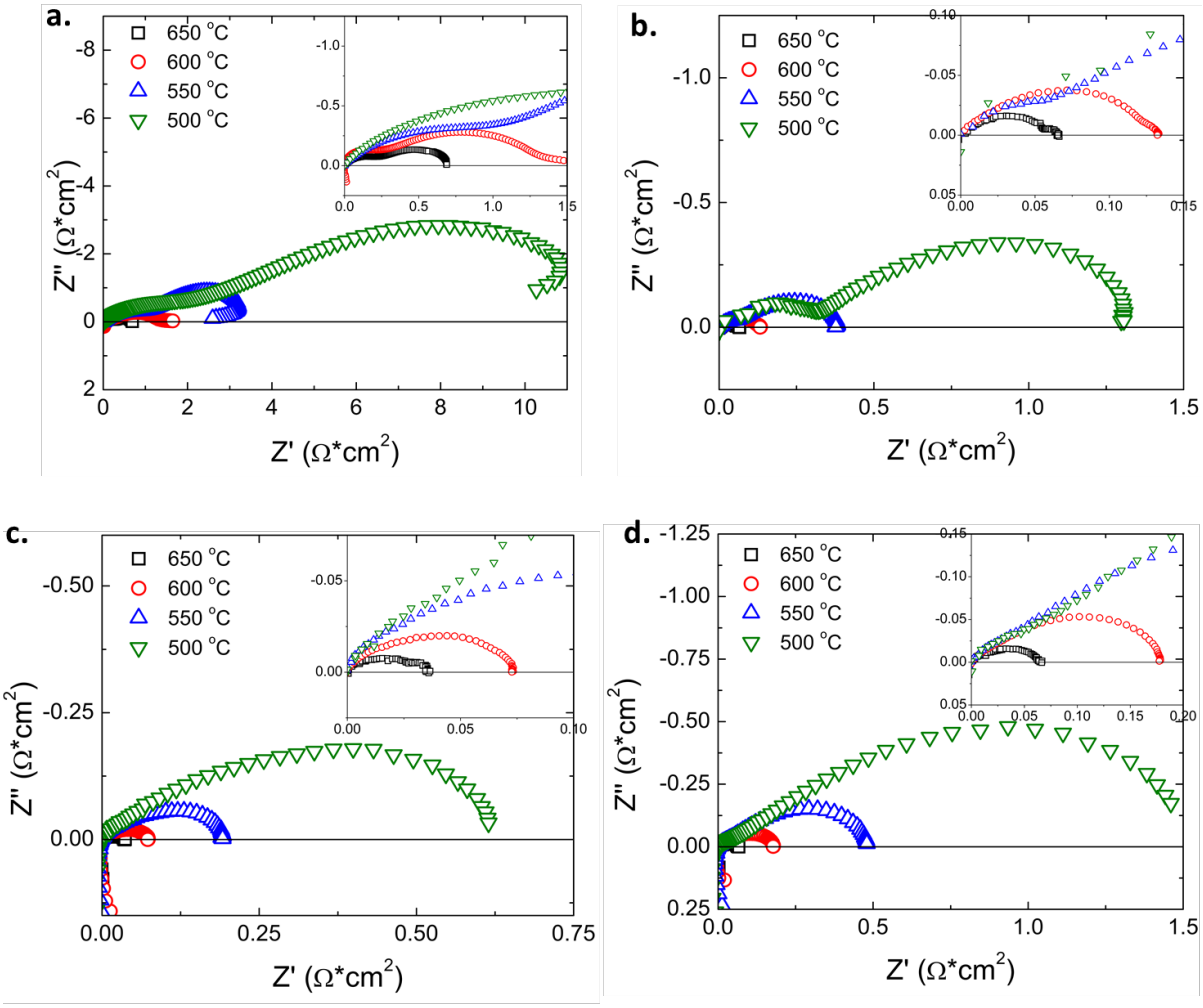

Figure 44. Temperature dependent impedance plots for symmetrical cells with composition of LSCF-GDC|GDC|LSCF-GDC with (a) no modification, (b) 1 infiltration of $PrNO_3$, (c) 3 infiltrations of $PrNO_3$, and (d) 5 infiltrations of $PrNO_3$.

Figure 45. (a) is provided for a direct comparison of each cell with different infiltration cycle at 600 ºC. The non-ohmic ASR was recorded and plotted logarithmically with the inverse temperature in **Figure 45. (b)**.

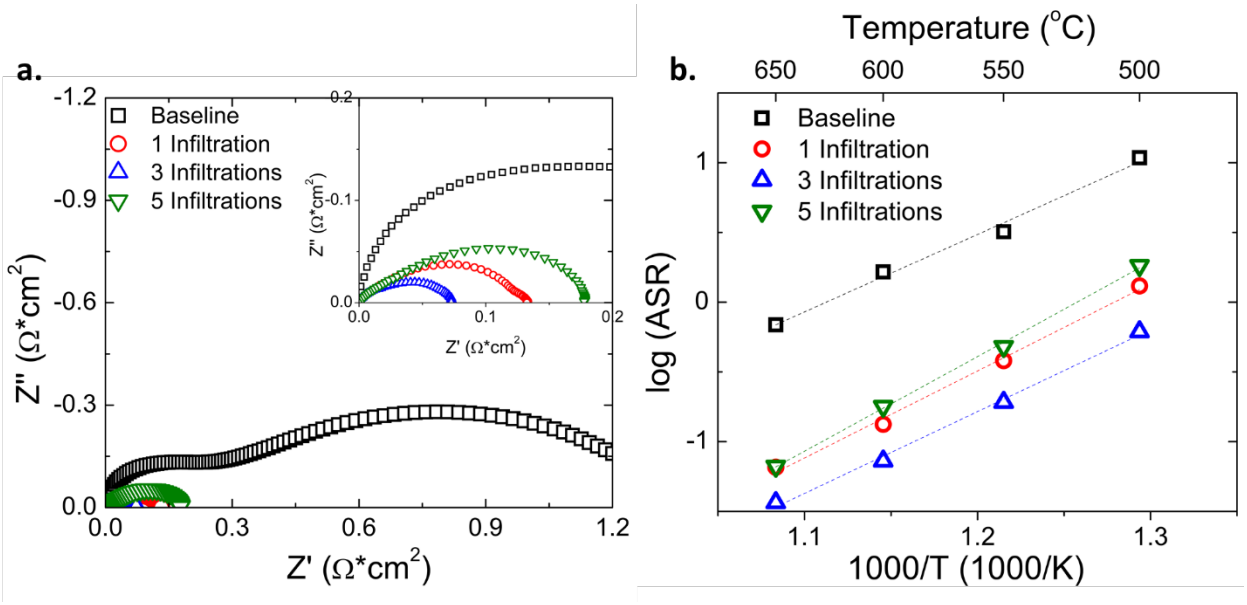

Figure 45. (a) Impedance plots for LSCF-GDC|GDC|LSCF-GDC symmetrical cells with various infiltration cycles at 600 ºC, and (b) Arrhenius plot of non-ohmic resistance for each infiltration cycle.

The non-ohmic ASR was plotted as a function of the number of infiltration cycles for each temperature in **Figure 46 (a)**, and the minimum is observed at 3 infiltrations. Furthermore, in **Figure 46 (b)** the non-ohmic ASR of each modified cell is standardized by the non-ohmic ASR of the unmodified cell at the corresponding temperature (ASR_o). For 3 infiltration cycles, the ASR was reduced by over 92.5% at all temperatures. The increase in non-ohmic ASR from 3 to 5 infiltrations could be a result of a pore/surface blocking effect. While the addition of nano-particles on the surface can catalyze the oxygen reduction reaction, excess particles can crowd pores and hinder oxygen transport. This theory will be further investigated by visual observation (with a scanning electron microscope) of the microstructure of each symmetrical cell.

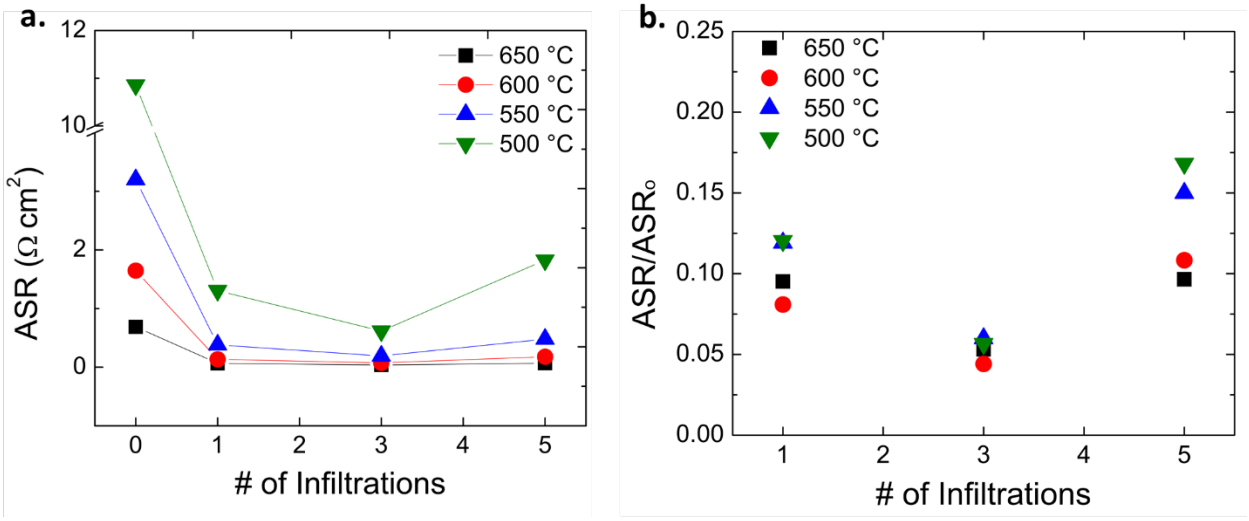

Figure 46. Non-ohmic (a) absolute ASR and (b) standardized ASR response to various number of cathode infiltration cycles.

Developing Solution Infiltration Technique on SSC

We further investigated the electrochemical behavior of various metal oxide infiltrates on the surface of a common SOFC cathode, SSC-GDC composite. SSC is selected because it exhibits excellent electronic conductivity and oxygen reduction capabilities at lower temperatures and has limited CO_2 interaction. These two characteristics make SSC an ideal candidate for a low-temperature SOFC cathode.

SSC-GDC cathode paste was prepared using commercially available $Sr_{0.5}Sm_{0.5}CoO_{3-\delta}$ (Praxair Surface Technologies) and $Gd_{0.1}Ce_{0.9}O_{2-\delta}$ (Fuel Cell Materials), respectively. The powders were then matched by a 50:50 surface area mixture and ball-milled in ethanol to ensure a homogenous mixture. The ink vehicle, ESL 441, was then added slowly in steps while ethanol was evaporated from the solution. After the ethanol was evaporated the remaining ink was then applied to GDC pellets and fired to form SSC-GDC/GDC/SSC-GDC symmetrical cells. Each cathode was then infiltrated with a total of 6 µL of 1 M solution and heated to 450 °C to dry the nitrates. The final calcination occurs *in situ* to reduce the number of necessary heating cycles that the cell undergoes. This process was optimized and shown in the previous report. Each symmetrical cell underwent EIS measurements under a temperature sweep and was aged to observe the stability of the nanoparticles.

Electrochemical Performance of Various Infiltrated Cathodes

Figure 47 shows the transition metal oxides screened as infiltrate materials on SSC-GDC. Baseline performance shows that the impedance of unmodified SSC-GDC composite cathode has matched values in literature, as shown in **Figure 47 (a)**. EIS results of Fe, Cu, Ni, and Co infiltrated cells at different temperatures are shown in **Figure 47 (b)-(e)**. None of the transition elements screened show appreciable effect to the performance enhancement. Cu modified cell has the largest

ASR, an ASR of 5.6 $\Omega \cdot cm^2$, compared to the reference cell 2 $\Omega \cdot cm^2$ at 500 °C. The infiltration of Fe, Ni, and Co all increase the value of the cathode ASR. Generally, the B site element in the ABO_3 perovskite is considered to be related to the catalytic activity. Our results show that Fe, Cu, Ni, and Co, on the cathode surface decrease the performance, indicating that the additional B-site cations on the perovskite cathode do not further promote the oxygen exchange properties.

Figure 48 shows the EIS results of Pr, Dy, Nd, and Ag infiltrated cells. Among all infiltrates, Nd and Ag seem to have a negative effect on the cathode area specific resistance (ASR). Dy modified cell shows a slight improvement in the ASR, showing an ASR of 0.19 $\Omega \cdot cm^2$, compared to the reference cell 0.2 $\Omega \cdot cm^2$ at 500 °C. In contrast, Pr modified cell shows significant enhancement in electrochemical performance.

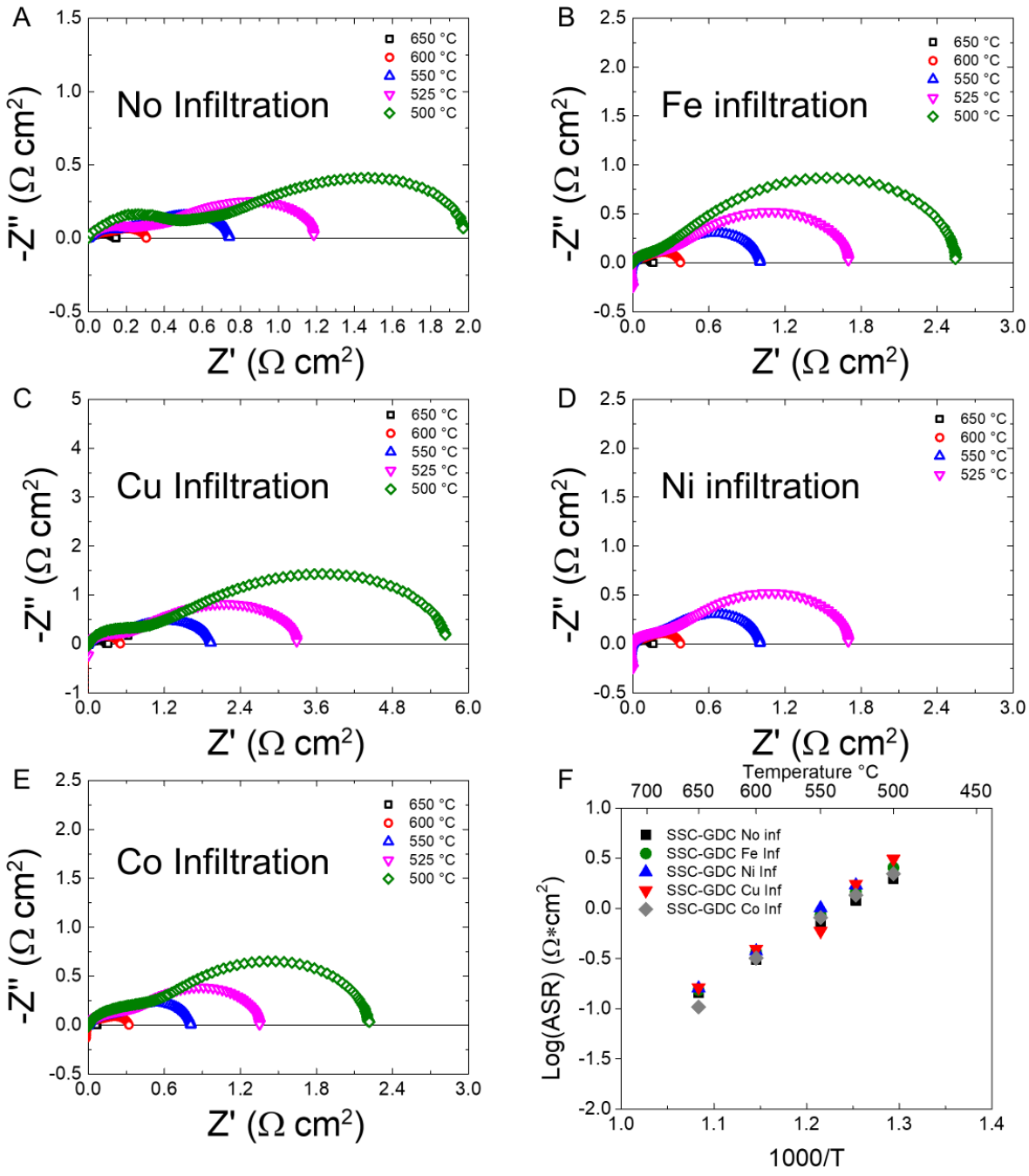

Figure 47. Electrochemical performance of transition metal infiltrated SSC-GDC cells. Nyquist Plot of (a) unmodified SSC-GDC symmetrical cell, (b) Fe, (c) Cu, (d) Ni, and (e) Co infiltration on SSC-GDC. (f) Arrhenius plot of cathode infiltrates with respect to the reference, SSC-GDC.

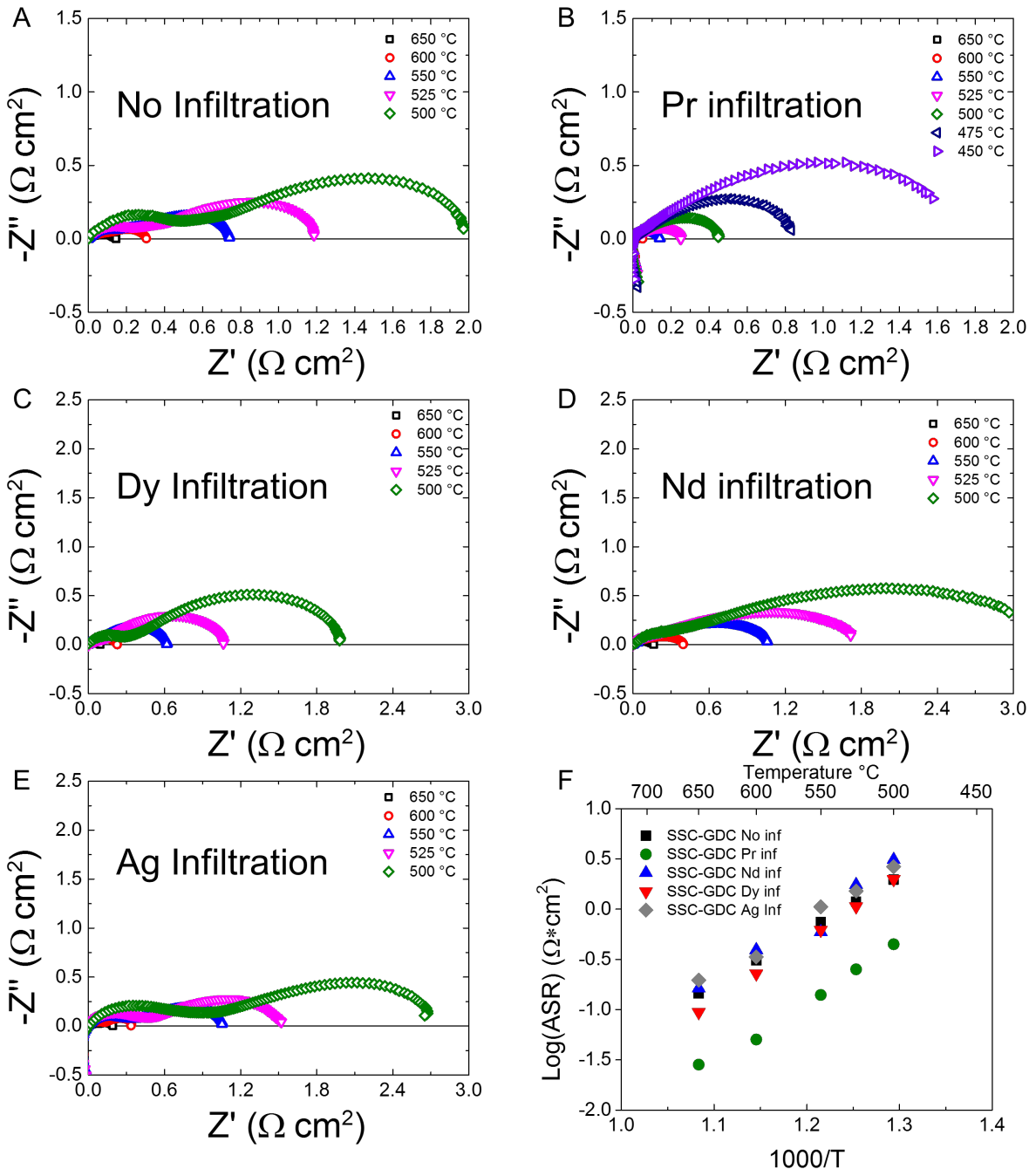

Figure 48. Electrochemical performance of infiltrated SSC-GDC cells. Nyquist Plot of (a) unmodified SSC-GDC symmetrical cell, (b) Pr, (c) Dy, (d) Nd, and (e) Ag infiltration on SSC-GDC. (f) Arrhenius plot of cathode infiltrates with respect to the reference, SSC-GDC.

Arrhenius plot of the cathode ASR is summarized in **Figure 48** (f). Pr modified cell shows an order of magnitude lower ASR than all other cells in the tested temperature range. Praseodymium oxide infiltration had the most significant effect to ASR out of the entire set of

infiltrating materials screened. At the targeted lower SOFC cathode operation temperatures, SSC-GDC has ASR values of 0.30 and 1.97 Ωcm^2 at 600 °C and 500 °C respectively. With a PrO_x infiltration onto SSC-GDC the ASR is reduced to only 0.05 and 0.45 $\Omega \cdot cm^2$ at 600 °C and 500 °C respectively. This could be due to the multivalent nature of Pr that effectively participates the oxygen reduction reaction. A further study is needed to determine the role of Pr on the surface exchange.

The Microstructure of Infiltrated SSC-GDC

The microstructure of the Pr infiltrated SSC-GDC with different infiltration cycles is shown in **Figure 49**. Compared to the EIS results from the previous report, it clearly shows that the loading of the infiltrated nano-electrocatalyst has a direct impact on the performance. Using Pr infiltration on SSC-GDC as an example in **Figure 49**, the optimized microstructure is the one with 3 infiltration cycles. The low loading has insufficient catalytic activity (as shown in 1 infiltration cycles). In contrast, the high loading will block active sites (triple phase boundaries), limiting the performance (as shown in 7 infiltration cycles).

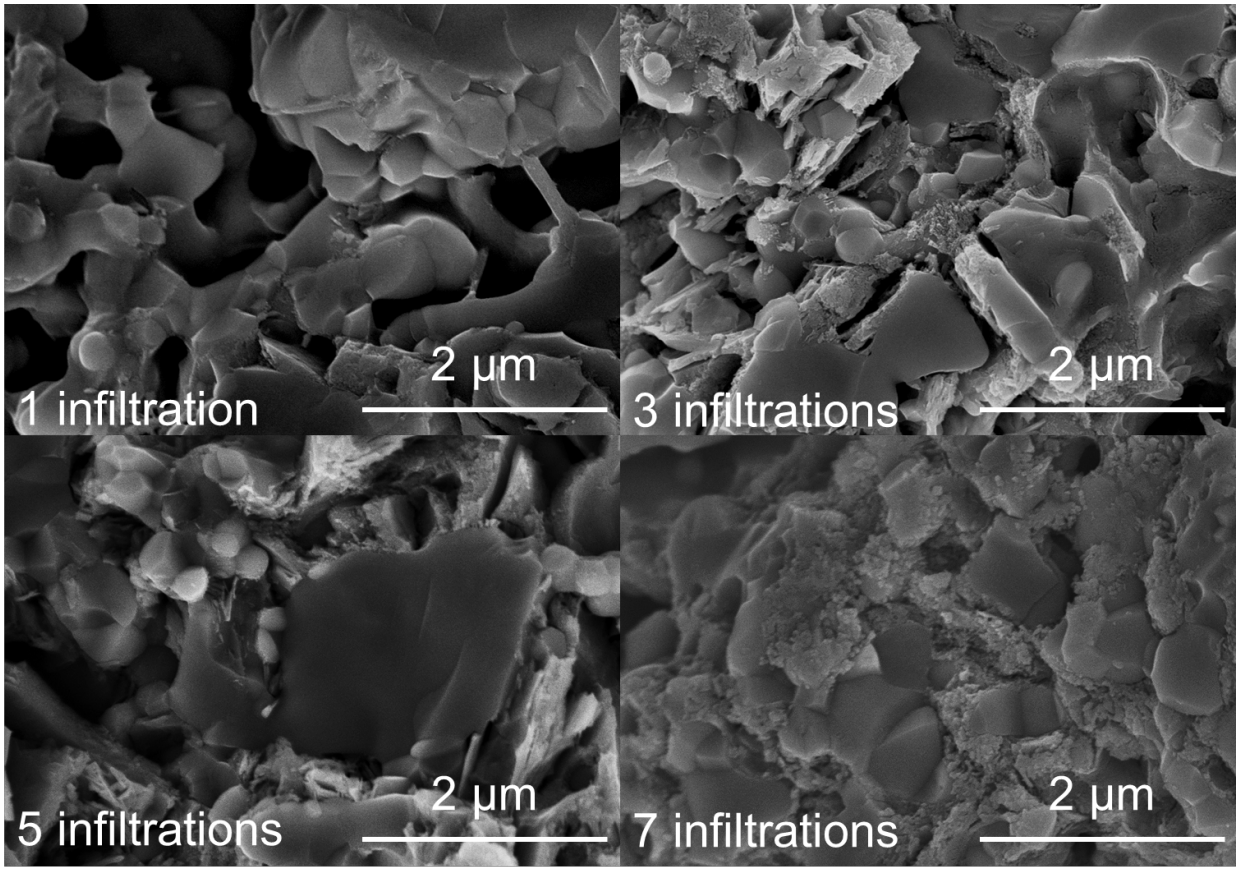

Figure 49. Microstructure of Pr modified SSC-GDC with different infiltration cycles.

Long-term stability of the modified cathodes

The long-term stability of surface modified SSC-GDC

The cathode ASR of modified cells as a function of aging time for 400 hours is shown in **Figure 50.** At the first 100 hours, all modified cells show a slight increase of the cathode ASR, possibly due to particle agglomeration. Nevertheless, all modified cells show a plateau of ASR after 100 hours of aging.

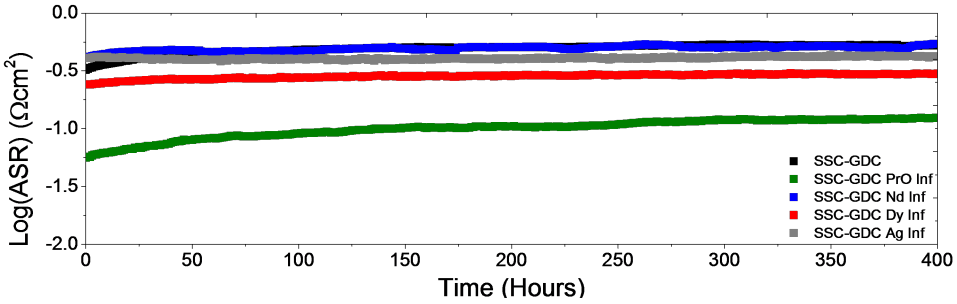

Figure 50. The long-term stability of surface modified cells. Cathode ASR of surface modified SSC-GDC symmetrical cells as a function of aging time.

Evaluation of the stability of the modified cathodes in CO_2

It is important to evaluate the CO_2 effect on the performance of the newly developed surface modified cathodes as CO_2 poisoning is a well-known issue for the durability of current SOFC cathodes. Reference SSC-GDC and surface modified PrO_x infiltrated SSC-GDC symmetrical cells were tested for their cathode ASR dependence on pCO_2 and temperature. As seen from the Nyquist plots of unmodified and modified cell in **Figure 51** (**a-b**), respectively. With the presence of CO_2 (1% CO_2), unmodified SSC-GDC has a substantial increase in cathode ASR compared to that of the modified one. The ASR is about 3 times lower when comparing the surface modified and reference cathodes, respectively. The same trend is also observed in a higher concentration of CO_2 (10% CO_2) in **Figure 51** (**c-d**). The temperature dependence on ASR is summarized in Arrhenius plot in **Figure 51** (**e**), showing that CO_2 effects are observed across all the tested temperatures, and there is a trend of the decrease in activation energy with increasing CO_2 concentration.

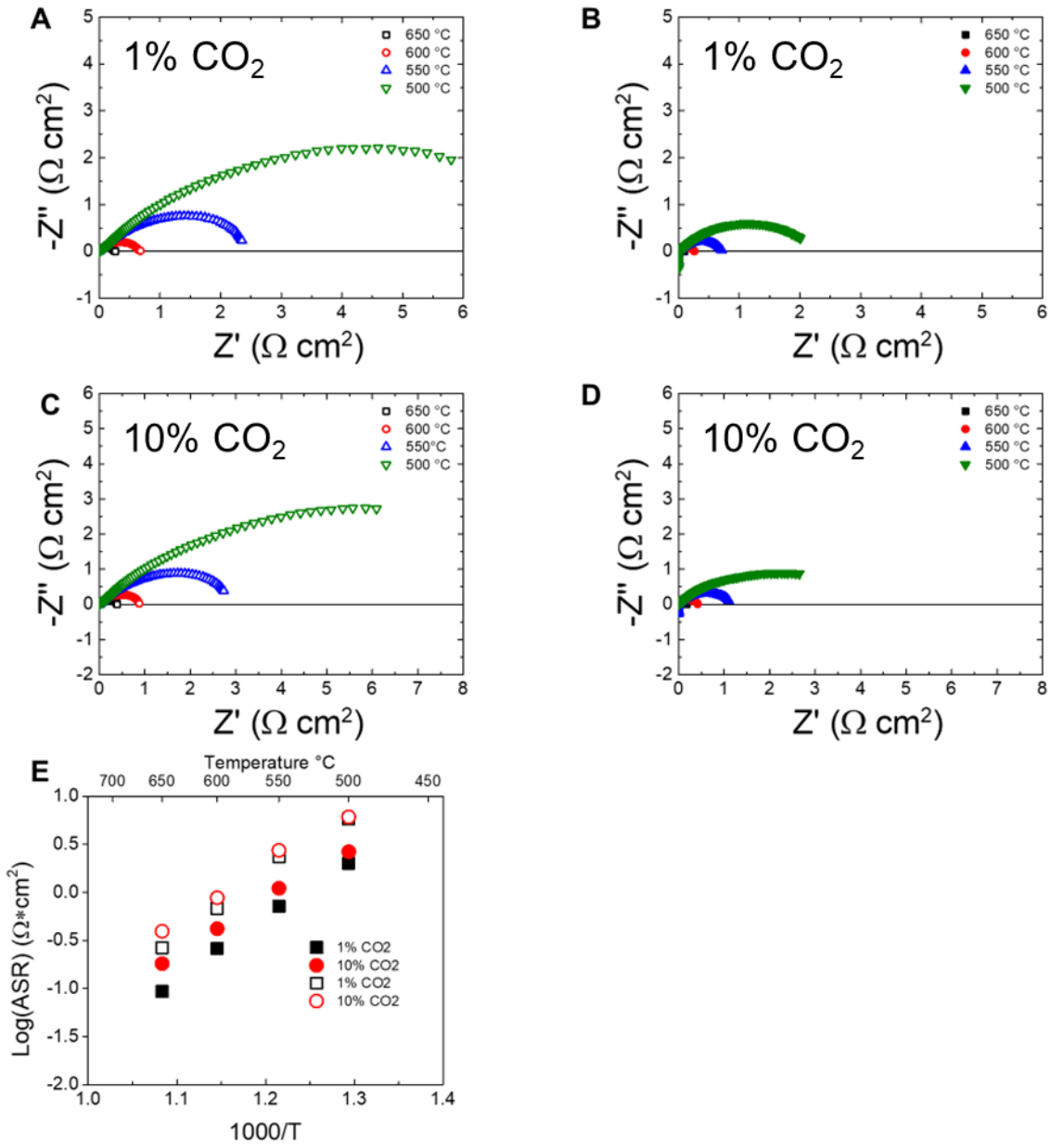

Figure 51. pCO_2 Dependence of SSC-GDC and PrOx infiltrated SSC-GDC. (a) Temperature dependent EIS, SSC-GDC symmetrical cell tested in 1% CO_2. (b) PrO_x infiltrated SSC-GDC symmetrical cell tested in 1% CO_2. (c) SSC-GDC symmetrical cell tested in 10% CO_2. (d) PrO_x infiltrated SSC-GDC tested in 10% CO_2. (e) Extracted Arrhenius plot for temperature dependent CO_2 testing. SSC-GDC (Open Symbol), PrO_x infiltrated (Closed Symbol).

Shown in **Figure 52 (a-b)** are the temperature dependent Nyquist plots for 10% pO_2 of both SSC-GDC and PrO_x infiltrated SSC-GDC respectively. Nyquist plots in a higher pO_2 (50%) for SSC-GDC and PrO_x infiltrated SSC-GDC are shown in **Figure 52 (c-d)**, respectively. Compared to the regular SSC-GDC. PrO_x infiltrated SSC-GDC has lower ASRs in all temperatures. The Arrhenius relationship in **Figure 52 (e)** elucidates the relationship between pO_2

dependence and cathode ASR. The infiltrated sample has much faster ORR kinetics which would lead to a significant reduction in ASR.

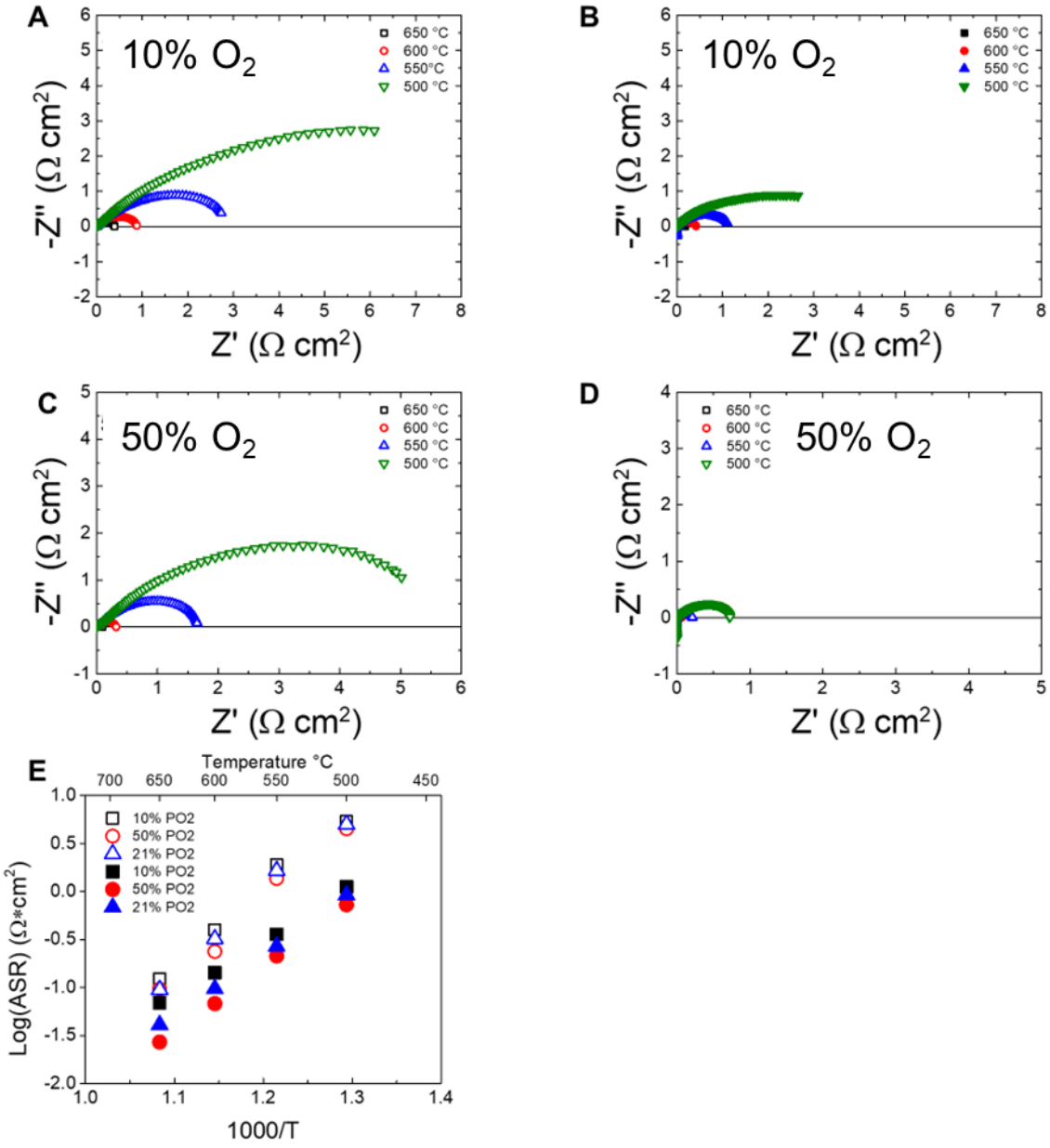

Figure 52. pO_2 Dependence of SSC-GDC and PrO_x infiltrated SSC-GDC. (a) Temperature dependent EIS, SSC-GDC symmetrical cell tested in 10% pO_2. (b) PrO_x infiltrated SSC-GDC symmetrical cell tested in 10% O_2. (c) SSC-GDC symmetrical cell tested in 50% O_2. (d) PrO_x infiltrated SSC-GDC tested in 50% pO_2. Extracted Arrhenius plot for temperature dependent pO_2 testing. SSC-GDC (Open Symbol), PrO_x infiltrated (Closed Symbol).

Long-term stability of modified cathodes

Figure 53 shows the temperature dependent behavior of the SSC-GDC and PrO_x infiltrated SSC-GDC symmetrical cells aging for over 2000 hours at 600 °C in air. **Figure 53** (**a-b**) shows SEM images of the unmodified and modified cell after 2000 hours of aging, respectively. There is no significant agglomeration of PrO_x after thousands of operating hours, indicating that the calcination at 650 °C does not affect the long-term stability for cells operating at 600 °C.

Figure 53 (**c**) shows the changes in electrode ASR as a function of aging time. The unmodified cell is shown in black, and SSC-GDC shows a rapid increase in ASR in the first 250 hours. The modified cell is shown in red, and the aging curve shows a very stable ASR. The PrO_x infiltrated sample shows an increase in stability and performance over the SSC-GDC cathode. The aging Nyquist plots in **Figure 53** (**d-e**) show that the majority of degradation occurs for SSC-GDC in the first 250 hours rather than that for the infiltrated sample. The infiltrated sample shows that the first arc growth is halted in the PrO_x infiltrated sample compared to the of the SSC-GDC cathode. The SSC-GDC shows that both arcs grow with time contributing to rapid degradation over the first 250 hours compared to that of the infiltrated sample.

The ASR value after 2000 hours for the infiltrated sample is 0.2 Ωcm^2 compared to that of 0.6 Ωcm^2 for that of the SSC-GDC cathode. As the first arc is attributed to high frequency it may be due to the infiltration process stabilizes charge transfer process within the material, potentially preventing phase destabilization. The low frequency arc which does grow may be due to slight coarsening of the infiltrate. Our results show that the overall performance and stability of the modified cell is significantly better.

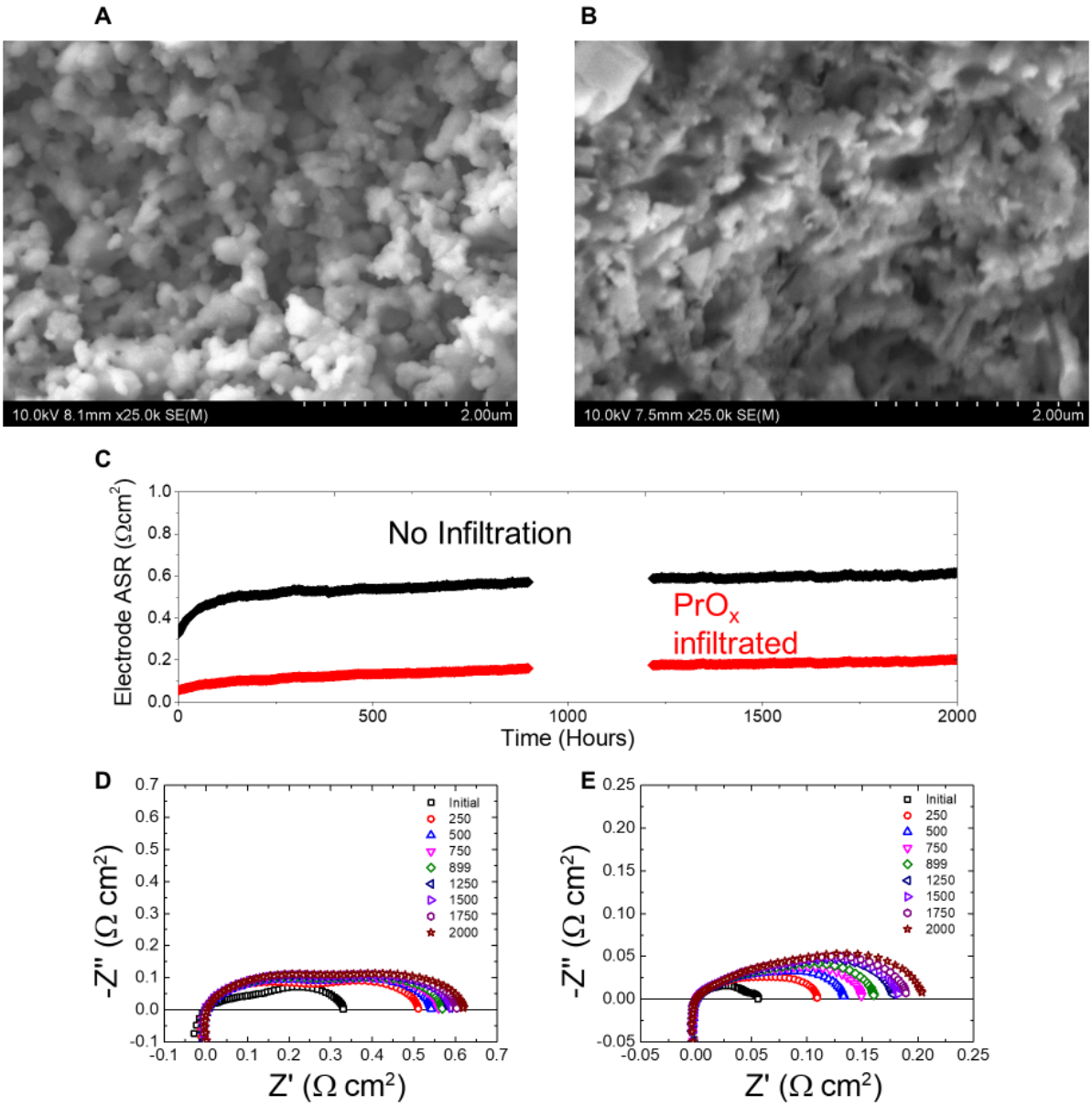

Figure 53. Long term stability of the modified cathode. SSC-GDC symmetrical cells with or without surface modification (PrO_x) were aged at 600 °C in air for over 2000 hours. (a) SEM image of unmodified SSC-GDC aged 2k hours. (b) SEM image of PrO_x infiltrated SSC-GDC aged for 2k hours. (c) Cathode ASR vs time for SSC-GDC and PrO_x infiltrated SSC-GDC. (d) and (e) Aging Nyquist plots of SSC-GDC and PrO_x infiltrated SSC-GDC respectively.

Ceramic Anode Development

SFNM Material Synthesis and Phase Identification

Ceramic anodes with the composition $SrNi_{0.5}Mo_{0.5}O_{3-\delta}$ (SNM) were synthesized by the solid-state method. The process consisted of mixing stoichiometric amounts of $SrCO_3$ (Aldrich), NiO (Fuel Cell Materials), and MoO_3 (Alfa-Aesar) and milling in ethanol for 24 hours. Next, the slurry was dried overnight and the homogeneous mixture was collected into an alumina crucible, and then calcined at 1100°C for 4 hours.

After only one calcination (at 1100°C for 4 hours), significant impurity peaks were identified by the XRD. NiO precursor was still detected along with the side-products $SrMoO_4$ (PDF #96-153-3565) and $Sr_{11}Mo_4O_{23}$ (PDF #96-230-0577). In order to increase the purity of the desired product, the SNM powder was re-calcined until the impurity peaks nearly vanished. **Figure 54 (a)** shows the XRD results after each calcination step. It is clear that the peaks around 27.5° and 30.75° shrunk significantly after repeating calcination. For clarity, **Figure 54 (b)** is included to focus on these peaks. $SrNi_{0.5}Mo_{0.5}O_{3-\delta}$ has been successfully synthesized with minimal impurities present.

Next, a variation of SNM was synthesized, $SrFe_{0.1}Ni_{0.45}Mo_{0.45}O_{3-\delta}$ (SFNM144), with Fe on the B-site to increase the electrical conductivity of the anode material. The XRD results for SFNM144 are presented in **Figure 55**. SFNM144 was synthesized in the same manner as SNM, but did not require three re-calcination steps, only one.

Conductivity of Ceramic Anodes

The conductivity of the anode material is extremely important for an anode-supported fuel cell. If the anode layer (on the order of hundreds of microns) is not sufficiently conductive, major ohmic losses will be observed in the cell.

To test conductivity, dense samples of both SNM and SFNM144 were fabricated by uniaxially pressing powder into pellets and sintering at 1340°C for 4 hours. The pellets were cut into bars for conductivity testing. Four-probe measurements were taken using a Keithley 2400 SourceMeter over the range of 450-650°C in air and pure H_2 environments. The conductivity results are presented in **Figure 56**. Clearly, the addition of Fe to the B-site of the perovskite results in a significant increase in bulk conductivity in reducing environments.

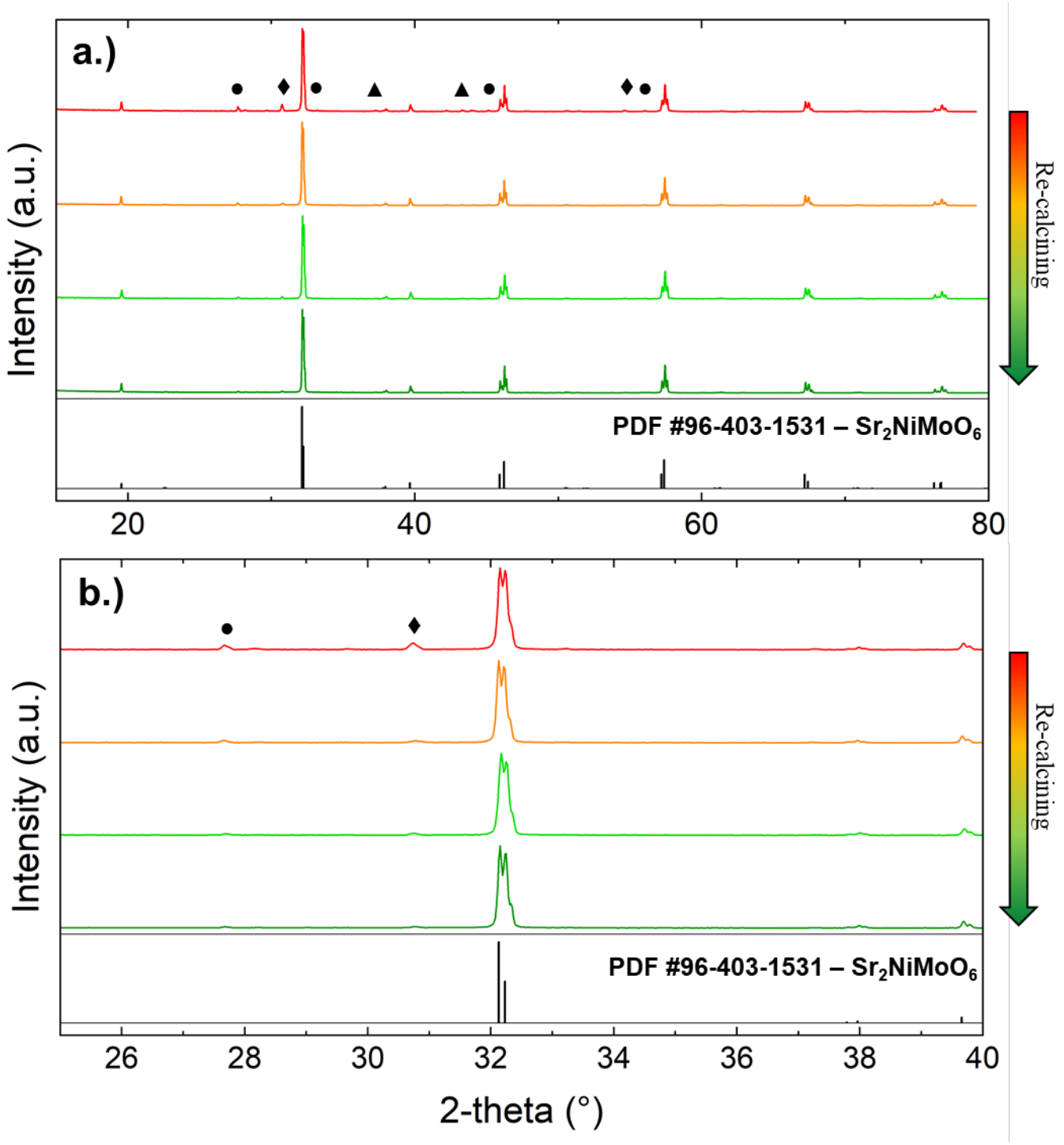

Figure 54. (a) XRD patterns for SNM after each of the 4 calcination steps. (b) Zoomed in XRD with 2-theta range of 25-40° to show a decrease in impurity phases (● - $SrMoO_4$, ♦ - $Sr_{11}Mo_4O_{23}$, ▲ – NiO).

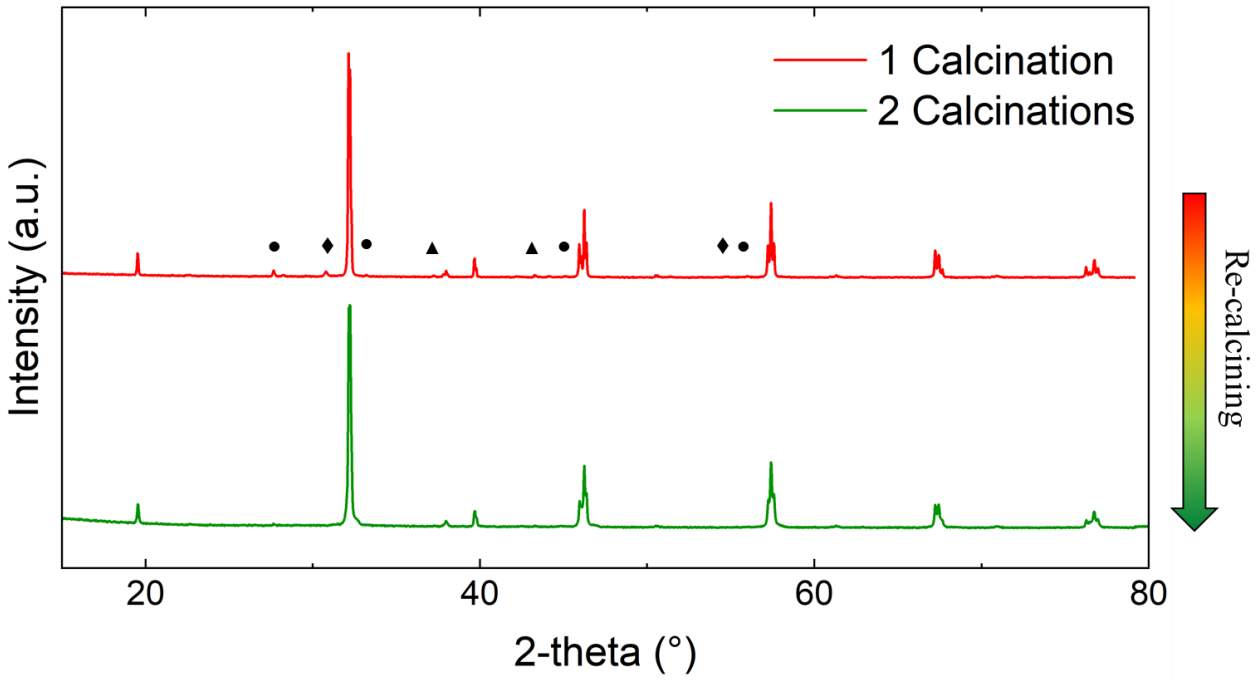

Figure 55. XRD patterns for SFNM144 after both calcination steps (● - $SrMoO_4$, ♦ - $Sr_{11}Mo_4O_{23}$, ▲ – NiO).

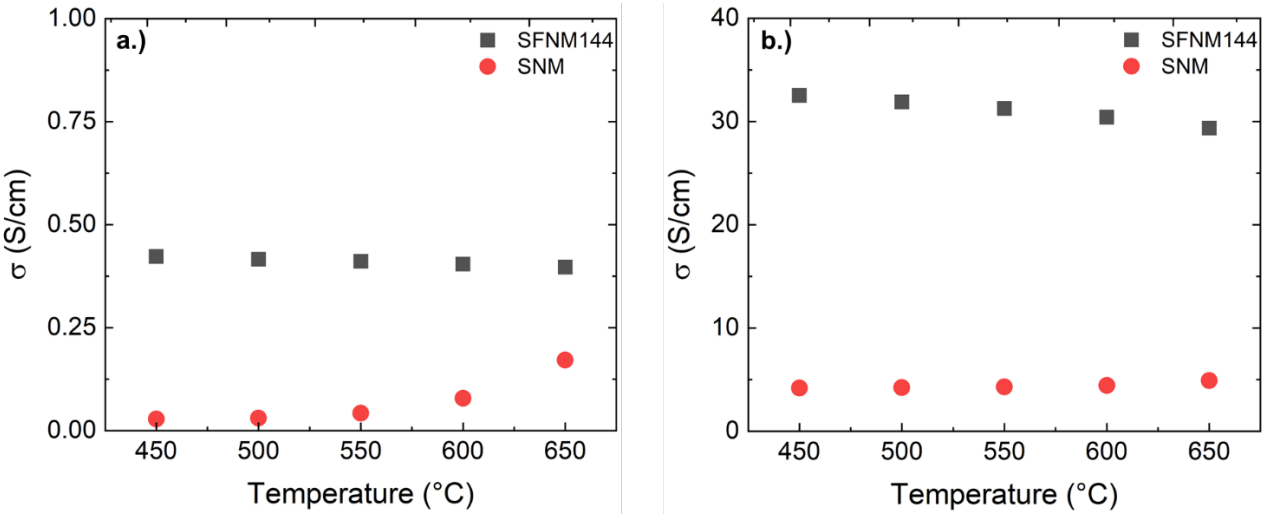

Figure 56. Conductivity of SFNM144 and SNM over the temperature range of 450 – 650°C in (a) air and (b) pure H_2.

Surface Modification on Ceramic Anodes via *in situ* Strain Relaxation

Ceramic Anode Material Synthesis

A wide range of ceramic anode materials following the composition of $SrFe_xNi_{(1-x)/2}Mo_{(1-x)/2}O_{3-\delta}$ (SFNM) were synthesized by the solid-state method. The process consisted of mixing stoichiometric amounts of $SrCO_3$ (Aldrich), Fe_2O_3 (Sigma), NiO (Fuel Cell Materials), and MoO_3 (Alfa-Aesar) and milling in ethanol for 24 hours. Next, the slurry was dried overnight and the homogeneous mixture was collected into an alumina crucible, and then calcined at 1100°C for 4 hours. Eight compositions were made and named according to Table 2.

Table 2. $SrFe_xNi_{(1-x)/2}Mo_{(1-x)/2}O_{3-\delta}$ (SFNM) compositions synthesized in this study.

x =	Name
1.00	SFNM-100
0.90	SFNM-955
0.80	SFNM-811
0.50	SFNM-522
0.34	SFNM-333
0.20	SFNM-244
0.10	SFNM-144
0.00	SFNM-055

Phase Identification of Anode Material Powder

Figure 57 (a) shows the XRD of all SFNM compositions. The phases of the resultant powders were checked by X-ray diffraction (XRD) using a Bruker D8 Advance. For the compositions in which x = 1.0 and 0.9, the phase matches the XRD pattern for cubic perovskite $SrFeO_{2.96}$. For the compositions in which x = 0.0 and 0.1, the phase matches a tetragonal perovskite Sr_2NiMoO_6. For all compositions in between, there is a clear shift from cubic to tetragonal perovskite.

Phase Stability of Anode Material in Reducing Conditions

In order to check the anode material stability in reducing conditions at high temperature, anode material powders were reduced in 100% dry H_2 at 600°C for 24 hours. Then, the phase of the powder was checked again by XRD as shown in **Figure 57. (b)**. SFNM-955 and SFNM-811 showed a phase transition to a brownmillerite structure ($A_2B_2O_5$). For the compositions with higher Ni/Mo content, a minor impurity phase $A_4B_2O_8$ appeared after reduction, increasing with an increase in Ni/Mo loading. Interestingly, SFNM-055, the composition with the most Ni/Mo (but no Fe) showed no phase change in reducing conditions.

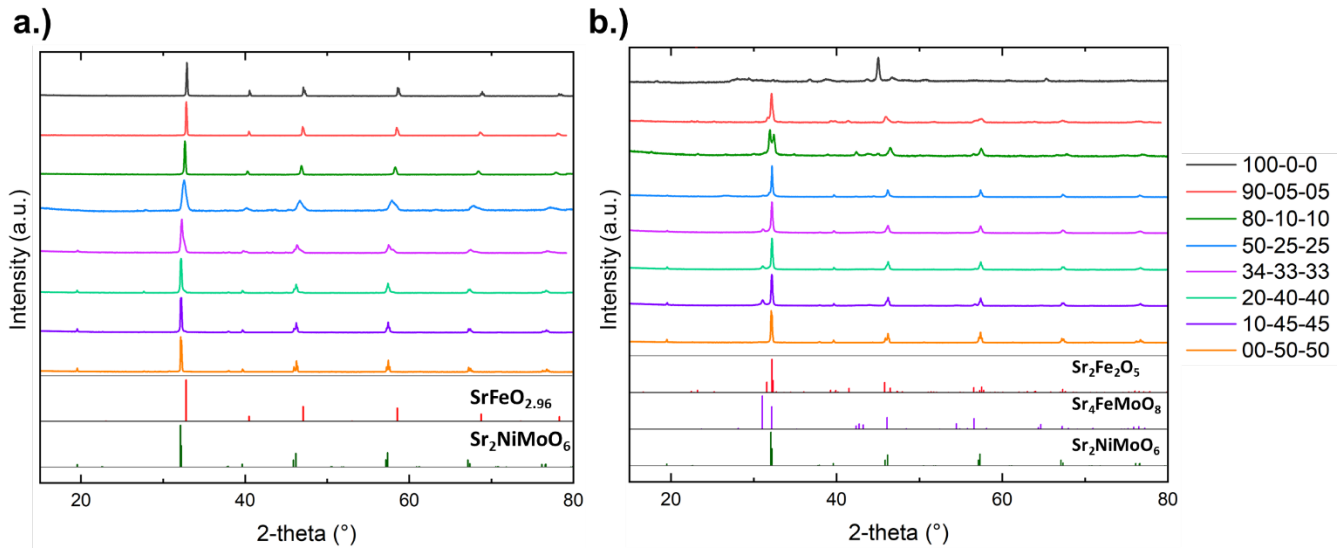

Figure 57. XRD results for SFNM powders. (a) As synthesized and (b) after reduction in 100% H_2 for 24 hours. The Fe:Ni:Mo ratio is shown in the right.

Conductivity of Ceramic Anodes

The conductivity of the anode material is extremely important for an anode-supported fuel cells. If the anode layer (on the order of hundreds of microns) is not sufficiently conductive, major electrochemical losses will be observed.

To test conductivity, dense samples of all compositions were fabricated by uniaxially pressing powder into pellets and sintering at 1340°C for 4 hours. The pellets were cut into bars for conductivity testing. 4-probe measurements were taken using a Keithley 2400 SourceMeter over the range of 450-650°C in air and pure H_2 environments. The conductivity results in air and H_2 are presented in **Figure 58 (a)** and **Figure 58 (b)**, respectively. **Figure 58 (c)** shows the conductivity of SFNM as a function of Fe content (x in $SrFe_xNi_{(1-x)/2}Mo_{(1-x)/2}O_{3-\delta}$). Next, the activation energies were calculated for each composition and shown in Table 3.

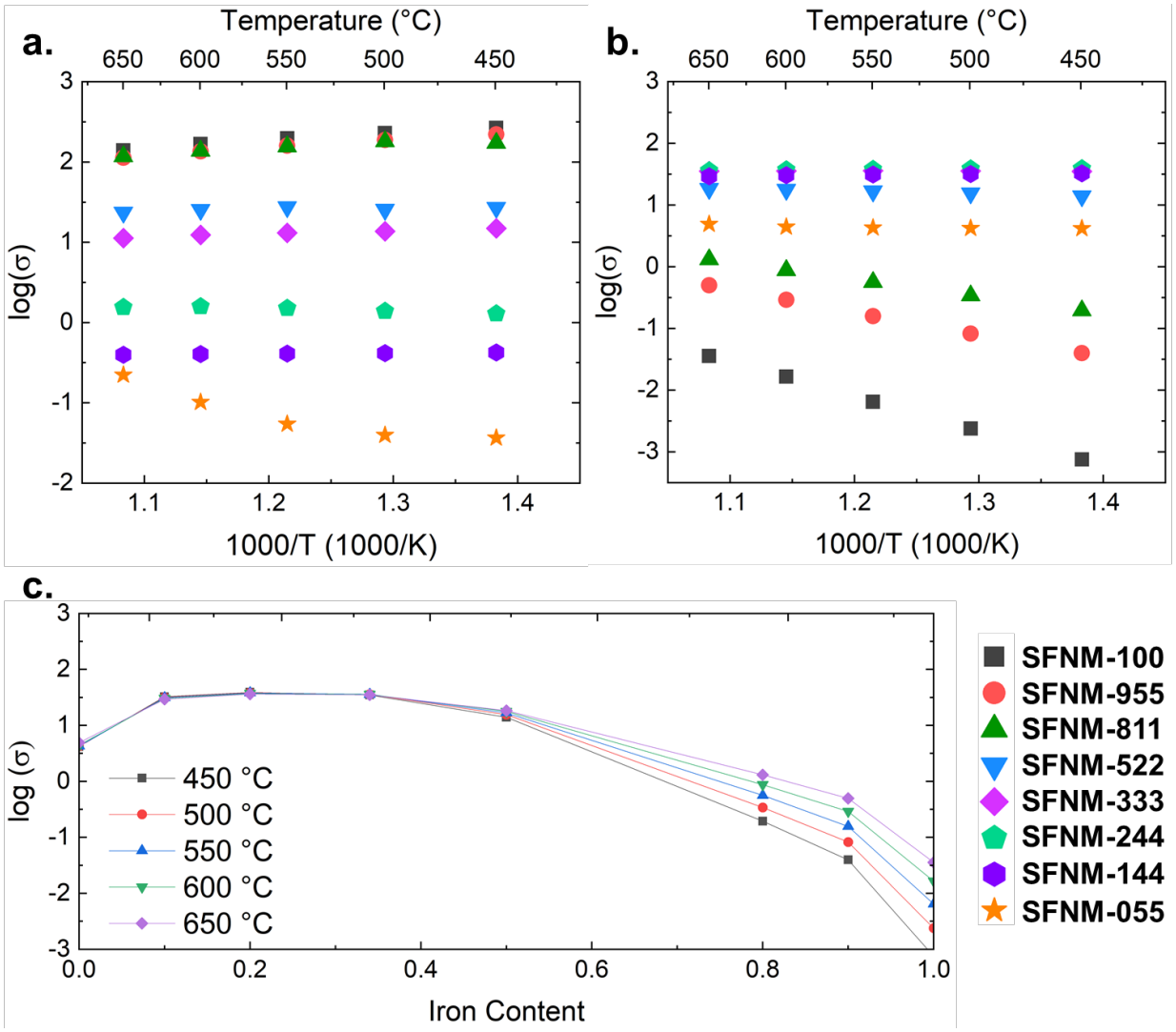

Figure 58. Conductivity results plotted in the form of Arrhenius plots in (a) air environment and (b) H_2 environment. (c) Conductivity trend as a function of iron content in SFNM where the x-axis is x in $SrFe_xNi_{(1-x)/2}Mo_{(1-x)/2}O_{3-\delta}$.

Table 3. Activation energies for all measured compositions of SFNM

Composition (Fe-Ni-Mo)	Activation Energy (eV)
SFNM-100	1.18
SFNM-955	0.798
SFNM-811	0.619
SFNM-522	0.150
SFNM-333	0.073
SFNM-244	0.049
SFNM-144	0.041
SFNM-055	0.111

Observation of In-Situ Surface Modification

The exciting property of the SFNM is the ability to modify the surface by exsolving metallic nano-electrocatalysts to the surface under a reducing condition – effectively modifying the electrode surface during operation. To illustrate this process, SFNM powders were reduced in pure H_2 for 24 hours, and the changes in surface morphology were characterized by scanning electron microscope (SEM). The before and after SEM of SFNM-522 is shown in **Figure 59**. This *in situ* surface modification technique is expected to provide catalytically active sites for fuel oxidation.

To study the trend between composition and exsolved particles, all SFNM compositions reduced were observed under SEM. **Figure 60** shows the reduced powders of all compositions. It is clear that the number/size of particles varies with composition: those with high Fe content show larger particles than those with less (or no) Fe.

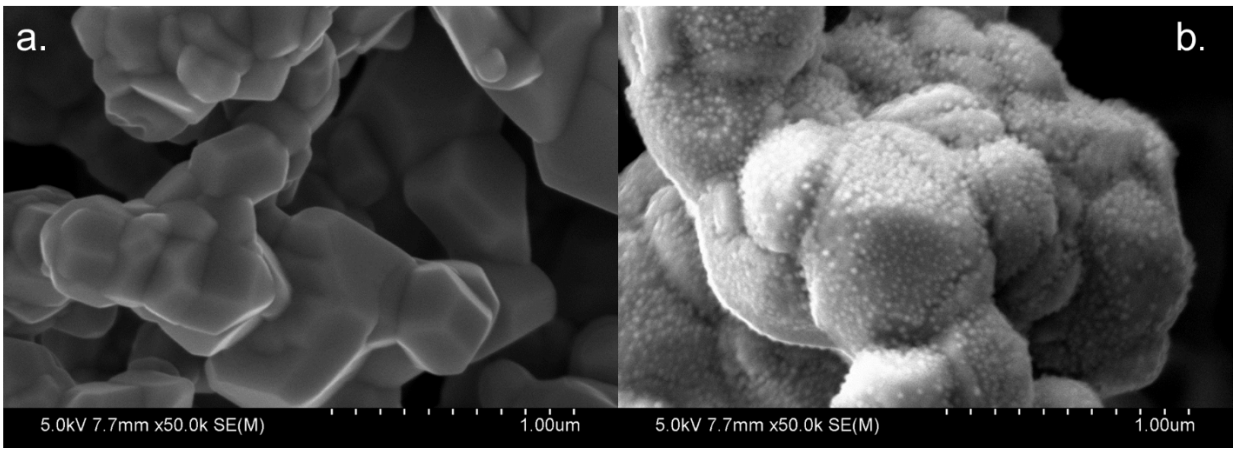

Figure 59. SEM image of SFNM-522 particles (a) before reduction and (b) after reduction at 600°C in pure H_2 for 24 hours

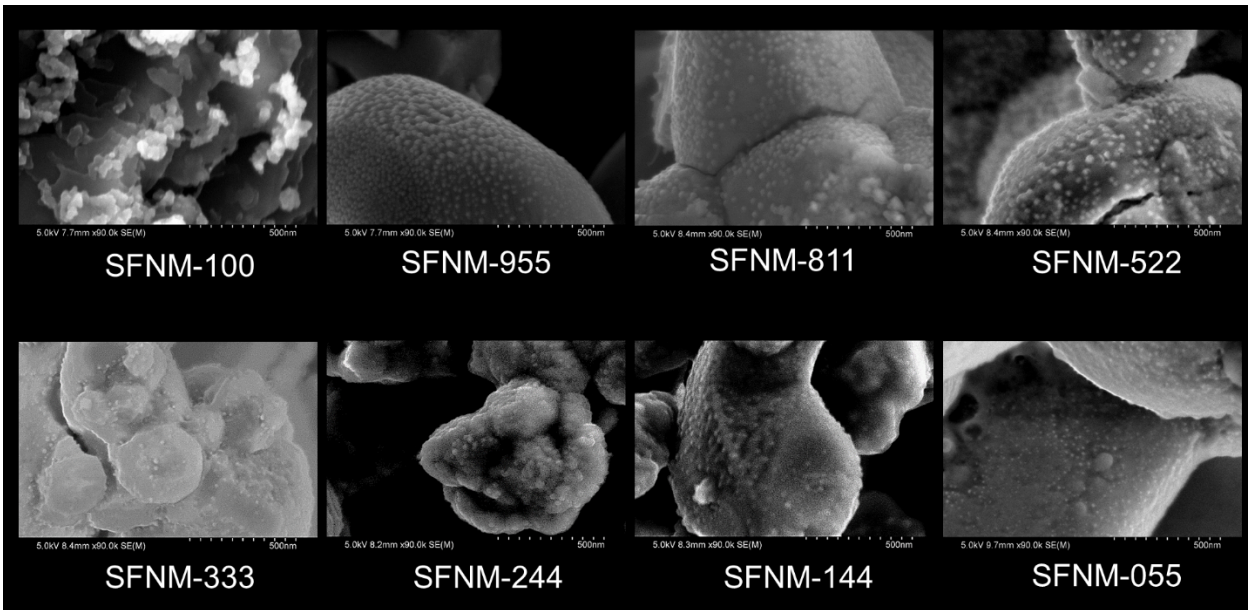

Figure 60. SEM comparison of SFNM powder after reduction for 24 hrs in pure H_2. All images are taken at 90,000x magnification.

Electrolyte-Supported Full Cells

The performance of the SFNM anode was tested electrolyte supported cells. SFNM-244 is selected because of the high conductivity in the reducing condition. GDC disks (thickness of ~200μm) were prepared by tape casting. SFNM-GDC composite paste was made for SFNM-244 and applied to the GDC disks by blade-coating and sintering at 1150°C for 2 hours. $Sr_{0.5}Sm_{0.5}CoO_{3-\delta}$ – GDC (SSC-GDC) paste was subsequently applied as cathode and fired at 950°C for 2 hours.

The resultant cell was tested in two steps. 1) *Reducing step* – where the cell was introduced to wet H_2 at 600°C and impedance measurements were carried out to monitor the changes in the total cell resistance. Every 10 minutes, a full-range EIS was carried out, followed by an I-V sweep. 2) *Aging step* – where the cell was continuously operated under a current density of 0.1 A/cm^2 interrupted hourly by full-range EIS and I-V sweeps. The open-circuit-voltage was also measured in hourly intervals.

During the *reduction step*, the non-ohmic impedance shrinks (see **Figure 61 (a)**), likely due to the in-situ exsolution process providing an increased surface area with active sites for electro-oxidation. Also, the ohmic impedance decreases because the conductivity increases as the SFNM reduces. The peak power density (PPD) also increases, in agreement with the shrinking impedance, as seen in **Figure 61** (b).

Next, the cell was run in the *aging step* for 100 hours. All measurements were done at 600°C in wet H_2. From **Figure 61 (c)**, it is clear that the impedance grows during the initial 72 hours but then stabilizes. The cause of this growth in non-ohmic impedance is unclear but could be due to the agglomeration of metallic particles on the surface. **Figure 61 (d)** shows the I-V and calculated power density sweeps for the aging process. Finally, the long-term galvanostatic data is plotted in **Figure 61 (e)** to show the initial degradation process followed by the stable operation of an SFNM-244 cell.

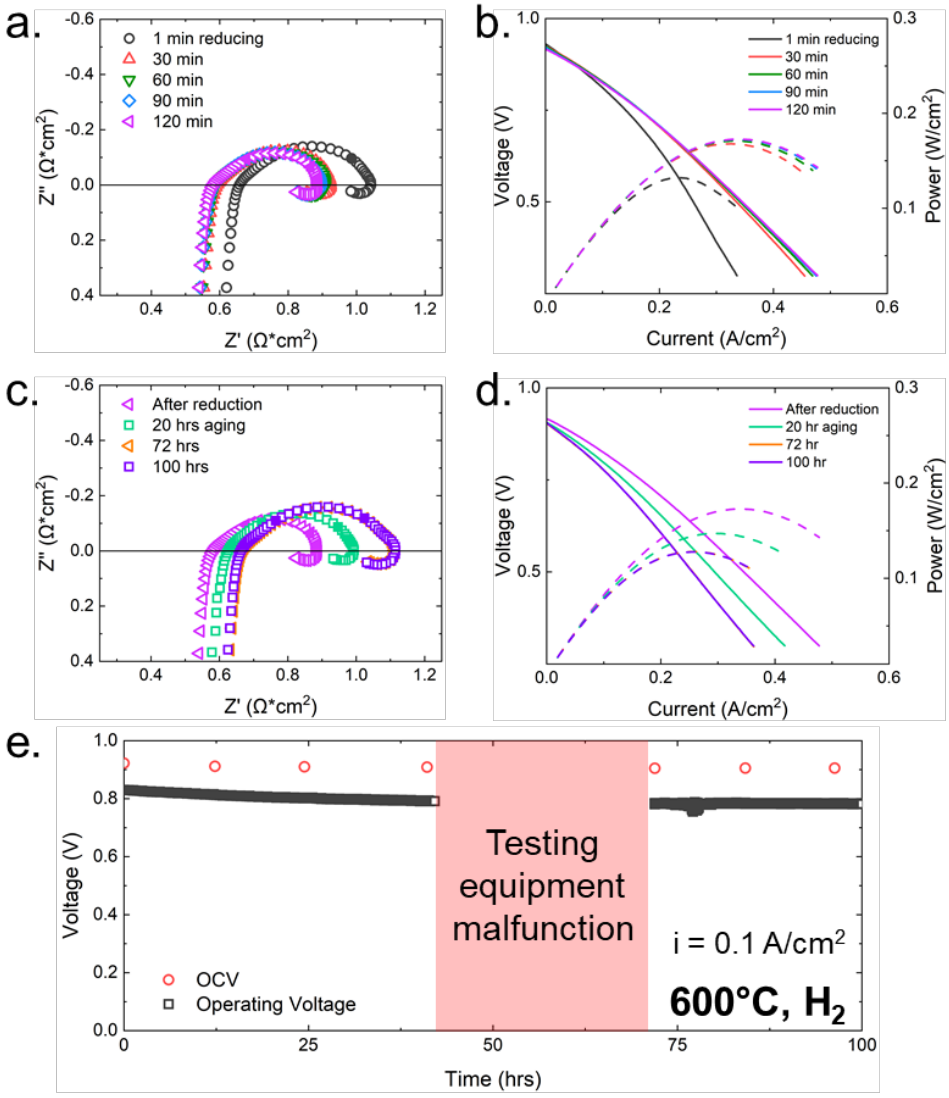

Figure 61. Electrochemical testing results for SFNM-244/GDC | GDC | SSC/GDC cell at 600°C. (a) Impedance results during the initial reduction of the cell, (b) I-V results during the initial reduction, (c) impedance results during the aging process, (d) I-V results during the aging process, and (e) long term aging results showing OCV and operating voltage under a constant current of 0.1 A/cm^2. The Solartron Potentiostat stopped functioning during aging and was recovered later on.

SFNM Exsolution Analysis

To understand the chemical composition of exsolved nano-catalysts, x-ray photoelectron spectroscopy (XPS) and transmission electron microscopy (TEM) were used. XPS results for SFNM before reduction shows no sign of metal, but after reduction, B-site metals are seen on the surface. Ni 2p XPS scan revealed the formation of metallic Ni on SFNM-055 and SFNM-522 after reduction, shown by the formation of the peak around 852eV in **Figure 62 (b).** Furthermore,

compositions with Fe exsolve metallic Fe, evidenced by the peak around 707eV in the Fe 2p scan for SFNM-522 in **Figure 62(c).** Interestingly, in addition to Ni^0 and Fe^0, compositions with high Mo loading exsolved metallic Mo^0, seen in **Figure 62(a).** The exsolution of metallic Mo is not widely reported, and this discovery could open the door to new functional catalysts prepared by *in-situ* surface modification.

An elemental analysis of the surface particles was carried out using dark-field scanning/transmission electron microscopy with energy dispersive x-ray spectroscopy. The results revealed the nano-catalysts have a high concentration of Fe and Ni, as seen in **Figure 62(d).** Furthermore, it appears the Ni was completely exhausted from the lattice at the particle/bulk interface, but Fe was not.

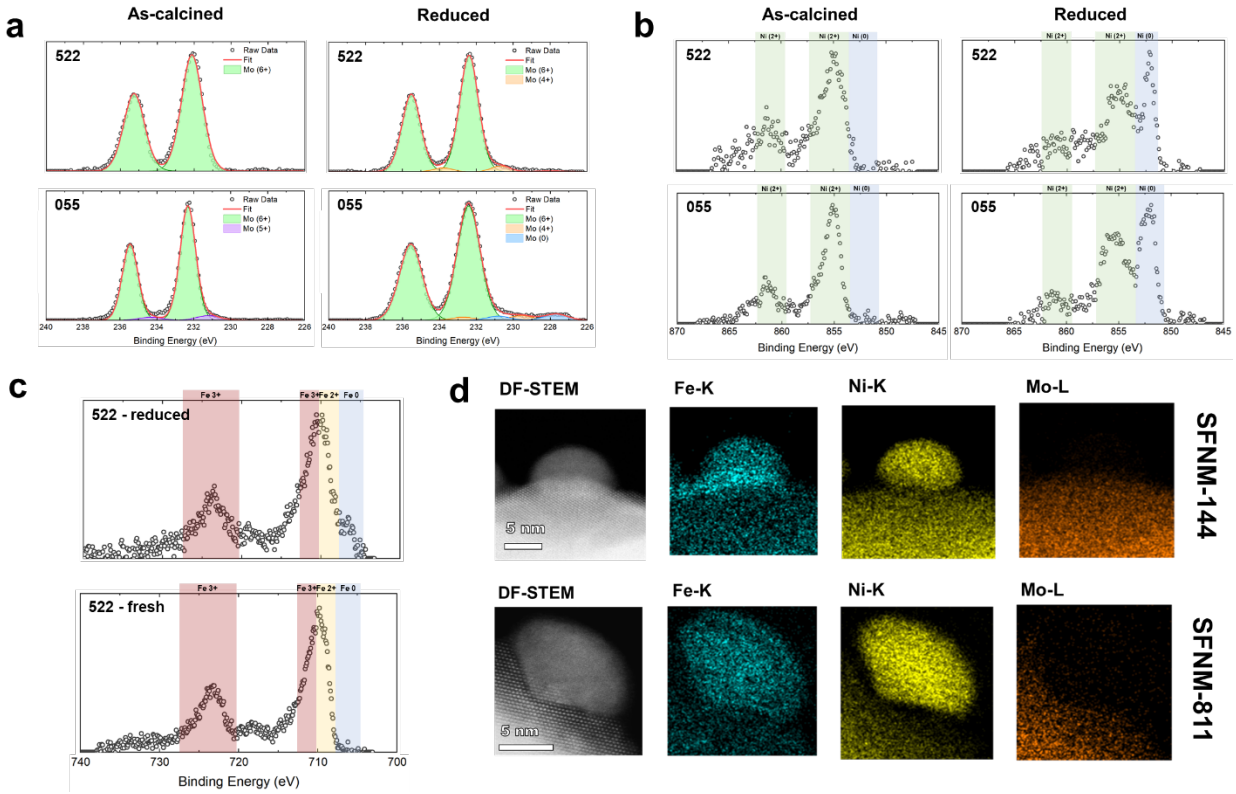

Figure 62. SFNM surface analysis. a) Mo 3d XPS scan reveals the formation of metallic Mo in some compositions. b) Ni 2p XPS scan shows the exsolution of metallic Ni. c) Fe 2p scan shows the appearance of metallic Fe peak after SFNM reduction. d) TEM-EDS analysis of nano-catalysts exsolved from two different SFNM compositions: SFNM-144 and -811.

SFNM as Anodes for SOFCs

GDC disks (thickness of ~200μm) were prepared by tape casting. SFNM-GDC composite paste were made for SFNM-055, -244, and -333 and applied to the GDC disks by blade-coating

and sintering at 1150°C for 2 hours. $Sr_{0.5}Sm_{0.5}CoO_{3-\delta}$ – GDC (SSC-GDC) paste was subsequently applied as cathode and fired at 950°C for 2 hours. The resultant cell was tested in two steps. 1) *Reducing step* – where the cell was introduced to wet H_2 at 600°C and continuous low frequency (0.1Hz) impedance measurements were carried out to observe the total resistance of the cell. Every 10 minutes, a full-range EIS was carried out, followed by an I-V sweep. 2) *Aging step* – where the cell was continuously operating under a current density of 0.1 A/cm^2 interrupted hourly by full-range EIS and I-V sweeps. The open-circuit-voltage was also measured in hourly intervals.

The cell performance during the initial reducing step is summarized by **Figure 63**. All cells show a decrease in area specific resistance (ASR) and increase in peak power density (PPD) over time, but the kinetics vary significantly – SFNM-055 improves slower than SFNM-244 which improves slower than SFNM-333. This "improvement" is likely the process of exsolution which provides an increasing amount of electrochemically active sites for hydrogen oxidation. Additionally, after the 2 hr reducing step, SFNM-333 has the best performance, likely due to the fast exsolution kinetics providing the most active sites under the same amount of the reduction time.

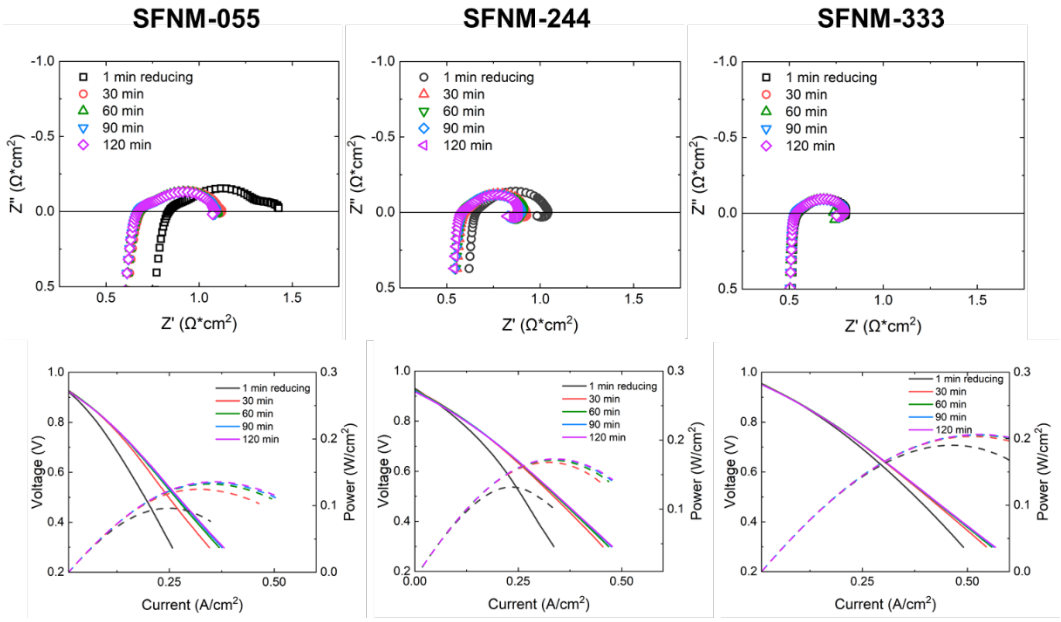

Figure 63. Reducing step results including EIS and IV curves for full cells with composite anodes SFNM-055, -244, -333 with GDC at 600 °C.

Long term performance results are shown in

Figure 64. All compositions showed similar degradation over the 100-hour testing period, but a trend emerged revealing that the degree of degradation was less severe for compositions with less Ni/Mo doping. In other words, the composition with the highest initial performance, also had the least degradation.

Figure 65 summarizes the OCV and cell operating voltage (0.1 A/cm^2) over the 100-hour aging step. The OCV is relatively constant over the entire period, and the operating voltage shows the least degradation for SFNM-333, which is in good agreement with the open-circuit EIS results. Our results show that our approach of using *in situ* metal alloy exsolution on a conductive ceramic anode achieves both high performance and durability.

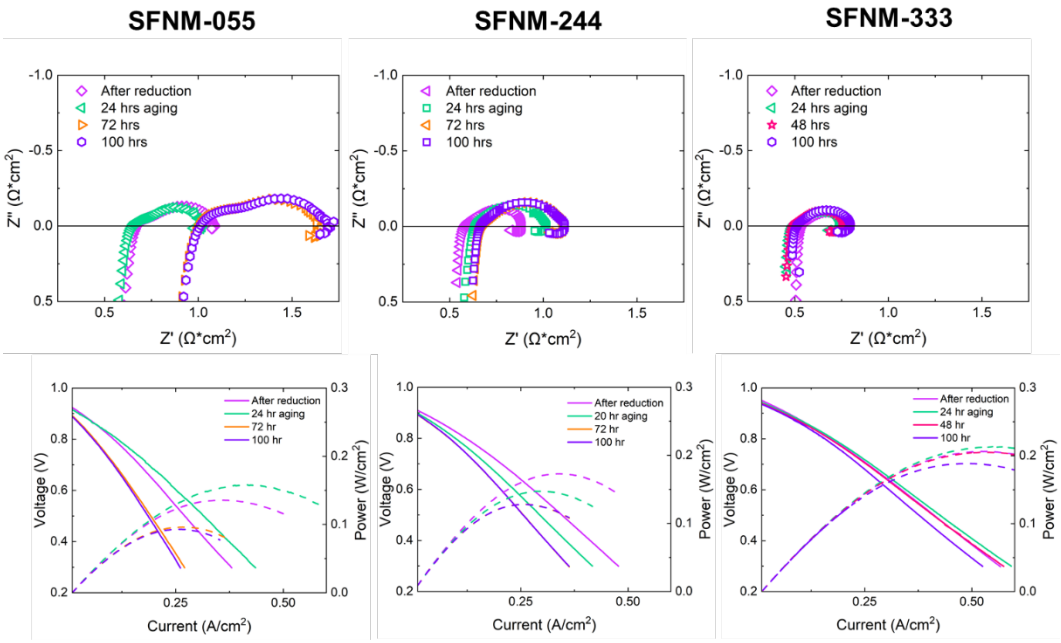

Figure 64. EIS and IV results from the aging step for full cells with composite anodes SFNM-055, -244, -333 with GDC at 600 °C in H_2.

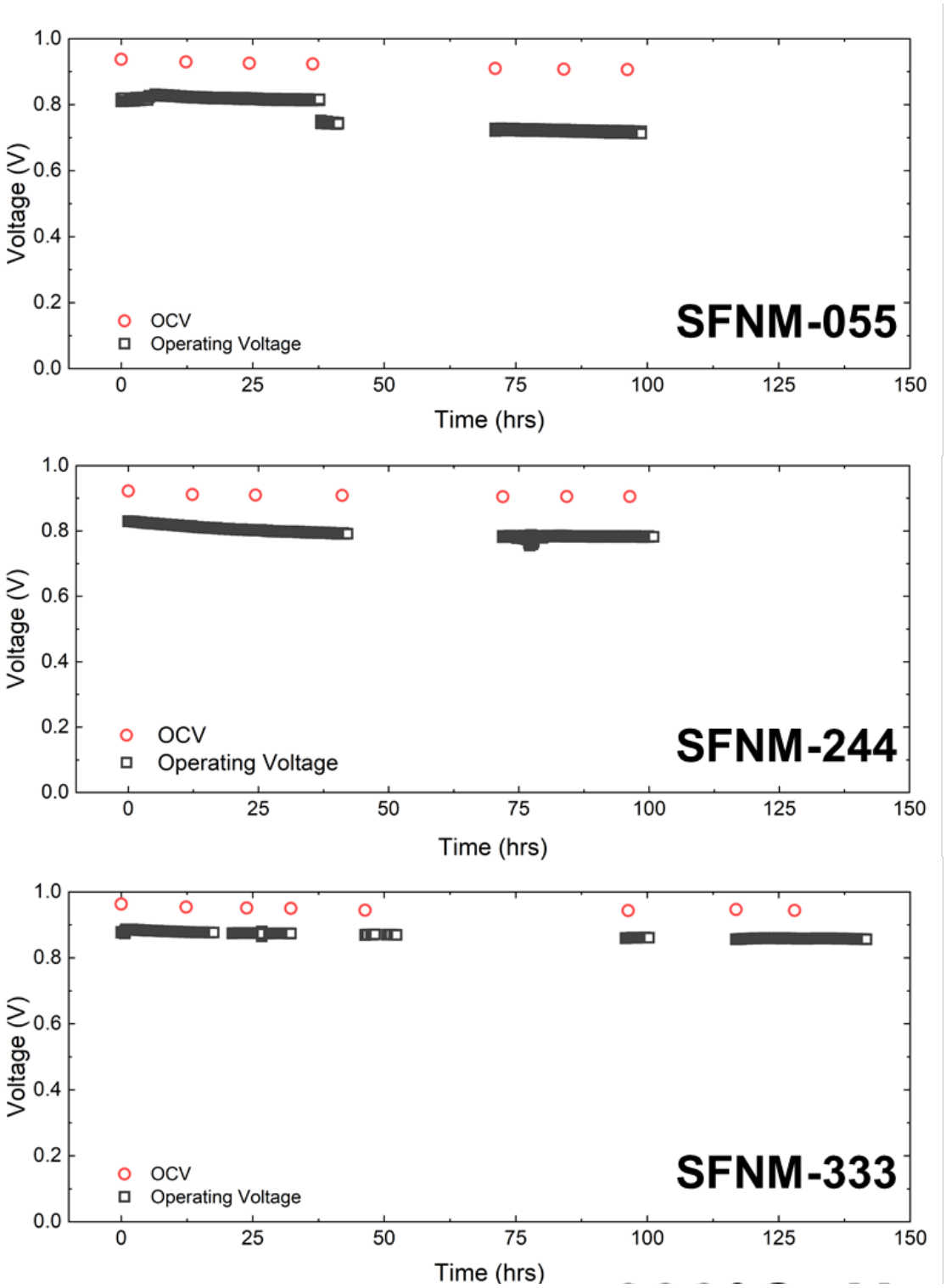

Figure 65. Aging results including OCV over time and operating voltage response (0.1 A/cm^2) at 600 °C.

SFNM Electrolyte-Support Study

A survey of the electrochemical performance of four different SFNMs was carried out to identify the optimal composition for an SOFC anode. SFNM-055($SrNi_{0.5}Mo_{0.5}O_{3-\delta}$), -244($SrFe_{0.2}Ni_{0.4}Mo_{0.4}O_{3-\delta}$), -333($SrFe_{0.34}Ni_{0.33}Mo_{0.33}O_{3-\delta}$), and -522($SrFe_{0.5}Ni_{0.25}Mo_{0.25}O_{3-\delta}$) composite anodes were made and deposited onto four different cells. **Figure 66(a)** is a schematic representation of each cell while **Figure 66**(b) shows the SEM image of the SFNM-333 full cell that was tested at 600°C with H_2 fuel. A higher magnification image of the anode | electrolyte interface shows good contact and is provided in **Figure 66**(c).

The electrochemical performance of each cell is shown in **Figure 66**(d) and (e). With an increase in Fe content, the total area-specific-resistance (ASR) decreases, accompanied by a slight increase in OCV. This is likely due to the high concentration of oxygen vacancies that form under reducing conditions for compositions with high Fe, supported by the TGA data in **Figure 66**(f). The increased concentration of charge carriers reduces resistance and provides more active sites for the fuel oxidation reaction.

A high magnification SEM of the microstructure of the anode was taken before and after testing for the SFNM-333 cell to characterize the *in situ* formation of surface catalysts. The before and after images are provided in **Figure 67**(a) and (b), respectively. Before operation, each particle is smooth, but after exposure to H_2 at 600°C during testing, nanoparticles clearly exsolve to the surface, verifying the ability for *in situ* surface modification.

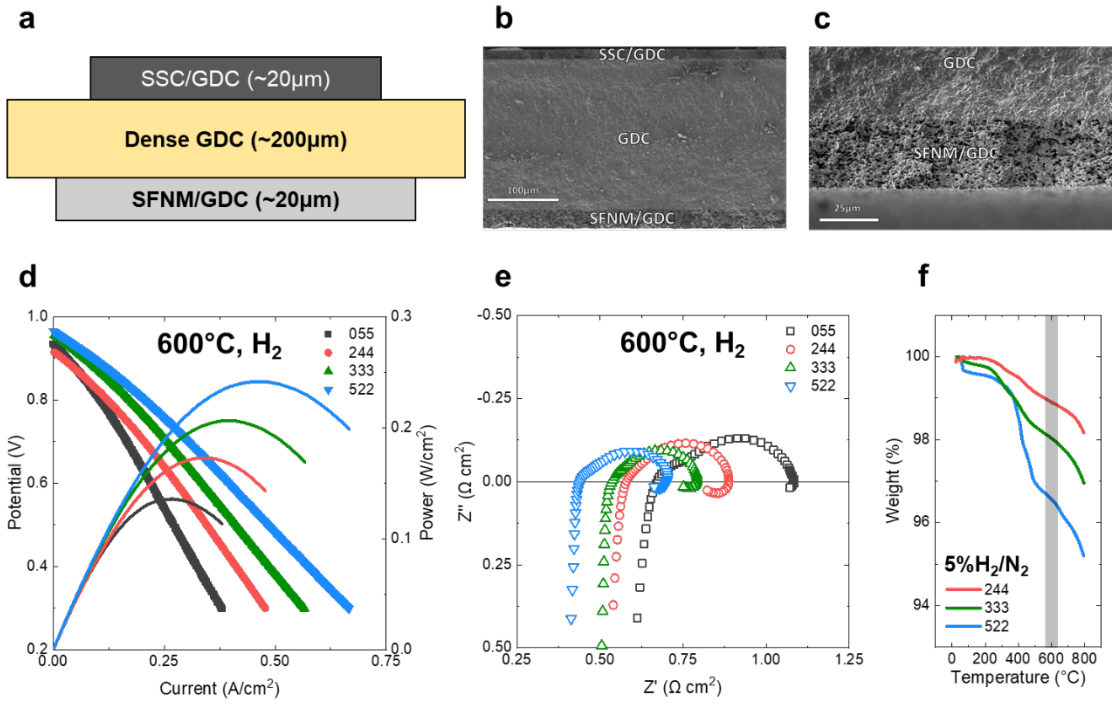

Figure 66. Result from the electrolyte-supported cell study to screen SFNM activity. (a) a schematic for the 4 cells made and tested. (b) SEM image of the full cell and (c) anode-

electrolyte interface. (d) iV curves recorded at 600°C with H_2 fuel and (e) corresponding EIS sweeps at OCV. (f) TGA results from different SFNM compositions in reducing environment.

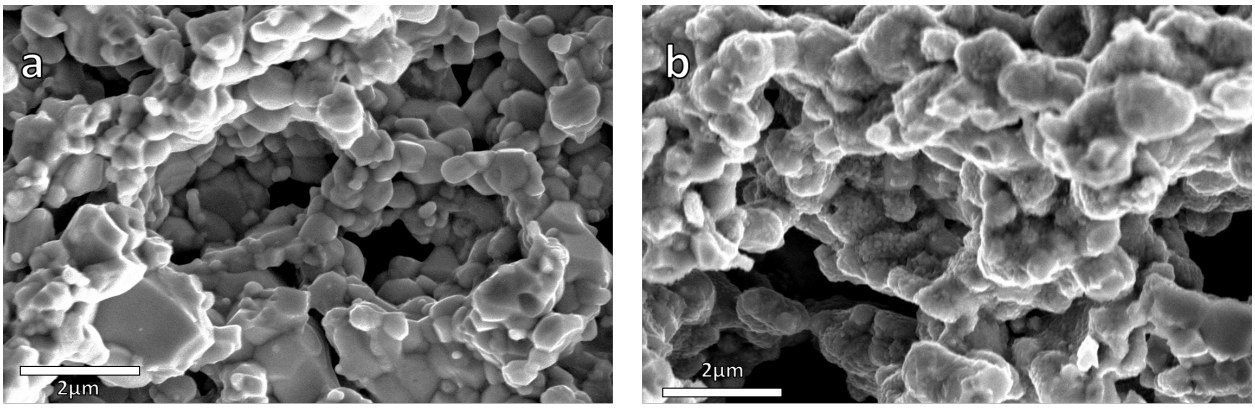

Figure 67. High magnification SEMs of the SFNM-333 composite anode (a) before and (b) after operation in H_2 at 600°C.

Development and Characterization of SFNM-Supported Cells

Next, ceramic-anode-supported cells were engineered by a tape-casting/lamination procedure. The 300µm-thick composite anode supports a 20µm GDC electrolyte. An SEM image of the entire half-cell and a magnified view of the anode | electrolyte interface are provided in **Figure 68(a)** and (b). The back-scatter SEM image in **Figure 68**(c) shows the distribution of SFNM (darker grains) and GDC (brighter grains). A schematic is provided in **Figure 68**(d) to characterize the ceramic-anode-supported-half-cells that were successfully fabricated.

A Pr-GDC cathode functional layer (CFL) and SSC-GDC cathode layer was sintered onto the ceramic half-cell to make a full cell, then the cathode was infiltrated with Pr (see **Figure 69c**). Once finished, the cell was sealed, heated to 600°C, and fueled with H_2 electrochemical measurements were taken regularly over time to probe the performance changes with respect to in-situ exsolution. **Figure 68**(e) and (f) show the electrochemical data. Initially, the cell has a total ASR of 0.63 Ωcm^2 and peak power density (PPD) of 210 mW/cm^2. After reducing the cell for 2 hours to promote in-situ surface modification, the ASR was reduced by ~35% to 0.41 Ωcm^2, resulting in a PPD improvement of ~52% (320 mW/cm^2).

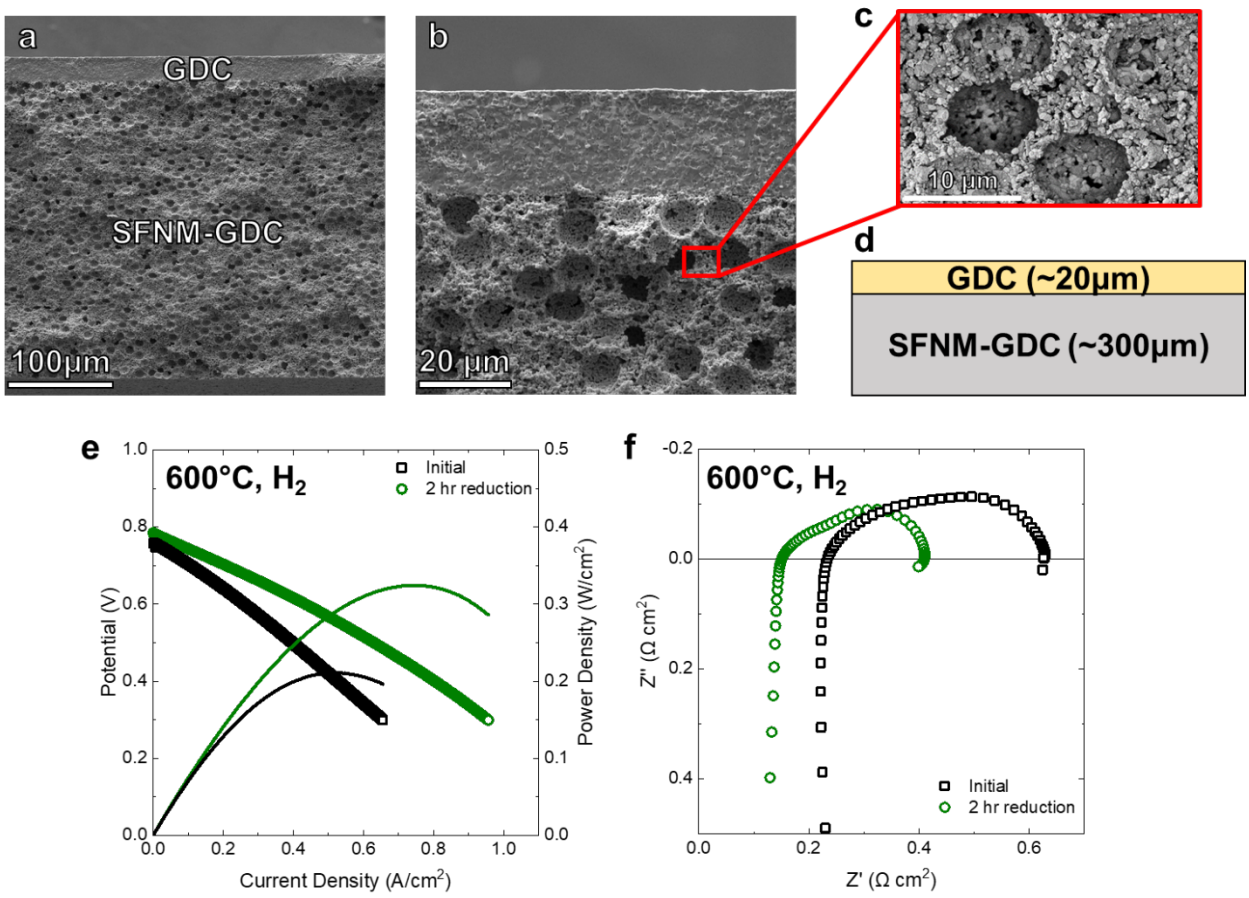

Figure 68. SEM images of (a) the ceramic anode supported cell and (b) ceramic anode | electrolyte interface. (c) Backscatter image showing the distribution of SFNM (darker grains) and GDC (brighter grains) within the composite anode. (d) Schematic describing the configuration of ceramic half-cells. (e) iV curves at 600°C with H_2 fuel and (f) corresponding EIS sweeps at OCV.

Two other anode-supported cells were tested and aged prior to the cell characterized above. The first was a reference cell: a half-cell with only SSC-GDC cathode layer, shown in **Figure 69**(a). This cell had a particularly low OCV resulting in poor performance. Based on our labs previous experience with ceramic anodes, a Pr-GDC cathode functional layer (CFL) (**Figure 69**(b)) was added to improve OCV. Pr-infiltration (**Figure 69**(c)) was added to the third cell to decrease ASR.

The performances of these three cells are summarized in **Figure 69**(d) and (e). The Pr-GDC layer effectively increased the OCV when compared to the reference cell. The difference in OCV between the two cells with CFL is likely due to differing thickness of the CFL. Furthermore, the Pr-infiltration on the cathode reduced the cell ASR.

After the initial 2-hour reduction, all three cells were operated under a constant current of 0.2 A/cm^2 for >100 hours and the voltage response is reported in **Figure 69**(f). All cells show an

initial increase in performance and an eventual slow degradation. The abrupt drop in potential for the Pr-infiltrated cell is likely due to a crack.

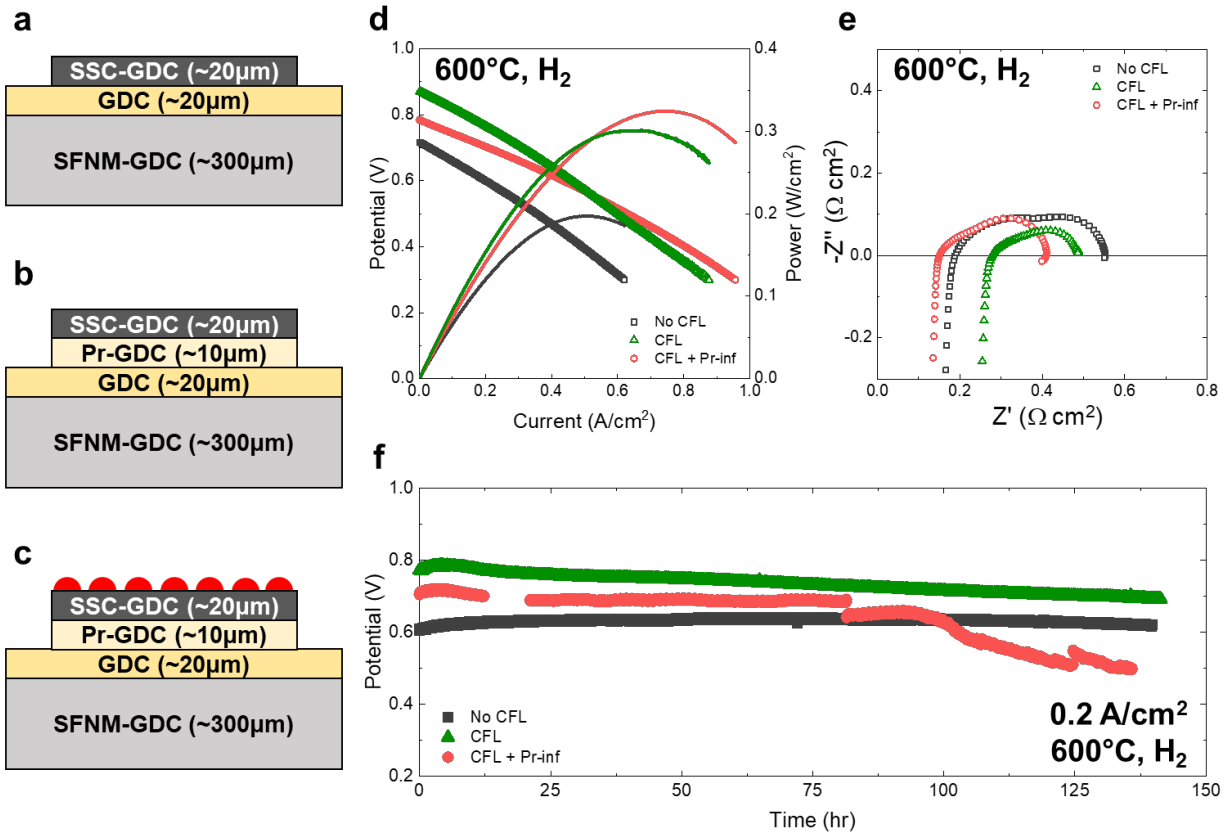

Figure 69. Three SFNM cell configuration tested were (a) without CFL, (b) with CFL, and (c) with CFL + Pr-infiltration on the cathode. (d) iV curves at 600°C with H_2 fuel and (e) corresponding EIS sweeps at OCV. (f) Voltage response to galvanostatic aging at 0.2A/cm^2.

Methane-fueled exsolution-SOFC

Following the development of exsolvable-ceramic-anode supported fuel cells, the durability in a carbon-containing fuel (methane) was investigated. **Figure 70** (a) shows the galvanostatic (0.2A/cm^2) voltage response of the SFNM supported cell and **Figure 70** (b) shows the electrode, ohmic, and total area-specific resistances (ASR) of the cell. Impressively, the cell operated >500hrs without any significant coking failure.

During the initial ~100hrs of operation, the total resistance drops due to the decrease in electrode polarization. This can be explained by the in-situ exsolution of nano-electrocatalysts in the reducing environment. After the initial 100hrs though, an increase in resistance is observed. One possibility for this is the agglomeration of nano-catalysts due to the high temperature of operation (600°C).

Figure 70 (c) and **Figure 70** (d) show SEM images of the ceramic-anode microstructure before and after cell testing, respectively. After operation, the smooth surface of the anode becomes

rough, covered with exsolved particles. No significant buildup of carbon chains was observed, further indicating the exsolved catalysts are resistant to coking failure.

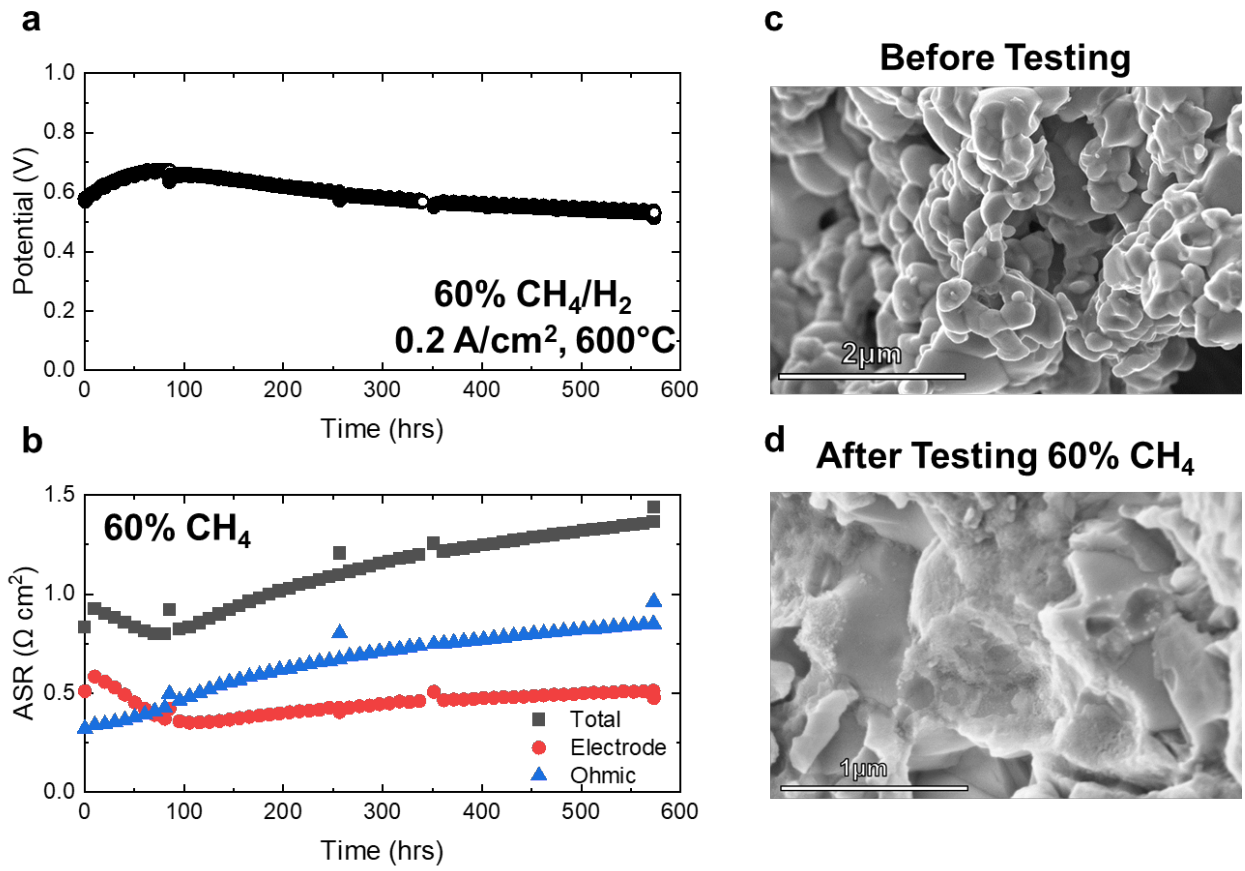

Figure 70. SFNM-GDC supported fuel cell operating off of carbon-containg fuel: 60%CH_4/H_2 bubbled through water. (a) Voltage response to galvanostatic aging (0.2A/cm^2) and (b) deconvoluted ASR at open circuit vs time. (c) SEM micrograph of the anode microstructure before and (d) after operation.

Solution Infiltrated Anode Development

We determined the ideal testing/fabrication methods for $SrFe_{0.2}Co_{0.4}Mo_{0.4}O_{3-\delta}$ (SFCM)-GDC based ceramic anodes to operate on H_2. Shown in **Figure 71** are SEMs of SFCM based ceramic anode supported cells, SFCM-GDC/GDC/Pr-GDC/SSC-GDC cells. SFCM-GDC is the anode support 300-400 μm, GDC electrolyte 20 μm, Pr-GDC cathode functional layer 10μm and SSC-GDC cathode 20 μm. SEM images show the porosity of the anode to infiltrate desired electrodes for high performing low-temperature SOFCs. The purpose of the CFL is to enhance the OCV of the ceramic anode SOFC and the cathode performance. We also optimized the amount of infiltrates, which is 36 μmol/cm^2.

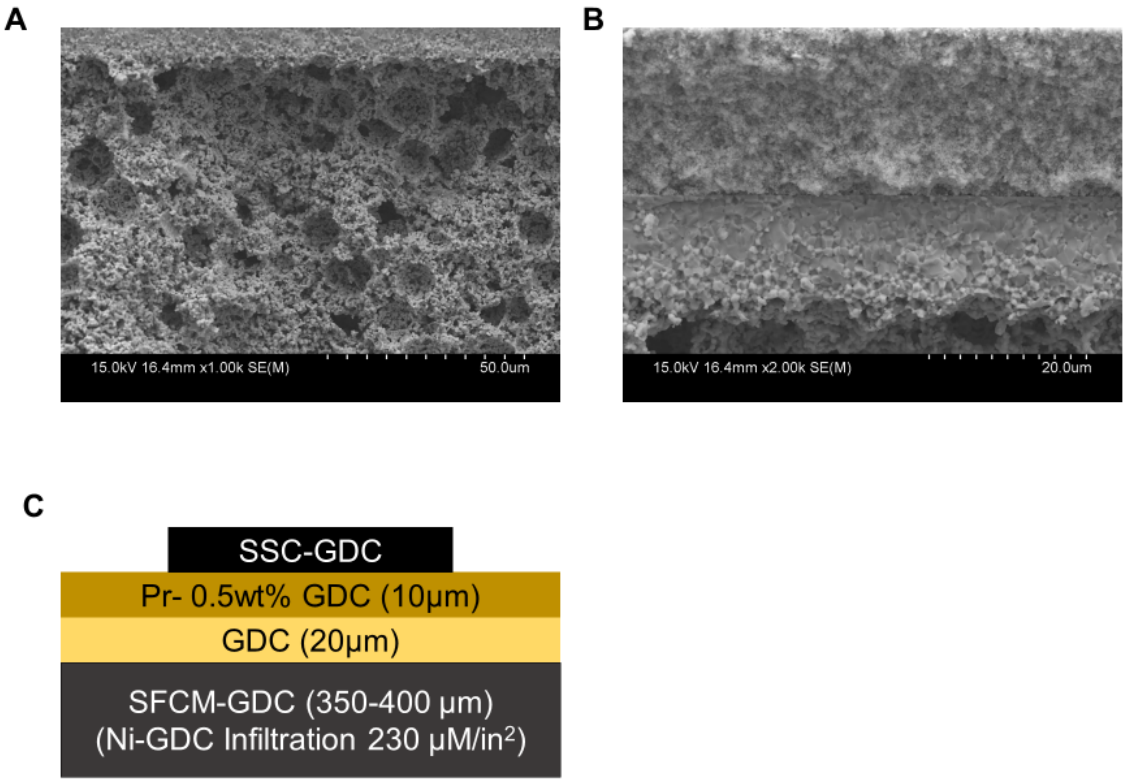

Figure 71 Cell Architecture and Microstructure. (a). Microstructure of SFCM-GDC based ceramic anode showing the high porosity. (b). Microstructure of the CFL, electrolyte and anode with CFL being on top of the dense electrolyte. (c) Overall cell design of ceramic anode supported SOFC.

We optimized the testing procedure for the SFCM ceramic anode. The conventional anode, cermet Ni-GDC needs to be reduced at 650 °C or higher in order to fully reduce the huge chunks of NiO, which have an average size of > 10μm. Using SFCM-GDC ceramic anode, it is possible to reduce the reduction temperature of the anode to 550 °C because of the nanoscale infiltrated NiO particles, which avoids higher temperature processing that causes irreversible degradation of the anode. In **Figure 72** (a), (b), and (c), iV characterization shows the PPD for each cell reduced at 650 °C, 600 °C, and 550 °C respectively. The Nyquist plots on the right of each iV curve in **Figure 72** (d), (e), and (f) show that there is an increase in ohmic and non-ohmic ASR for the cell reduced at 650 °C, compared to 600 °C and 550 °C. As shown in **Figure 72** (d-f), for the cell reduced at 650 °C, the total ASR is about 1 Ωcm^2 whereas it is only 0.5 Ωcm^2 for the cell reduced at 600 °C. For the cell reduced at 550 °C, the ASR is only about 0.4 Ωcm^2.

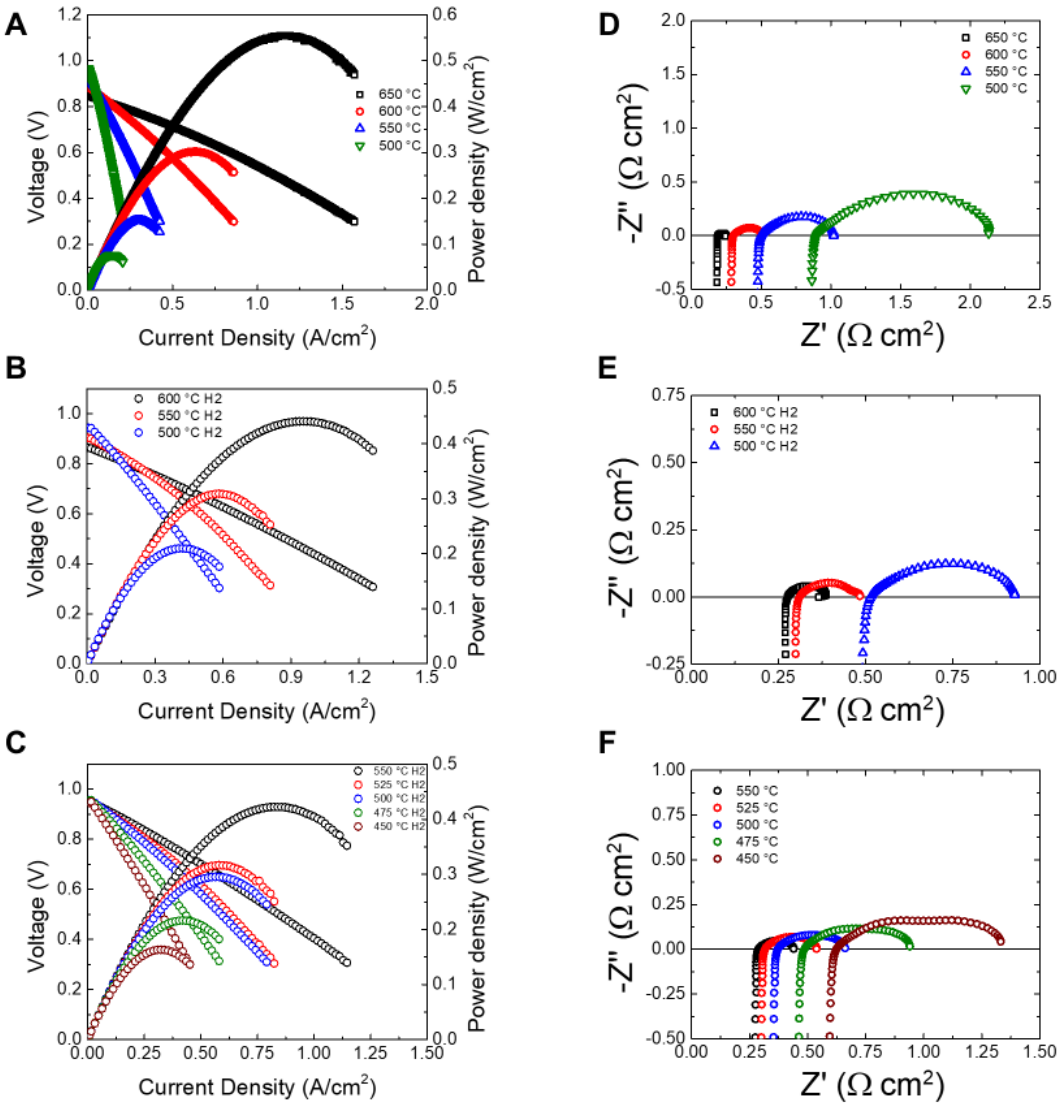

Figure 72. iV and Nyquist Characterization Initial SFCM-GDC Testing Parameters. iV) Characterization of SFCM-GDC Based Ceramic Anode Supported Cells. Cells reduced at (a) 650 °C, (b) 600 °C, and (c) 550 °C Respectively. Nyquist plots of SFCM-GDC based cells reduced at (d) 650 °C, (e) 600 °C, and (f) 550 °C respectively.

Figure 73 highlights the effects of the reduction temperature effect on SFCM-GDC based ceramic anodes. In **Figure 73** The iV curve differences at 550 °C are clearly shown that a lower reduction temperature has a higher PPD as the ASR is much lower.

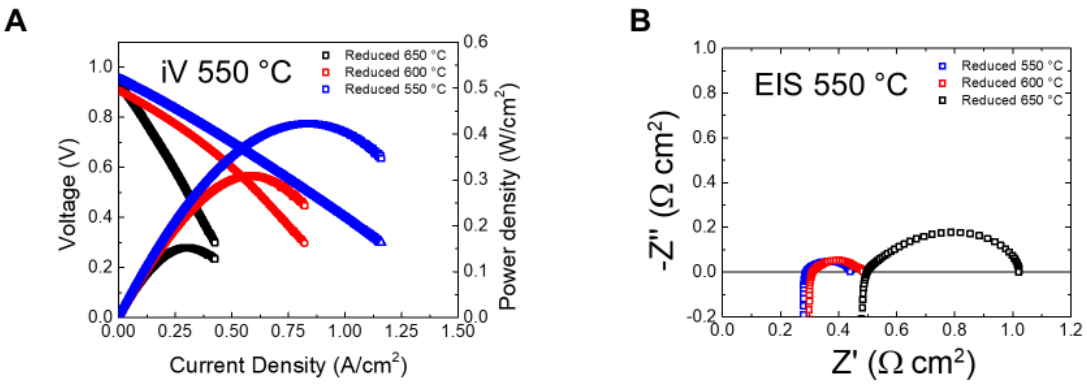

Figure 73 SFCM Cells Tested at 550 °C. (a) iV curves of SFCM based cells based on different reduction temperature. (b) Nyquist of SFCM based cells with different reduction temperature at 550 °C.

We also optimized the operating temperature for the SFCM based ceramic anode SOFC. **Figure 74** shows the aging behavior for the cells aged at 550 °C and 500 °C. The cell reduced at 650 °C was aged at 550 °C because it did not have sufficient PPD at 500 °C whereas the cell that was reduced at 550 °C had sufficient PPD to be aged at 500 °C. **Figure 74** (a) and (b) show the cell voltage under 0.2 A/cm^2 and the PPD of the cell as a function of aging time. Both cells show high stability while operating in H_2 for over 400 hours. The ASR of the cells are also shown in **Figure 74** (c). No severe degradation was observed.

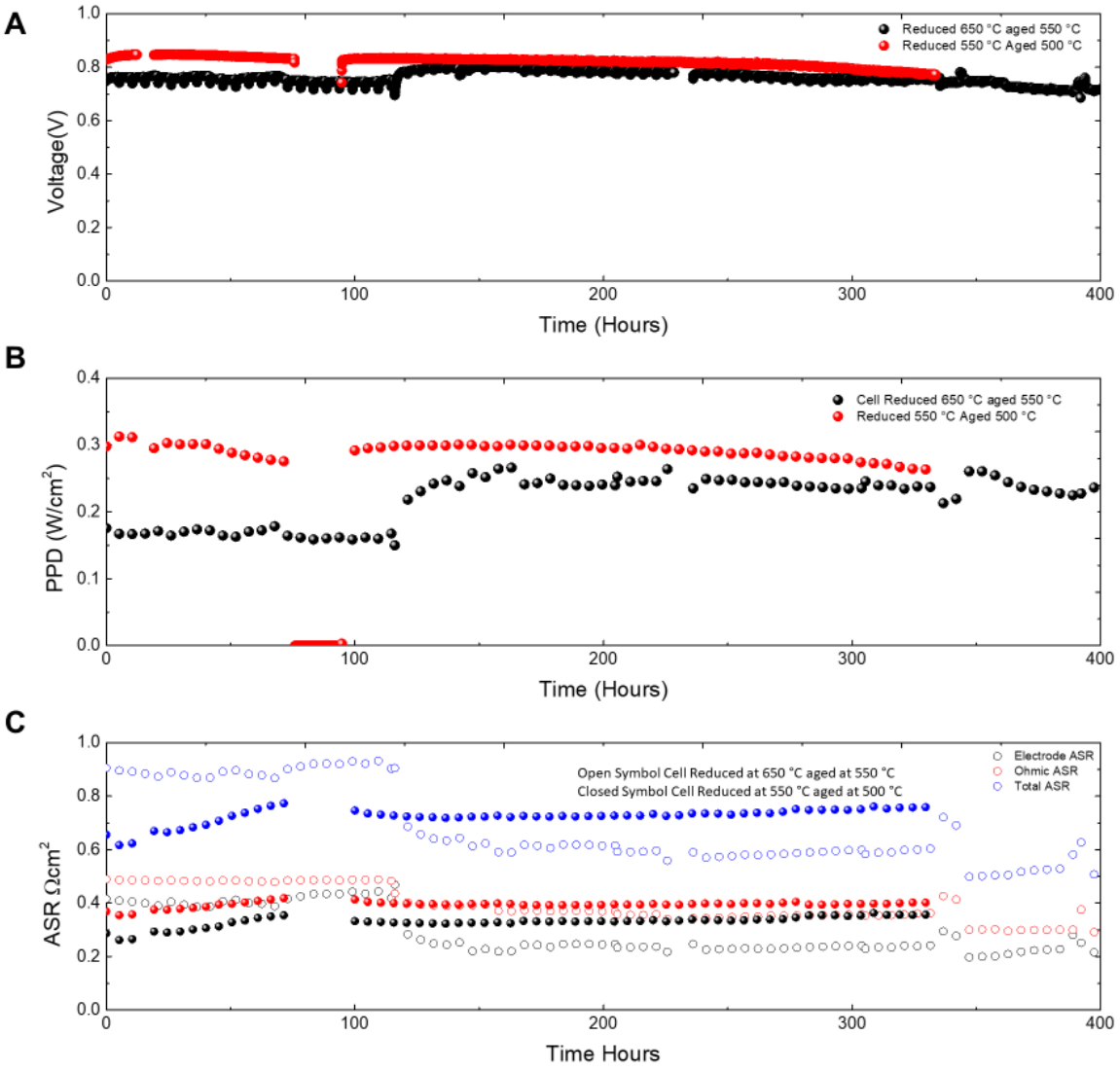

Figure 74. Aging Behavior of SFCM-GDC based cells. (a) The galvanostatic at 0.2A/cm^2 aging condition for the 650 °C reduced and the 550 °C reduced cell. The cell reduced at 650 °C was aged at 550 °C, which have similar performance to the 550 °C reduced cell that operates at 500 °C. (b) the PPD vs time for each cell. (c) the time dependent change in EIS spectra deconvoluted into ohmic and non ohmic vs time for each cell. Open symbol is the cell reduced at 650 °C and the closed symbol is the cell reduced at 550 °C.

Other Modification Approaches

In addition, we investigated the effect of other surface modifications on the SFCM-GDC anode. **Figure 75** (a) shows the performance of a Ru-infiltrated SFCM-GDC on top of the standard procedure of Ni-GDC infiltration. Ru-infiltration enhances the overall performance of SFCM-GDC operating on hydrogen, the PPD is approximately 0.75W/cm^2 at 550 °C compared to that of

0.4 W/cm^2 with the Ni-GDC infiltration. The EIS spectra in **Figure 75** (c) shows that the cell impedance is only 0.5 Ωcm^2 at 500 °C. These results indicate the high activity of the infiltrated ceramic anodes.

Another surface modification was to coat a thin layer of vanadium oxide on top of the standard Ni-GDC infiltration using atomic layer deposition (ALD). ALD was used to modify the anode surface in order to observe the effects on catalytic activity and chemical stability. Similar studies on cathodes suggest that thin metal oxide coatings can improve electrochemical kinetics. Vanadium oxide was chosen due to its reported catalytic activity towards methane and the possibility of forming beneficial secondary phases, such as strontium vanadium oxide, on the anode surface. Other available precursors allow the deposition of titanium, aluminum and zinc oxides.

ALD works by exposing the substrate to alternating pulses of metal precursors and oxidizer. The metal precursor reacts with the substrate but not itself resulting in a self-limiting coating. After unreacted precursor is removed through vacuum, the pulsed oxidizer reacts with the precursor forming a metal oxide and allows subsequent reactions. This entire process constitutes one cycle of ALD. ALD was deposited on the anode side using a Beneq TFS 500 ALD system. 6 layers of vanadium oxide were deposited using Vanadyl Triisopropoxide (VTOP) precursor and ozone oxidizer at 175°C with pulse times of 1 second. The reported growth rates for vanadium oxide are approximately 0.11 Å/cycle.

The I-V curves of the vanadium ALD coated SOFC at 500 and 550 °C are shown in **Figure 75** (b). Compared to solution infiltrated SOFCs, vanadium ALD, however, does not enhance the activity of the anode as the PPD is only about 0.2 W/cm^2 at 550 °C. As shown in **Figure 75** (d). The vanadium ALD coated increases both ohmic and non-ohmic portion of the cell impedance, suggesting that vanadium modified surface blocks the surface reactions and is not active.

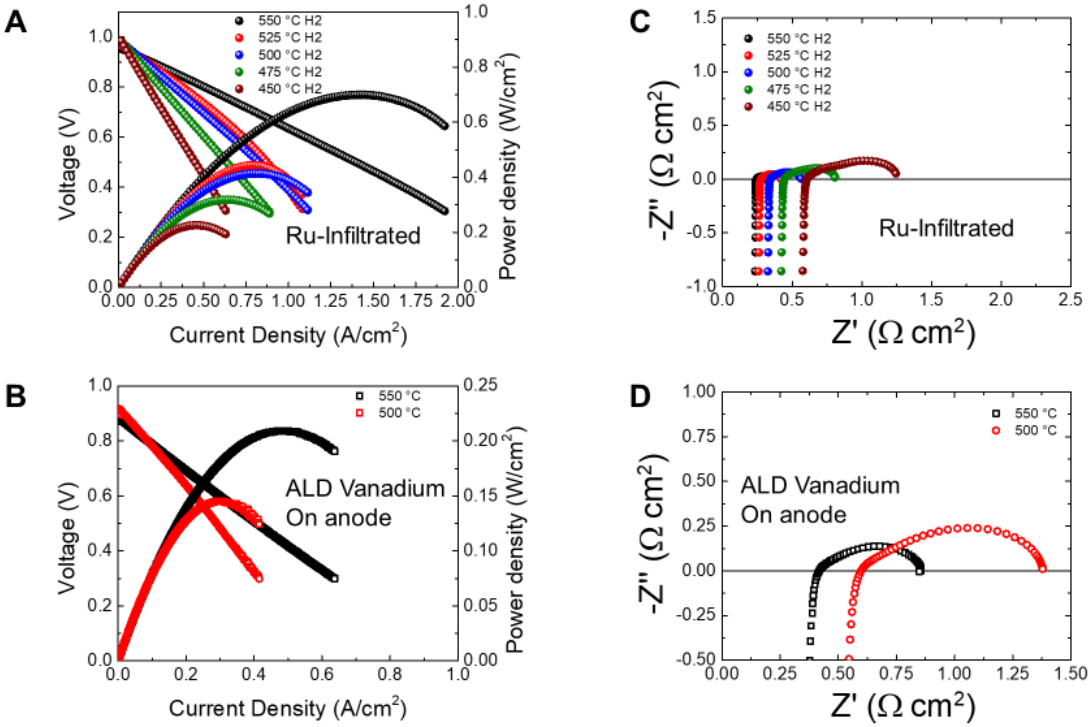

Figure 75. Surface modified anodes. (a) iV of Ru-infiltrated SFCM-GDC anode. (b) Vanadium oxide ALD on SFCM-GDC anode. (c) Nyquist plot of Ru-infiltrated SFCM anode. (d) Nyquist of vanadium oxide ALD on SFCM anode.

SFCM performance and durability in methane

We also determined the performance and stability of the ceramic anode in a hydrocarbon fuel environment. To do so a 60 vol% methane and 40 vol% H_2 gas stream was used to operate the cell for over 500 hours. The cell consists of an $SrFe_{0.2}Co_{0.4}Mo_{0.4}$-GDC (SFNM-GDC) anode with co-infiltrated Ni, Ru, and GDC, a 20 µm GDC electrolyte, a 10 µm thick Pr-GDC CFL (0.5 wt% Pr_6O_{11} in GDC), and a SSC-GDC cathode infiltrated with PrO_x in accordance with previous results. The nickel coupled with the ruthenium nano-particles will enhance stability operating under a hydrocarbon environment.

Figure 76 displays the results in H_2 and CH_4 as well as the stability operating on 60% CH_4 and 40% H_2 at 550 °C. A peak power density (PPD) of 0.7 W/cm^2 in H_2 and 0.5 W/cm^2 in CH_4 with an OCV of 0.95V at 550 °C are achieved, as shown in **Figure 76** B and D respectively for H_2 and CH_4.

The aging result is shown in **Figure 76** E and F, respectively, showing the galvanostatic and EIS. During aging in the hydrocarbon gas mixture the electrode ASR increases, likely due to coarsening of the nanoscale infiltrates. However, the cell maintained a voltage above 0.7V for the duration of the 500 hours, indicating high stability for the ceramic anode supported cell.

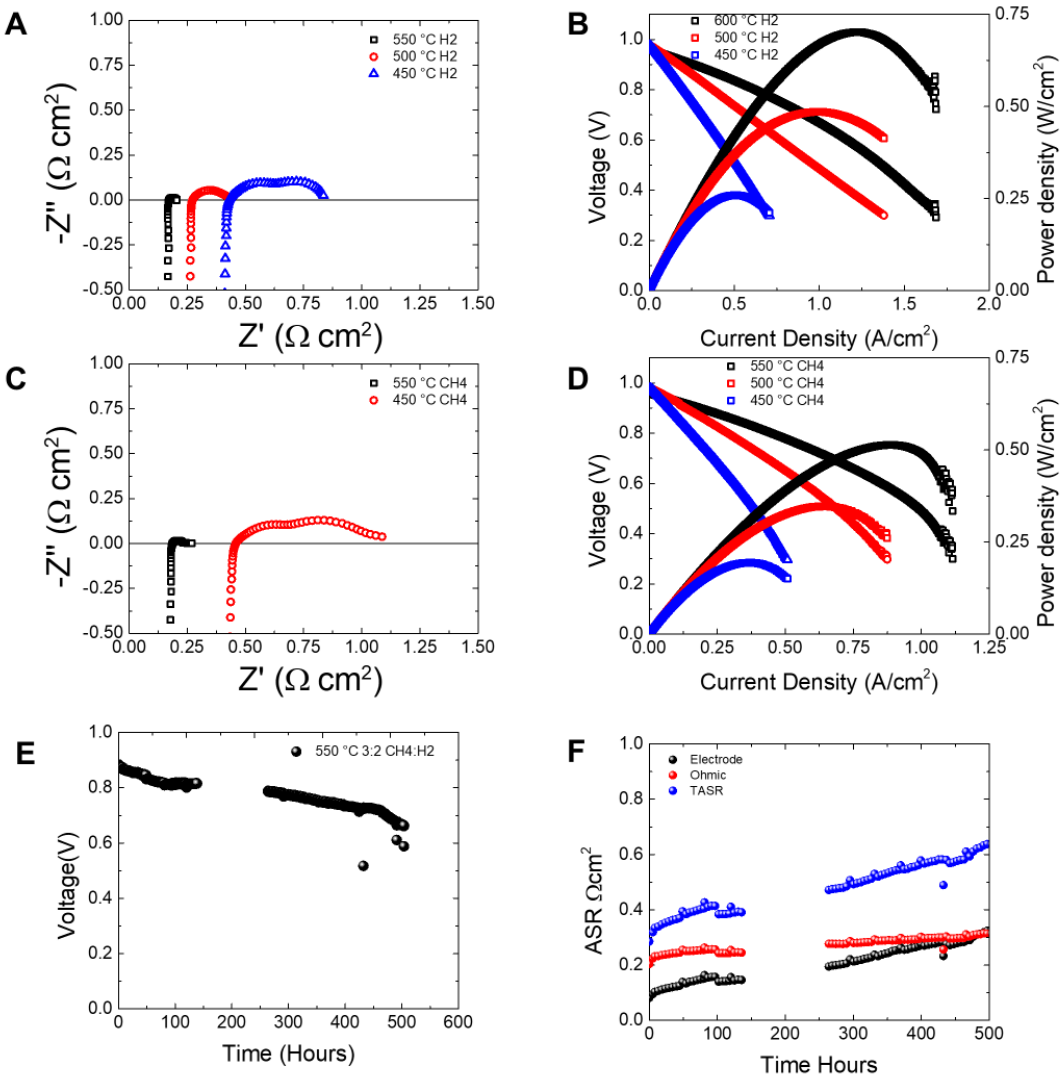

Figure 76. SFCM-GDC (Ru-Ni-GDC infiltrated anode)/GDC/Pr-GDC/SSC-GDC infiltrated with Pr (A) EIS and (B) iV in H_2. (C) EIS and (D) iV in CH_4. (E) Galvanostatic 0.2 A/cm^2 at 550 °C in a 3:2 CH_4 to H_2 gas mixture, and (F) the corresponding change of cell impedance during aging.

SFCM Ni-GDC Loading Optimization

We also optimized of the Ni-GDC on SFCM-GDC loading. It was found that a starting reference point for our SFCM-GDC cell system was ~ 1 mMol/cm^3 of Ni(10)-GDC(90 mol %) for the beginning stages of the SFCM development. In this process optimization appears to be no additional effect of infiltrating more than 1.5 mMol/cm^3 of Ni-GDC into the SFCM-GDC scaffold. **Figure 77** (a) and (b) show the infiltration loading effect of Ni-GDC on SFCM-GDC in iV and Nyquist plots, which shows significant performance enhancement.

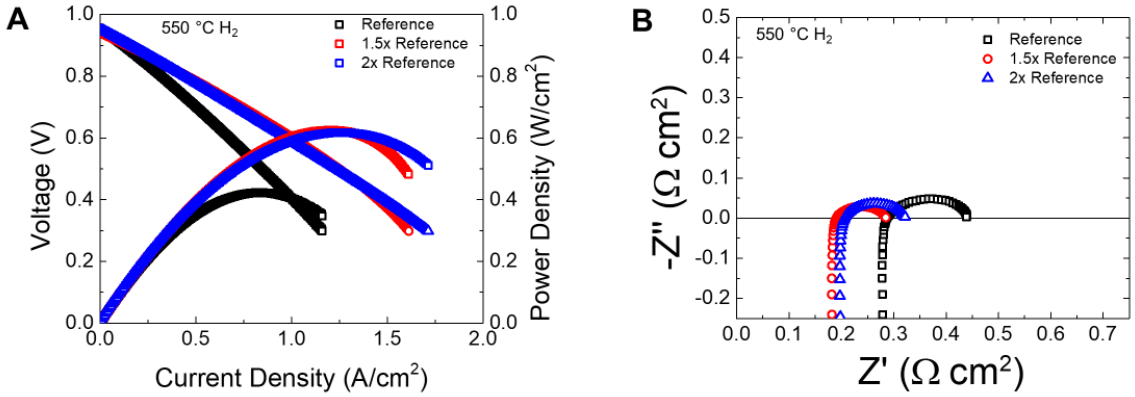

Figure 77. SFCM-GDC Scaffold infiltration optimization. (a) iV at 550 °C curves relating the reference amount (~ 1 mMol/cm^3) of Ni-GDC infiltrate to the increase in infiltration loading factor. (b) The corresponding Nyquist plots show the lowest ohmic and non ohmic ASR at 550 °C.

Methane-fueled infiltrated-SOFC

Different elements were infiltrated into SFCM anode supported cells to determine the activity in methane. The anode support cell fabrication procedure was shown in the previous report, and the iV curves of the infiltrated cells are shown in **Figure 78**. We did materials screening over multiple elements. Different anode infiltrates, including Zn, Ru, and Mg were added into the optimized Ni-GDC infiltrated cells. For Zn/Ni/GDC co-infiltrated cell, the peak power density reaches almost 0.3 W/cm^2 at 550°C in pure methane (3% H_2O). Mg/Ni/GDC co-infiltrated cell

shows the lowest performance (~0.22 W/cm^2). In contrast, with Ru/Ni/GDC co-infiltration, the peak power density reaches 0.45 W/cm^2.

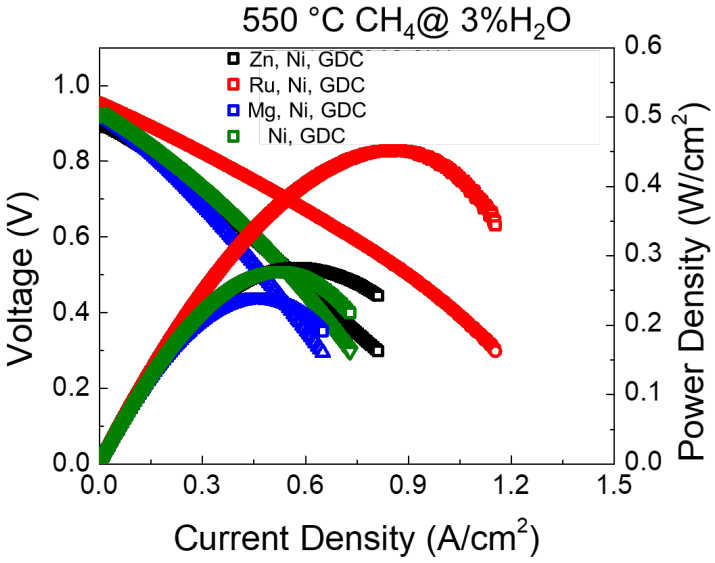

Figure 78. iV curves of SFCM based SOFCs with different infiltrates (Zn, Ru, Mg, and Ni) in CH_4.

The corresponding EIS spectra are shown in **Figure 79**. In methane, the co-presence of Ni/GDC/Ru effectively reduces the cell area specific resistance (red), compared to other infiltrates.

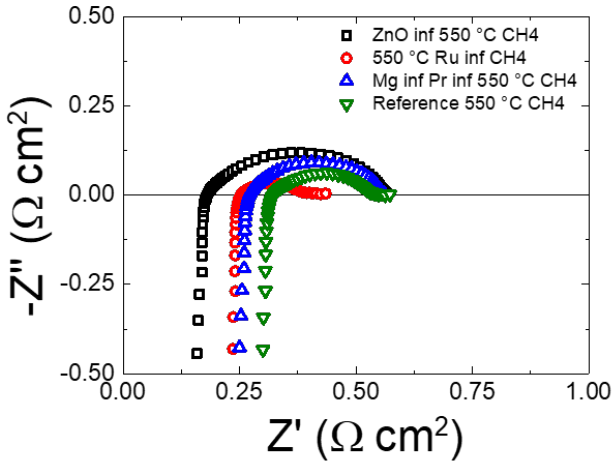

Figure 79. EIS spectra of SFCM based SOFCs with different infiltrates in CH_4.

The performance of Ni/Ru/GDC modified SFCM cell in H_2 and CH_4 is shown in **Figure 80.** The modified cell shows good performance at low-intermediate temperatures. At 550°C, the cell shows a peak power density of 0.7 and 0.45 W/cm^2 in H_2 and CH_4, respectively. At lower temperatures, the cell still shows decent performance in pure methane (>0.1 W/cm^2 at 550°C). Thus, we demonstrated that Ru/Ni/GDC co-infiltrated cell is the optimized composition for SFCM modification.

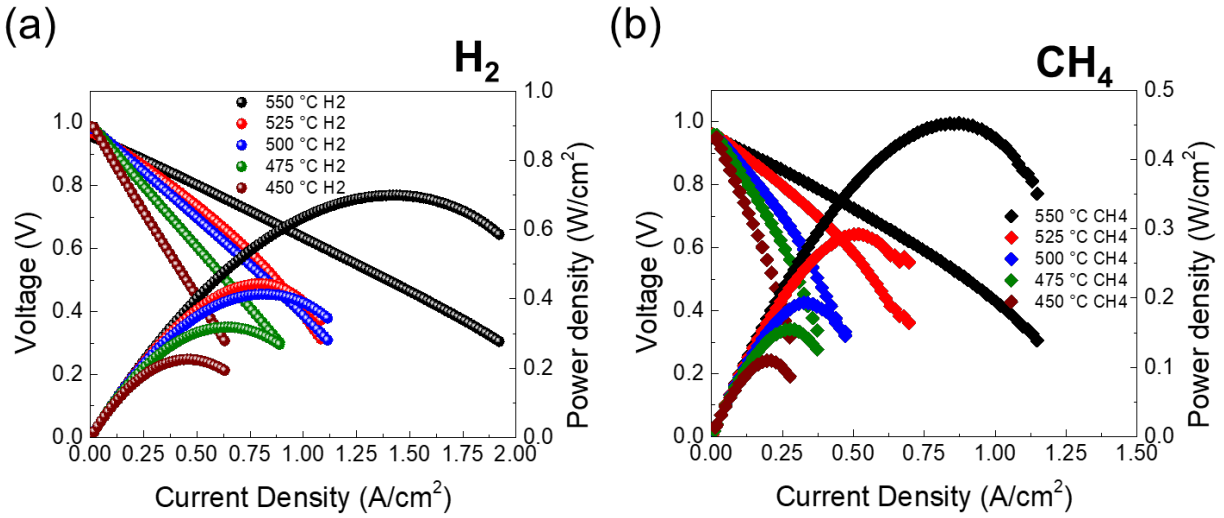

Figure 80. Ni-Ru GDC co infiltrated SFCM anode supported SOFCs in (a) H_2 and (b) CH_4 at different temperatures.

We also tested a SOFC with the combination of ALD and solution modification, as shown in **Figure 81**. The tested cell consists of SFCM-GDC anode with ZnO ALD layer and Ni/GDC infiltration, GDC electrolyte, cathode functional layer (CFL), SSC cathode with Pr infiltration. The PPD of the cell is about 0.7 W/cm^2 and 0.3 W/cm^2 at 550 and 500°C, respectively, (**Figure 81(a)**), and the corresponding impedance is shown in (**Figure 81(b)**). The aging profile is shown in **Figure 81(b)**. The cell was aged for over 350 hours and the cell voltage drops as a function of time.

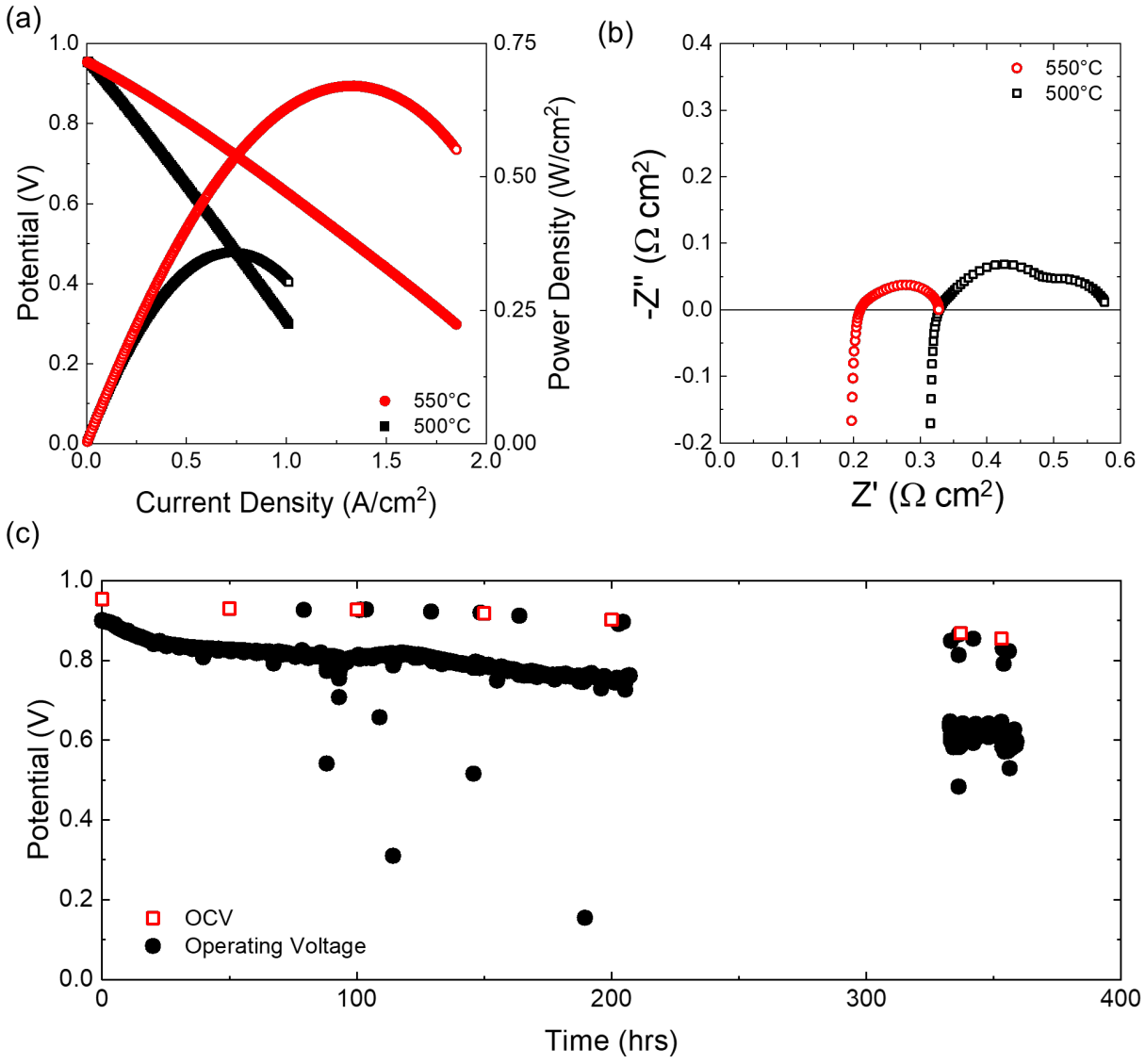

Figure 81. SOFC performance of the cathode and anode modified SOFC. (a) iV curve and (b) EIS spectra, and (c) the aging results at 550°C in H_2 at 0.2 A/cm². The cell configuration: SFCM anode with ZnO(ALD), Ni and GDC (infiltration), and SSC cathode with Pr infiltration.

Characterization of Modified Electrodes

Figure 82 shows the microstructure of the aged cell that is previously shown (**Figure 81**). The SOFC has a 20 µm dense GDC electrolyte (**Figure 82 (a)**). Both SSC and SFCM anode show high porosity after 350 hours of aging in **Figure 82 (b,d)**. Both surface modification in cathode and anode can be clearly seen in **Figure 82 (c,f)**. The corresponding EDS elemental mapping is shown in **Figure 83**, where the signals of Zn, Ni, Gd, and Ce are shown. Ni and Zn are well distributed on the anode surface.

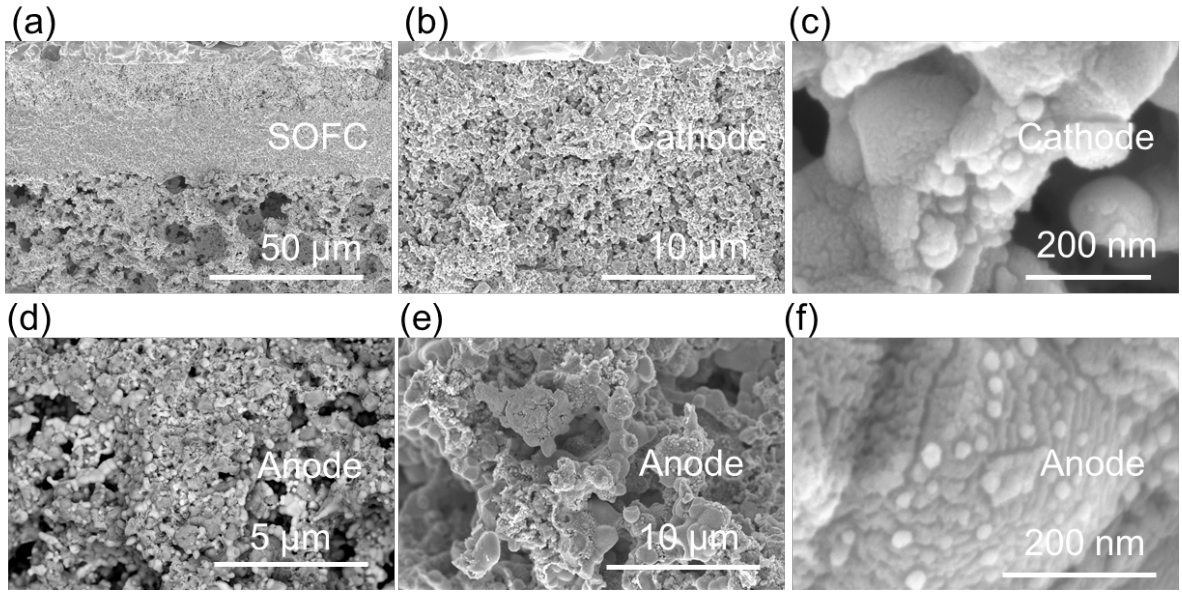

Figure 82. Microstructure of the Aged SFCM-based SOFC where ZnO(ALD) and Ni/GDC (infiltration) were introduced to SFNM anode and Pr was infiltrated in SSC cathode. The cell was aged at 550 for 250 hours.

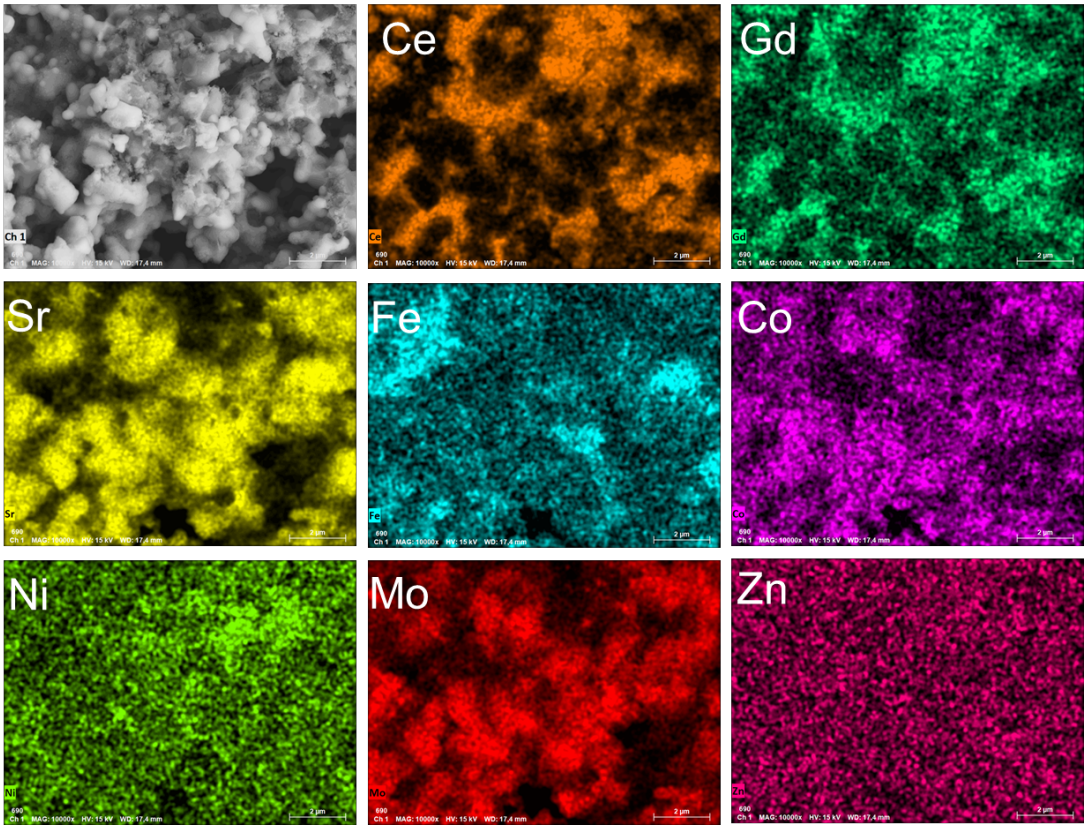

Figure 83. EDS elemental mapping on the aged SFCM-based SOFC where ZnO(ALD) and Ni/GDC (infiltration) were introduced to SFNM anode and Pr was infiltrated in SSC cathode. The cell was aged at 550 for 250 hours.

Figure 84 shows structure analysis on the modified cathode. XRD on PrO_x that sintered at different temperature in **Figure 84** (a) shows a similar diffraction pattern but a slight shift in the peak position. It suggests that PrO_x phase is formed and the sintering temperature affects the level of oxygen stoichiometry (x), and the oxygen content of PrO_x seems to play an important role in its catalytic activity. **Figure 84** (b) shows PrO_x on SSC after sintering, and no observable secondary phase is formed, suggesting that the modified cathode is stable.

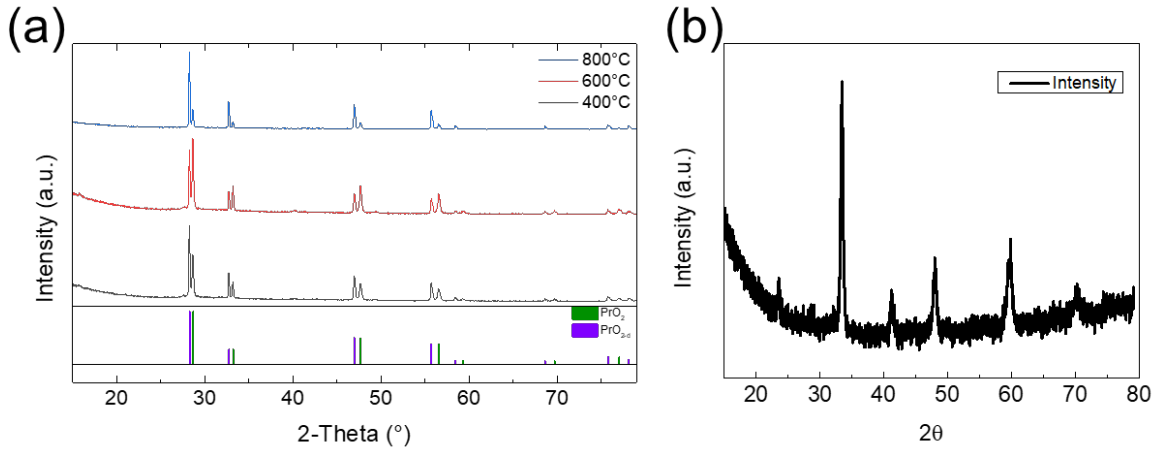

Figure 84. XRD on (a) PrO_x after sintering at different temperatures and (b) PrO_x infiltrated SSC.

Figure 85 shows Pr and O signals of XPS analysis on PrO_x that sintered at different temperatures. **Figure 86** shows XPS analysis on Pr infiltrated SSC cathode. Ce 3d (**Figure 86**(a)), Pr 3d (**Figure 86**(b)), and Co 2p (**Figure 86**(c)) spectra. Pr 3d and 4d spectra suggest that Pr is in a mixed state of 3+ and 4+ both sintering temperatures.

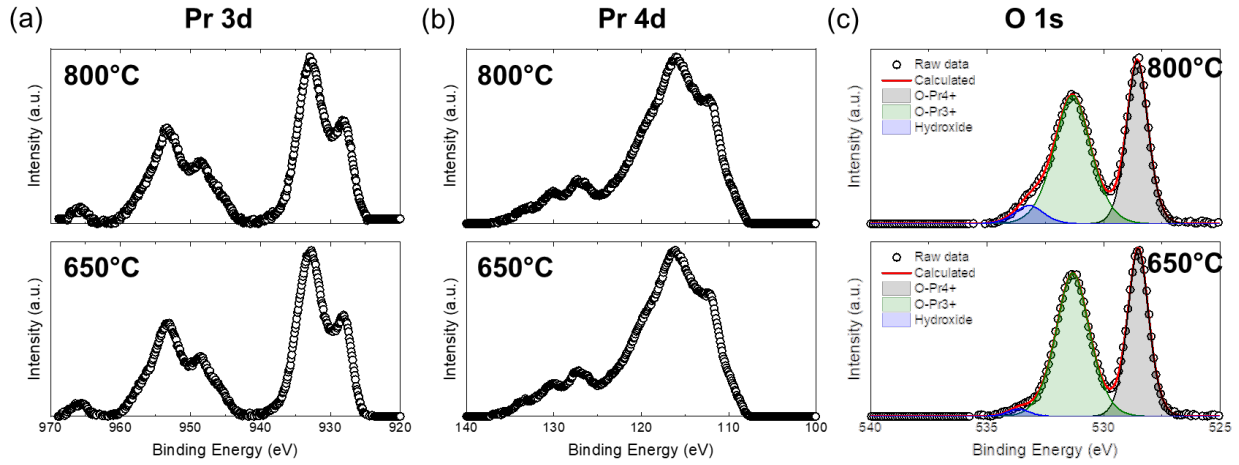

Figure 85. XPS on PrOx sintered at different temperatures: (a) Pr 3d, (b) Pr 4d, and (c) O 1s.

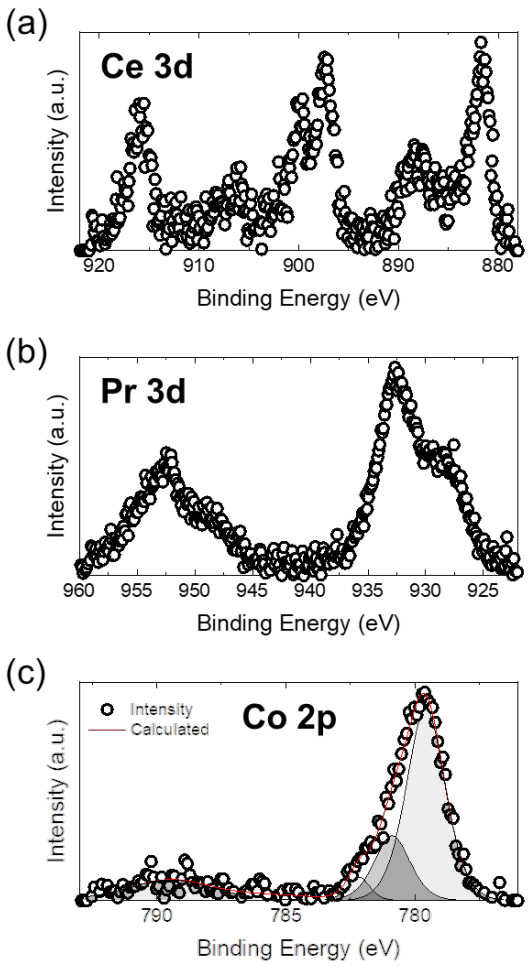

Figure 86. XPS analysis on Pr infiltrated SSC cathode: (a) Ce 3d, (b) Pr 3d, and (c) Co 2p.

TEM EDS analysis was performed on Ni/Ru/GDC infiltrated SFCM, as shown in **Figure 87**. **Figure 87** (a) shows TEM image on the infiltrated SFCM particle, and the corresponding EDS elemental mapping is shown in **Figure 87** (b). Ru and Ni are well dispersed on SFCM particle while Gd, and Ce seem to agglomerate to a larger particle. **Figure 87** (c) shows HR-TEM on the infiltrated particles, showing that all particles are crystalline and less than 5nm.

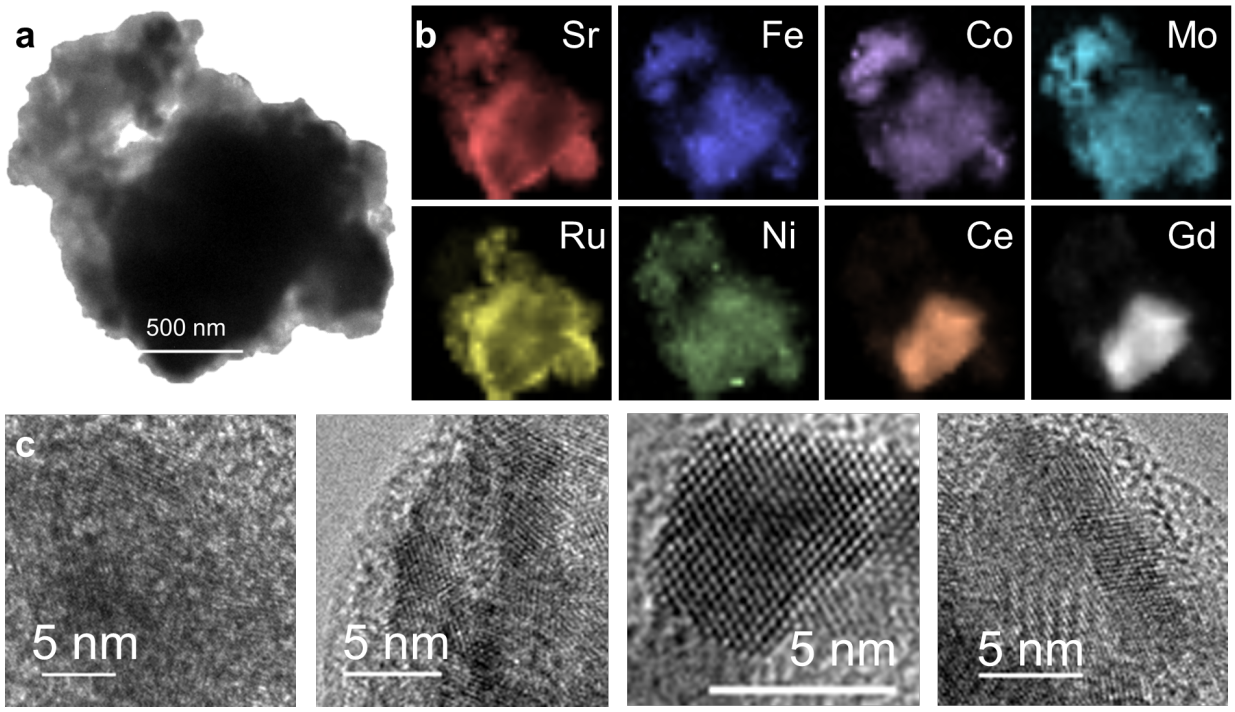

Figure 87. TEM characterization. (a) TEM on the modified SFCM particle. (b) Elemental mapping on the particle in (a). (c) High-resolution TEM (HR-TEM) on the modified SFCM particles.

Figure 88 shows the microstructure of SFNM aged in H_2 at different temperatures. In general, at both temperatures, the SFNM anode still shows intact after aging. **Figure 88** (a) and (b) show SEM micrographs of SFNM aged at 550°C for 170 hrs. The SFNM ceramic anode maintains its porous structure after 170 hours of testing, and the spike shape microstructure is observed on the SFNM surface in a higher magnification in **Figure 88** (b). **Figure 88** (c) and (d) show SEM micrographs of SFNM aged at 600°C for 300 hrs. SFNM still holds its porous microstructure after aging at 600°C and the exsolved FeNi particles can clearly be seen in **Figure 88** (d).

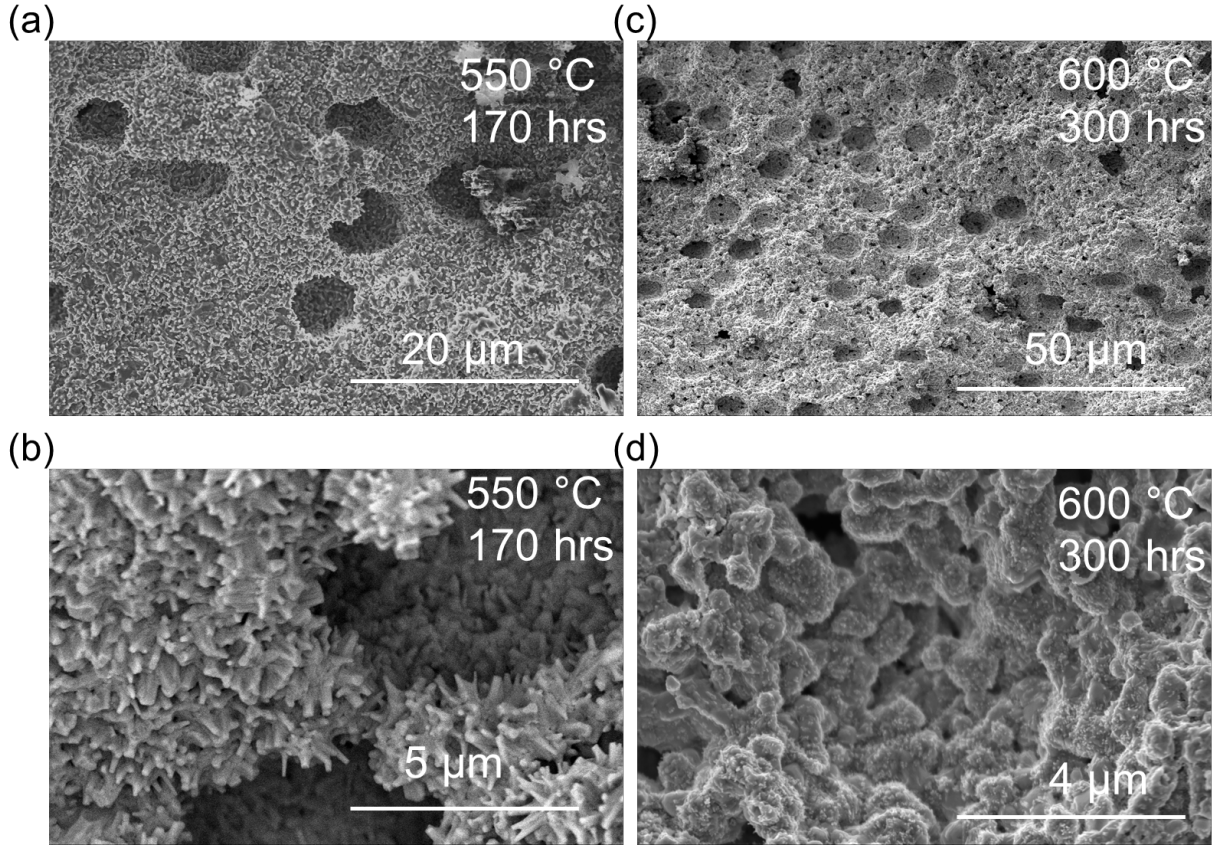

Figure 88. Microstructure of aged SFNM: (a) At 550 °C for 170 hours and (b) the enlarged view. (c) At 600 °C for 300 hours and (d) the enlarged view.

Products

1. I. A. Robinson, Y.L. Huang, S. Horlick, A. Mohammed Hussain, A. Pesaran, and E. D. Wachsman "Performance and Durability Enhancement for Low-Temperature Solid Oxide Fuel Cells via Surface Chemistry Modification" under revision (2020).
2. E. Ostrovskiy, Y.L. Huang, E. D. Wachsman, ""Effects of Surface Chemical Potentials on Cation Segregation," *Journal Materials Chemistry A,* DOI: 10.1039/d0ta08850a (2020).
3. I. A. Robinson, Y.L. Huang, S. Horlick, J.Obenland, N. Robinson, J. Gritton, A. Mohammed Hussain, and E. D. Wachsman "Mitigating Electronic Conduction in Ceria-based Electrolytes via External Structure Design" in preparation, (2020).
4. S.A Horlick, Y.L. Huang, I.A. Robinson, and E. D. Wachsman "Understanding and Controlling Exsolution kinetics on $SrFe(Ni,Mo)O_3$" in preparation, (2020).

5. I. A. Robinson, S. Horlick, Y.L. Huang, and E.D. Wachsman, "Scaffold Infiltrated Cathodes for Low-Temperature Solid Oxide Fuel Cells" in preparation, (2020).

Milestone Status Report

	Planned Completion Date	Actual Completion Date	Verification Method	Comments
MS 2.1 : Develop ALD coating techniques	12/31/2018	12/31/2018	Deposited ALD films/SEM/EIS/ECR	
MS 2.2: Develop solution-based infiltration techniques	3/31/2019	3/31/2019	Solution infiltration /SEM/EIS	
MS 3.1: Determine the performance of modified cathodes	6/30/2019	6/30/2019	SEM/EIS/ECR	
MS 3.2: Identify optimized surface modification process	9/30/2019	9/30/2019	IV/SEM/EIS/ECR	
MS.4.1: Determine the performance of modified anodes	12/31/2019	12/31/2019	IV/SEM/EIS	
MS.4.2: Determine the performance of modified anodes in methane	3/31/2020	3/31/2020	IV/SEM/EIS	Covid-19
MS.5.1: Integrate to full button cells.	6/30/2020	9/30/2020	IV/SEM/EIS	Covid-19
MS.5.2: Post-testing characterization of surface modified SOFCs	9/30/2020	12/31/2020	IV/SEM/EIS	Covid-19

References

1. Oh, D., Gostovic, D. & Wachsman, E. D. Mechanism of La0.6Sr0.4Co0.2Fe0.8O3 cathode degradation Dongjo. *Journal of Materials Research* **27**, 1992–1999 (2012).

2. Mathew Niania, Renaud Podor, T. Ben Britton, Cheng Li, S. J. C. & Nikolai Svetkov, S. S. and J. K. In situ study of strontium segregation in La0.6Sr0.4Co0.2Fe0.8O3-d in ambient atmospheres using high-temperature environmental scanning electron microscopy. *Journal of Materials Chemistry* **6**, 14120–14135 (2018).
3. Piskin, F., Bliem, R. & Yildiz, B. Effect of crystal orientation on the segregation of aliovalent dopants at the surface of La.Sr.CoO. *Journal of Materials Chemistry A* **6**, 14136–14145 (2018).
4. Kim, H. K., Jang, D. Y., Kim, J. W., Bae, K. & Shim, J. H. Ionic properties of ultrathin yttria-stabilized zirconia thin films fabricated by atomic layer deposition with water, oxygen, and ozone. *Thin Solid Films* **589**, 441–445 (2015).
5. von Gastrow, G. *et al.* Ozone-based Batch Atomic Layer Deposited Al2O3 for Effective Surface Passivation. *Energy Procedia* **38**, 890–894 (2013).
6. Choi, M.-B. *et al.* Interpretation of Impedance Spectra of Solid Oxide Fuel Cells: L-Curve Criterion for Determination of Regularization Parameter in Distribution Function of Relaxation Times Technique. *JOM* **71**, 3825–3834 (2019).
7. Boukamp, B. A. & Rolle, A. Use of a distribution function of relaxation times (DFRT) in impedance analysis of SOFC electrodes. *Solid State Ionics* **314**, 103–111 (2018).